Karlsruher Institut für Technologie

IEKP-KA/2016-21

Model-Unabhängige Ausschlussgrenzen auf exotische Diboson Resonanzen mit dem CMS Detector bei einer Schwerpunktsenergie von $\sqrt{s} = 13$ TeV

Masterarbeit
von
Daniela Schäfer

An der Fakultät für Physik
Institut für Experimentelle Kernphysik

Referent:	Prof. Dr. Th. Müller
Korreferent:	Prof. Dr. U. Husemann

04. Nov 2016

Zusammenfassung

Seit seiner Entwicklung in den sechziger Jahren des neunzehnten Jahrhunderts ist das Standardmodell der Teilchenphysik zu einer der erfolgreichsten und genauesten vermessenen physikalischen Theorien geworden. Mit der Entdeckung eines Higgs-Bosons im Jahr 2012, dessen Eigenschaften mit denen des im Standardmodell vorhergesagten Higgs-Bosons übereinzustimmen scheinen, hat das Standardmodell noch einmal eine Bestätigung erfahren. Trotz seines überwältigenden Erfolgs bleiben einige Fragen und Probleme offen. Ein Beispiel hierfür ist der Versuch, Gravitation als vierte Kraft in das Standardmodell zu integrieren. Es gibt viele verschiedene Theorien, wie zum Beispiel Modelle, die endliche gekrümmte Extradimensionen enthalten, die am LHC als Resonanzen im invarianten Massenspektrum von zwei elektroschwachen Bosonen beobachtet werden könnten.

Mit dem neuen Datensatz der 2015 am LHC bei einer Schwerpunktsenergie von 13 TeV aufgenommen wurde, wird in vielen verschiedenen Endzuständen nach neuer Physik im Diboson-Massenspektrum gesucht. Um dabei eine hohe Rekonstruktionseffizienz auch in geboosteten Endzuständen zu erreichen, wie sie von einem Zerfall eines schweren Teilchens zu erwarten sind, werden zur Rekonstruktion von hadronisch zerfallenden Vektor-Bosonen Techniken eingesetzt, die auf der Analyse der Substruktur von Jets beruhen.

Analysen, die nach neuer Physik suchen, sehen sich immer mit dem Problem konfrontiert, dass es eine Vielzahl an Modellen gibt, die unterschiedliche Phänomenologien am LHC vorhersagen. Idealerweise müssten Ausschlussgrenzen für jedes dieser Modelle gefunden werden; dies ist in der Praxis jedoch nicht möglich. Stattdessen konzentrieren sich die meisten Suchen auf einige wenige Modelle, innerhalb derer ihre Ergebnisse zu interpretieren sind. Durch diese Auswahl bleiben einige Modelle unbeachtet. Diese Arbeit schließt durch die Erweiterung zweier Diboson Resonanzsuchen, mit unterschiedlichen Endzuständen, auf eine modellunabhängige Interpretation, diese Kluft zwischen Theorie und Experiment. Zu diesem Zweck werden modellunabhängige Ausschlussgrenzen als Funktion der Resonanzmasse und der relativen Breite der Resonanz berechnet. Die Ausschlussgrenzen berücksichtigen Unterschiede der Rekonstruktions- und Identifikationseffizienzen zwischen verschiedenen Modellen, indem eine zusätzliche, von der Resonanzmasse abängige Unsicherheit der erwarteten Anzahl der Signalereignisse eingeführt wird. Die modellunabhängigen Ausschlussgrenzen sind in Abbildung 0.1 zu sehen. Die beobachteten Ausschlussgrenzen stimmen innerhalb einer Standardabweichung mit den

erwarteten Ausschlussgrenzen überein. Die betrachteten Endzustände sind ein semileptonischer Endzustand und ein hadronischer Endzustand. Im semileptonischen Endzustand zerfällt ein W-Boson leptonisch und das zweite Boson, das ein W- oder Z-Boson sein kann zerfällt hadronisch. Im hadronischen Endzustand zerfallen beide produzierte Vektorbosonen hadronisch, als Zwischenzustände sind zwei W-, zwei Z- oder ein W-Boson und ein Z-Boson berücksichtigt.

Um die Berechnung der modellunabängigen Ausschlussgrenzen als Funktion der natürlichen Breite der Resonanz möglich zu machen, wird im Rahmen dieser Arbeit ein Modell für die funktionale Parametrisierung breiter Resonanzformen entwickelt und an Simulationen verschiedener Modelle getestet.

Um einen Vergleich der Vorhersagen arbiträrer Modelle mit den gegebenen modellunabängigen Ausschlussgrenzen zu ermöglichen, werden die Rekonstruktionseffizienzen von hadronisch zerfallenden W- oder Z-Bosonen und von leptonisch zerfallenden W-Bosonen innerhalb der Analysen berechnet und mittels dem transversalen Impuls und der Pseudorapidität des generierten Vektorbosons parametrisiert. Mithilfe dieser Effizienzparametrisierung und eines im Rahmen dieser Arbeit geschriebenen Programms kann, ausgehend von Simulationen im Les Houches Format, die Signalereignishäufigkeit für beliebige Modelle berechnet werden.

Um das dieser Arbeit zu Grunde liegende Konzept zu testen, werden Ausschlussgrenzen für ein Randall-Sundrum-Modell [1] berechnet. Mit dem modellunabhängigen System können in diesem Modell Resonanzmassen kleiner als ungefähr 2 TeV und natürliche Resonanzbreiten Γ/M_X zwischen 0.05 und 0.3 ausgeschlossen werden. Diese Grenzen sind nur um ungefähr einen Faktor 2 schlechter als spezifisch für dieses Modell berechnete Grenzen im sensitiveren Diphoton-Zerfallskanal, siehe [2, 3].

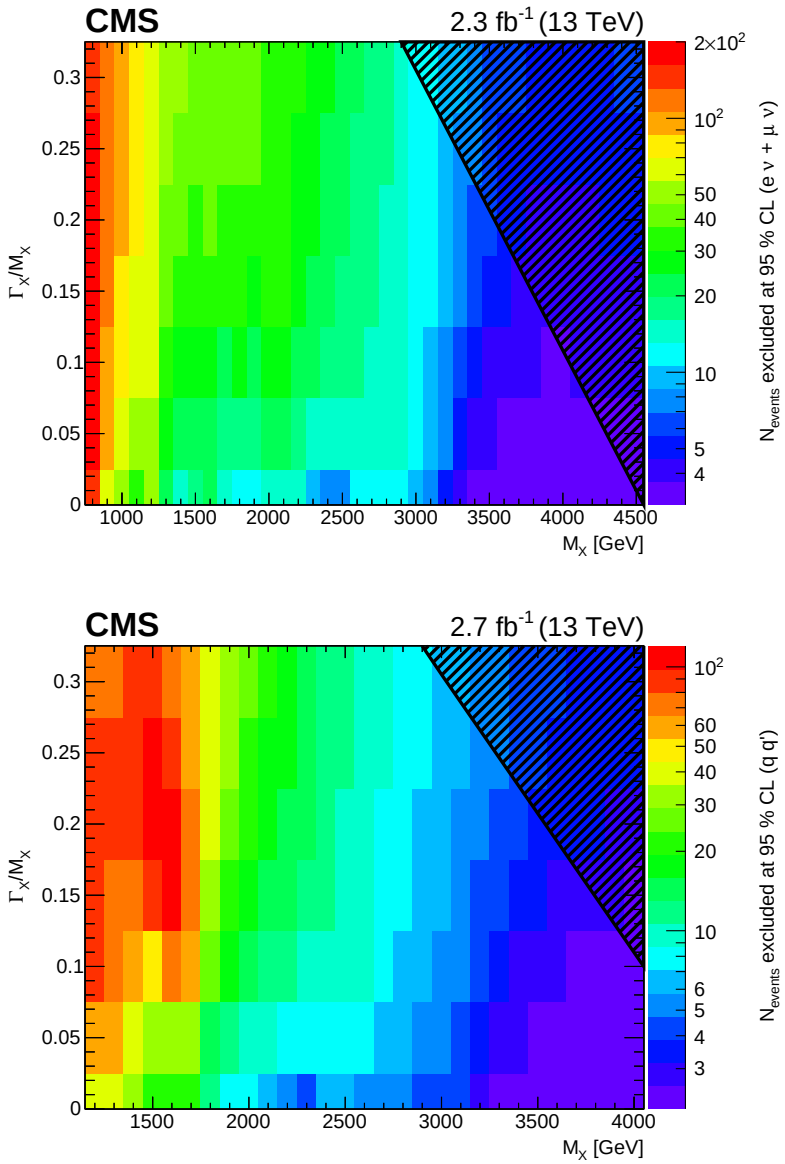

Figure 0.1.: Die modellunabhängigen Ausschlussgrenzen für ein Konfidenzniveau von 95% als Funktion von der Resonanzmasse M_X und der relativen Breite Γ/M_X. Die Ausschlussgrenzen sind auf die Ereignisanzahl für vorhersagen von arbiträren Modellen gegeben. Oben sind die beobachteten Ausschlussgrenzen für den semileptonischen Endzustand, unten diejenigen für den hadronischen Endzustand. Der schattierte Bereich markiert den Parameterbereich, in dem die Form von mit Gluon-Fusion produzierten Resonanzen mit dem verwendeten Modell für die Resonanzform nicht mehr beschrieben werden kann. In diesem Bereich sind die Ausschlussgrenzen nur noch für Modelle gültig, die primär andere Produktionsmechanismen verwenden.

Karlsruhe Institute of Technology

IEKP-KA/2016-21

Model-Independent Limits on Diboson Resonances with the CMS Detector at $\sqrt{s} = 13$ TeV

Mastersthesis
of
Daniela Schäfer

At the Department of Physics
Institut für Experimentelle Kernphysik

Advisor:	Prof. Dr. Th. Müller
Second advisor:	Prof. Dr. U. Husemann

Nov 4, 2016

I declare that I have developed and written the enclosed thesis completely by myself, and have not used sources or means without declaration in the text.

Karlsruhe, 04.11.2016

. . . . . .

(Daniela Schäfer)

Introduction

Since its development in the 1960s the Standard Model (SM) of particle physics has become the most successful and precise physical theory of all time. For all its merits, however, the standard model is not without flaws in both phenomenology and theory. Prominent examples include the Hierarchy problem, that introduces fine tuning of theory parameters, Neutrino flavor mixing, that has been experimentally observed but is not described by the SM, and the absence of the fourth fundamental force of nature, gravity, in the SM.

As a consequence, even though SM predictions describe the data taken by generations of particle accelerators very well, the general consensus within the particle physics community is that a multitude of new physical phenomena not described by the SM are to be expected at high energy scales. This skepticism regarding the SM lead to the development of new ideas such as grand unification, which tries to unify three of the four fundamental forces of nature (electromagnetic, weak and strong force) within one gauge group that is then dynamically broken at some higher energy scale, or Supersymmetry, which can solve the hierarchy problem. Another interesting idea is the attempt to include the effects of the fourth fundamental force, gravity, by introducing a corresponding particle, the graviton, into the SM. Well known representatives of this are warped extra dimensional models.

Since the spectacular discovery of the Higgs boson in 2012 at the Large Hadron Collider (LHC), a new run at a center of mass energy of $\sqrt{s} = 13$ TeV has begun in 2015, collecting data at energies never before reached in a laboratory.

This opens new opportunities for searches of physics beyond the Standard Model (BSM). Many BSM theories predict new resonances, for example in the diboson channel, at energies of a few TeV. However, due to the multitude of models with different phenomenologies only a fraction of existing models can be considered by a dedicated analysis by one of the experimental groups at the LHC. This leaves many theorists and model-builders who are unable to determine wether or not some of their predictions are already excluded by experimental results.

This thesis aims to provide such model-builders with the means to find experimental limits for the parameters of their respective models without having to rely on the help of experimental groups. As a first step towards this goal model-independent limits on

diboson resonances with a semileptonic or hadronic final state are extracted from data collected by the CMS detector at the LHC. Based on these limits a ready-to-use framework is then developed, which enables theorists to calculate the approximate signal yield of their theory predictions. As a proof-of-concept of the provided framework its application to a example model in the Randall-Sundrum scenario is demonstrated.

This thesis is organized as follows. Chapter 1 gives a short overview over the Standard Model of particle physics as well as beyond the Standard Model theories predicting diboson resonances. In chapter 2 the construction and operation of the Large Hadron Collider and the Compact Muon Solenoid Detector are explained. Chapter 3 is dedicated to the reconstruction of events in the detector as well as the physical principles behind Monte Carlo event generators. A description of the statistical methods used in this thesis is found in chapter 4. Chapter 5 contains a detailed description of two CMS analyses searching for diboson resonances in the semileptonic and hadronic final state. Finally, chapter 6 describes the calculation procedure for model-independent limits for both channels as well as a working example of the framework provided for an RS1-Graviton theory model.

Contents

1. Theoretical Introduction

The standard model (SM) of particle physics is a theoretical model describing the interactions and free behaviour of fundamental particles with great precision. Developed in the 1960th it is now one of the most powerful theories in physics, with its last missing piece, the Higgs boson, discovered in 2012. However although the standard model provides astoundingly precise predictions for the three fundamental forces of electromagnetism, the strong and the weak force, it still leaves unanswered questions and problems that hint at the SM only being an effective theory valid at relatively low energy scales, compared to the Planck scale at 10^{19} GeV. Since this thesis is an experimental work using the concepts of basic quantum field theory and the SM, the first section (1.1) will give a brief introduction to the SM of particle physics as well as a few glimpses at questions that the SM is not able to answer. The second part of this theoretical introduction (section 1.2) will be dedicated to models beyond the standard model (BSM) that try to address some or all of the problems of the SM. In this chapter natural units as well as the Einstein notation are used throughout. The following section is based on references [4–7].

1.1. The Standard Model of Particle Physics

One of the most basic concepts of the standard model is the connection between symmetries and the conservation laws following from them. The formalism connected to this is described mathematically by Noether's theorem [8, 9] and allows for general constraints on the formulation of a theory based on the observation that certain quantities are conserved. A convenient way of writing down such a theory with these restrictions in mind is using the Lagrange formalism; in the case of field theories Lagrange densities are used. As is the case in classical mechanics, as far as we know today every physical theory should hold under the following assumptions:

- The result of an experiment should be the same if it is shifted in time or space (invariance under translations).

- The result of an experiment should also remain unchanged if the whole experiment is rotated in space (rotational invariance).

Since a relativistic formulation is needed to describe phenomena involving elementary particles, the theory should also be invariant under Lorentz boosts. In summary the theory is supposed to be invariant under the full Poincaré group giving rise to the conservation of energy, momentum and angular momentum. These symmetries are global coordinate transformations.

However, the Poincaré group is not the only ingredient needed to formulate the SM; in addition the theory builds on knowledge from non-relativistic quantum mechanics, additional local symmetries that will be discussed later and other principles such as causality.

One of the trademarks of a quantum field theory is that the particle fields themselves are described by operators connected to the particle interpretation via expectation values - however the fields themselves are often called "particles" anyway.

The SM contains three different kinds of particles. The first kind are gauge bosons which are introduced mathematically using invariance under local gauge transformations and are therefor associated with a gauge symmetry; these will be described in more detail in the next section. The second kind are matter particles, which have a spin of $1/2$ and are governed by the Dirac equation (1.1) in their free state; they differ only in their charges under the gauge groups of the SM, which will be described in the next section, or in their mass m. The Dirac equation is

$$i\partial\!\!\!/\Psi - m\Psi = 0 \ , \tag{1.1}$$

with the particle field Ψ and $\partial\!\!\!/ = \gamma_\mu \partial^\mu$. The third kind of particle found in the SM is massive spin-0 field, called the Higgs boson. A spin-0 particle such as the SM Higgs boson in its free state is governed by the Klein-Gordon Equation

$$\partial_\mu \partial^\mu \Phi + m^2 \Phi = 0 \ . \tag{1.2}$$

The free fields in quantum field theory are the quantised solutions of (1.1) or (1.2)

$$\Phi(x) = \int \frac{d^3k}{(2\pi)^3} \left(e^{ikx} \frac{a^\dagger(\vec{k})}{2k^0} + e^{-ikx} \frac{a(\vec{k})}{2k^0} \right) \ , \tag{1.3}$$

$$\Psi(x) = \int \frac{d^3k}{(2\pi)^3} \sum_s \left(e^{ikx} v_s(\vec{k}) b_s^\dagger(\vec{k}) + e^{-ikx} u_s(\vec{k}) a_s(\vec{k}) \right) \ , \tag{1.4}$$

where $a, a^\dagger$ are annihilation/ creation operators of a spin 0 particle with momentum k, $a_s/b_s^\dagger$ are annihilation/creation operators of a spin s particle/anti-particle with momentum k, and u_s/v_s are spinors. A particle corresponds to the creation operator $a_s^\dagger(\vec{k})$ applied to the vacuum, it has a positive energy eigenvalue, while and anti-particle corresponds to the construction operator $b_s^\dagger(\vec{k})$ and has a negative energy eigenvalue.

1.1.1. Gauge Symmetries

The SM is constructed of several symmetries that are required to hold locally, i.e. under local spatial-dependent transformations of the symmetry group. The requirement that these symmetries hold requires the presence of gauge fields and determines the interaction of SM particles mediated by the gauge fields in a unique way. Each introduction of a new symmetry group leads to new charges for the matter fields, which relate the matter field to the gauge group generators. The matter fields belong to the fundamental representation of the gauge group, i.e. they transform as $\Psi \to U\Psi$ where $U = U(x)$ is a unitary matrix parametrising a gauge transformation. The gauge fields themselves belong to the adjoint representation of the gauge group, i.e. they transform as $\phi \to U\phi U^\dagger$.

The SM consists of three gauge groups, the associated mediator fields and kinematic terms for the fermions of the theory, and the kinematic and potential terms of a scalar spin-0 particle, the Higgs boson. In addition to this an interaction term between the Higgs boson and the fermion fields is added. The Higgs field is introduced to give rise to the masses of the weak gauge bosons, as well as the fermions, through spontaneous symmetry breaking.

The full symmetry group of the SM is $\mathrm{SU}(3)_C \times \mathrm{SU}(2)_L \times \mathrm{U}(1)_Y$. $U(n)$ is the group of all unitary $n \times n$ matrices, while $\mathrm{SU}(n)$ is a subgroup of this, containing only matrices with a determinant of 1. All three symmetry groups are also Lie groups and can therefore be described by a Lie algebra of the form

$$[T^a, T^b] = f^{abc}T^c \ , \tag{1.5}$$

where T^a are the group generators and f^{abc} is the structure constant. Each local gauge symmetry leads to n new gauge boson fields, where n is the number of Lie group generators.

Quantum Chromodynamics

The non-abelian Lie-group $\mathrm{SU}(3)_C$ is the gauge symmetry of the strong force with colour as charge. The Lagrange density $\mathcal{L}$ can be written as

$$\mathcal{L}_{QCD} = -\frac{1}{4}\left(G^a_{\mu\nu}G^{a,\mu\nu}\right) + \sum_{\text{quark flavours}} \bar{q}_i \not{D}_{ij} q_j \ , \tag{1.6}$$

$$D_{\mu,ij} = \partial_\mu \delta_{ij} - igG^a_\mu T^a_{ij} \ , \tag{1.7}$$

$$G^a_{\mu\nu} = \partial_\mu G^a_\nu - \partial_\nu G^a_\mu + g f^{abc} G^b_\mu G^c_\nu \ , \tag{1.8}$$

Here G are the gauge fields i.e. gluons, q are the quark spinor fields, g is the coupling and D_μ is the covariant derivative. The indices a, b, and c sum over the eight generators

of the Lie group, and the indices i and j denote the quark colours. A non-abelian gauge group like SU(3) gives rise to self couplings of the gauge fields which leads to triple and quadruple vertices in the Feynman rules for QCD. The gauge bosons of the strong force, generally referred to as gluons, remain massless after the spontaneous symmetry breaking of the Higgs field. However, because of the special non-abelian structure of QCD, the strong coupling constant α_s, which is proportional to g^2 in first order perturbation theory, grows smaller at high energies and larger at small energies, leading to the two phenomena of asymptotic freedom and confinement. Consequently at high energies or small distances, the quarks can be approximated as almost free particles (asymptotic freedom). At low energies or high distances the interaction between coloured particles get stronger, which ultimately leads to the confinement of colour charges within a colourless object. When the coupling α_s grows too large, calculations via a perturbative approach are no longer valid.

Electroweak Force

The second gauge group is also a non-abelian Lie-group, $\mathrm{SU}(2)_L$. The equation is almost identical to the QCD Lagrangian above:

$$\mathcal{L}_{weak} = -\frac{1}{4}\left(W^a_{\mu\nu}W^{a,\mu\nu}\right) + \sum_{\text{generations}} \bar{I}_L \not{D} I_L \ , \tag{1.9}$$

$$D_\mu = \partial_\mu - igW^a_\mu T^a \tag{1.10}$$

$$W^a_{\mu\nu} = \partial_\mu W^a_\nu - \partial_\nu W^a_\mu + g\epsilon^{abc}W^b_\mu W^c_\nu \ , \tag{1.11}$$

W^a are the gauge fields, g the coupling, T^a the three generators of SU(2) and I contains matter fields. Formally the charge of the matter fields under this group is called isospin, and I is an SU(2) doublet containing two quarks, or one lepton and one neutrino. The quarks are grouped into this doublet according to their flavour, where an up-type flavour coincides with an eigenvalue of T^3 of $1/2$ and a down-type flavour with an eigenvalue of T^3 of -1/2.

This force only couples to left-handed fermions with $I_L = (1 - \gamma_5)\, I$ and ϵ^{abc} is the totally anti-symmetric tensor in three dimensions i.e. the structure constant of SU(2). Left-handed means that the fermions have a negative chirality, i.e. the direction of their momentum is antiparallel to the direction of their spin. This non-abelian gauge group also gives rise to triple and quartic gauge couplings.

$U(1)_Y$ is an abelian symmetry group. Its Lagrangian $\mathcal{L}_Y$ is

$$\mathcal{L}_Y = \frac{1}{4} B_{\mu\nu} B^{\mu\nu} + \sum_{\text{flavours, generations}} \bar{\Psi} \not{D} \Psi \ , \tag{1.12}$$

$$D_\mu = \partial_\mu + i g' Y B_\mu \ , \tag{1.13}$$

$$B^a_{\mu\nu} = \partial_\mu B_\nu - \partial_\nu B_\mu \ , \tag{1.14}$$

where Y is the hypercharge of the fermion field Ψ. Left-handed fields have hypercharge -1 and right-handed ones -2. It is ,however, harder to associate these groups with any of the known forces directly, since the weak and electromagnetic forces as they are experienced at low energy scales only arise as a mixture of both $\mathrm{SU}(2)_L$ and $U(1)_Y$ symmetries after they are partially broken through the Higgs mechanism [10].

In order for this to occur a scalar field ϕ with a potential term and isospin $1/2$ is introduced, such that the ground state for this field has a non-vanishing vacuum expectation value:

$$\mathcal{L}_{Higgs} = (D_\mu \phi)^\dagger D_\mu \phi + \mu^2 \phi^\dagger \phi - \lambda (\phi^\dagger \phi)^2 \ , \tag{1.15}$$

$$D_\mu = \partial_\mu - \frac{ig}{2} \tau^a W^a_\mu + i \frac{g'}{2} B_\mu \ , \tag{1.16}$$

$$\phi = \begin{pmatrix} \phi_+ \\ \frac{v + H + i\varphi_z}{\sqrt{2}} \end{pmatrix} \ . \tag{1.17}$$

The Higgs field ϕ is parametrised with respect to its ground state $\phi_0 = (0, v/\sqrt{2})^T$, since it is a complex field the three field ϕ_+, H and φ_z are used. H and φ_z are real, while ϕ_+ has a real and imaginary part. This parametrisation if chosen in order to emphazise the ground state ϕ_0. λ and μ are constants with $v = \mu/\sqrt{\lambda}$. The ground state of the Lagrangian breaks the $\mathrm{SU}(2)_L \times \mathrm{U}(1)_Y$ gauge symmetry of the electroweak force to a residual U(1) symmetry, effectively leaving one massless U(1) gauge boson and three massive gauge bosons, the $W^\pm$ and Z bosons. The gauge boson for this residual U(1) symmetry is known as the photon and it is a mixed state of both B and W^3 fields. This leaves, according the Goldstone Theorem [11], one degree of freedom for a neutral Higgs boson.

Fermion Mass Term

The last ingredient for the full SM Lagrangian are the mass terms for fermions, which are believed to also originate through symmetry breaking, through a coupling to the Higgs field.

$$\mathcal{L}_{Yukawa} = -\bar{l}_L \phi Y_l l_R - \bar{q}_L Y_d \phi d_R - \bar{q}_L i \sigma_2 \phi^* Y_u u_R + h.c. \ , \tag{1.18}$$

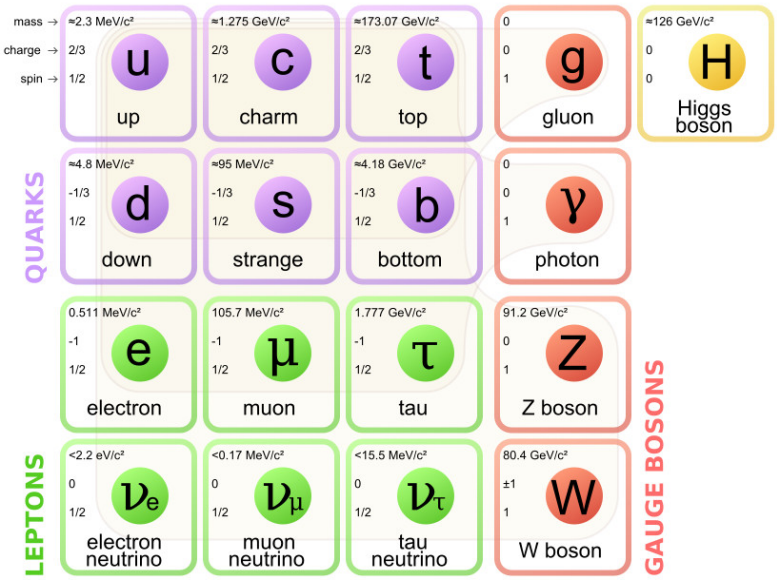

Figure 1.1.: The particle content of the SM. Figure taken from [13].

where Y_i are the Yukawa couplings, q contains the left handed quarks, and d_R/u_R contain the right-handed down/up-type quarks, while l_L contains the left handed leptons and left-handed neutrinos and l_R contains right-handed leptons. The Yukawa couplings are matrices in flavour space that are in general not diagonal, and in the SM up- and down-type Yukawa matrices cannot be diagonalised simultaneously. This gives rise to flavour-changing charged currents via the electroweak $W^{\pm}$ bosons proportional to the CKM matrix[1] [12] elements with $U_{CKM} = U_{L,u}U^{\dagger}_{L,d}$, where $U_{L,u/d}$ is the unitary transformation matrix diagonalising the u/d Yukawa matrix from the left side.

Due to some accidental global U(1) symmetries other quantities such as the baryon number and the electron, muon and tauon numbers are conserved.

An overview over the particle content of the SM is given in figure 1.1. There are three generations of fermions. The matter particles of each generation only differ in their respective masses, with each generation having a higher mass than the one before. All matter almost exclusively consists of the first generation of particles, which has the lowest masses. It is interesting to note that the SM itself gives no indication why there are three generations. In each generation there are two quark flavours, up-type and down-type, as well as 6 different colour states for each flavour. As mediator particles for the strong interaction there are 8 massless gluons. After spontaneous symmetry breaking, there is one massive Higgs boson, three massive bosons $W^{\pm}$ and Z for the mediation of the weak

[1] CKM stands for Cabibbo, Kobayashi and Maskawa, after the physicists who first suggested to introduce a quark mixing matrix.

force, and one massless gauge boson for the residual U(1) symmetry, the photon. Finally the SM contains one lepton per generation, denoted with electron, muon and tauon, as well as one left-handed neutrino per generation, the electron-, muon- and tau-neutrino.

Put together the SM Lagrangian density describes all elementary particles and their interactions with astounding precision. With the Lagrange densities the behaviour is determined through the principle of least action

$$S = \int d^4x \; \mathcal{L}_{SM} \; , \tag{1.19}$$

$$\delta S = 0 \; . \tag{1.20}$$

This however cannot be solved directly and particle physics instead relies on a perturbation series approach for its calculations. With Feynman diagrams the perturbation series can be written down pictorially. Quantum field theories have the additional peculiarity that they contain a series of ultraviolet divergences that have to be dealt with. This is done using regularisation, a mathematical recipe to parametrise the divergences, and renormalisation, a procedure to subtract the divergences into counter-terms. In principle this means that QFTs can predict the evolution of behaviour of the particles between two energy scales, but can make no absolute predictions at one particular scale.

1.1.2. Open Questions

There are several reasons why physicists generally believe that there has to be physics beyond the standard model. In this section some of these problems are discussed briefly.

- **Neutrino Mixing [14]:**
  The first problem concerns neutrinos and the masses of the fermions in general. Although the Higgs mechanism provides a convenient way to introduce masses to quarks and the charged leptons, the SM leaves the neutrinos massless. Neutrino masses can still be incorporated into the SM by introducing right-handed neutrinos and giving them a Dirac mass term, however doing this is not satisfying to most model-builders. This approach cannot explain why neutrino masses are as tiny as they are a few keV as opposed to MeV. There is also no satisfying explanation for the large mass differences between the three generations of particles, or for the mixing angles for quarks or neutrinos.

- **Unification [15]:**
  Another reason why the SM may only be a small energy approximation of a larger theory is condensed into the idea of unification. The weak and electromagnetic forces seem to be two different phenomena for sufficiently small energies. For energies above the electroweak breaking scale however, they combine into one force

under a larger symmetry group. The idea of unification then claims that if this works for the electroweak force, at sufficient high energies, all fundamental forces could be combined into one phenomenon. This hypothetical scale is called unification scale. This idea is aided by the fact that the energy dependence of the coupling constants of all three atomic forces have crossing points at high energies, though they do not combine at one point in the SM. Models that try to combine the forces of the SM are called Grand Unified Theories (GUT) although they usually do not take gravity into account.

- **Hierarchy Problem:**
  The hierarchy problem can be stated in many ways, such as why the Higgs mass is so small about 125 GeV [16], or why there is such a large difference between the Planck scale (10^{19} GeV) and the electroweak scale (10^{3} GeV). The problem can also be posed as the question why gravity is so weak compared to the electroweak force. The problem comes down to why the Higgs mass, which is not protected by any gauge symmetries in the SM, does not get corrected to a value near the Planck scale under loop corrections. Within the SM, this can only be solved by fine-tuning of parameters, which seems unnatural to many theorists. Supersymmetric models provide a nice solution to this fine-tuning problem, provided the Supersymmetric partners to SM particles have masses at the TeV scale, but warped extra dimensional models also provide solutions to this problem.

- **Dark Matter:**
  The existence of dark matter is hinted at by many measurements from astrophysics, for example the rotational curves of galaxies [17] can only be explained with a distribution of invisible mass throughout the galaxies. Such matter should consist of massive particles that interact only very weakly with the SM particles. The SM itself has no natural dark matter candidate, but theories like Supersymmetry do provide natural candidates for dark matter.

- **Gravitation:**
  The SM does not contain gravitation as a forth force. This makes no difference for particle interactions at low energies where most measurements take place, since gravity is so much weaker than the other three forces. However, a complete theory should also contain a fundamental description of gravity on the particle level.

1.2. Theories Beyond the Standard Model

In this section BSM theories that are important for this thesis will be discussed briefly. This account is therefore restricted to a few selected theory models.

1.2.1. Warped Extradimensional Models

Warped Extradimensional Models (WED) try to incorporate gravity as a forth force into the SM model. These theories are able to solve the hierarchy problem and usually still allow for a grand unification at some high energy scale. This section is based on references [18, 19]. The basic idea behind them is the following. There are two "branes" consisting of fourdimensional Minkowski space-time that are linked through a fifth, finite dimension. The wave functions of the normal SM particles, especially the Higgs boson, are now confined within their brane, called TeV brane. The graviton, however, can propagate through the "bulk" of the extra dimension, while the peak or its wave function is located on the other brane, called "Planck brane" (see figure 1.2). With this basic idea the gravitational force gets an exponential suppression due to travelling through the bulk. At the same time, the Higgs vacuum expectation value and with it its mass get also scaled down by an exponential factor, since the higgs is confined to the TeV brane the extra dimension can be integrated out of the five dimensional action.

In a more sophisticated theory some of the SM particles are allowed to propagate into the bulk too, giving them a coupling strength to gravity (i.e. mass) proportional to the overlap their wave function has with the graviton wave function.

This approach replaces the fine tuning of parameters on orders of magnitude with the tuning of order one parameters, i.e. the placement inside the bulk, thus getting rid of the hierarchy problem.

Properties

The most basic feature of all WED models is the extension of 3+1-dimensional Minkowski space to a fivedimensional space with the metric g_{MN}. The most general solution of the fivedimensional Einstein equations

$$R_{MN} - \frac{1}{2} R g_{MN} = 0 \ , \tag{1.21}$$

where R_{MN} is the Ricci tensor and $R = R^M_M$ the Ricci scalar is,

$$ds^2 = e^{-2kr(\phi)} \eta_{\mu\nu} dx^\mu dx^\nu + r^2 d\phi \ . \tag{1.22}$$

ds^2 is the line segment of the given metric and a solution for 1.22, ϕ parametrises the extra dimension and $\eta_{\mu\nu}$ is the Minkowski-metric, while r is the size of the extra dimension and k its curvature. Here curvature can only be understood in a purely mathematical sense, where it is closely connected to the second derivation of a path with respect to its parameters, see for example [20]. In order to arrive at this ds^2 matter is neglected and the solution is required to retain four-dimensional Minkowski space-time on the branes.

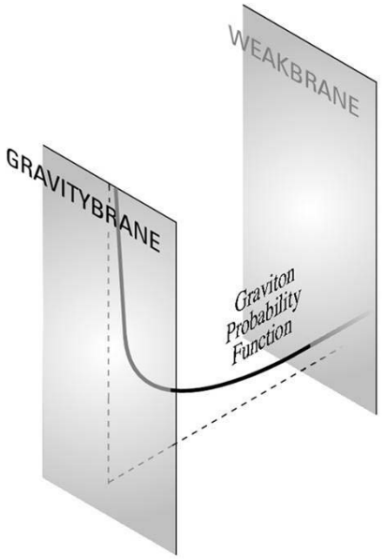

Figure 1.2.: Schematic picture of the two branes connected via a finite extra dimension. Here the Planck brane is called gravitybrane, and the TeV brane is called weakbrane. Figure taken from [19].

When integrating the extra dimension out of the five dimensional action, an exponential "warp factor" appears, effectively suppressing quantities like the vacuum expectation value v of the SM Higgs boson $v = v_0 e^{-\pi kr}$ with respect to its fivedimensional value v_0. In this case the Higgs potential from equation (1.17) is put into a 5D action and confined to the TeV brane. With this the hierarchy problem is solved if

$$kr \approx 11 \ . \tag{1.23}$$

Models of this kind introduce resonances with interesting features. These resonances are the excitation modes of the five dimensional metric g_{MN}. They can be decomposed into two different excitations

$$\delta g_{MN} = \begin{pmatrix} h(\phi, x)_{\mu\nu} & \vec{0} \\ \vec{0} & h(x, \phi)_5 \end{pmatrix} \ , \tag{1.24}$$

a spin-2 excitation $h(\phi, x)_{\mu\nu}$ of Minkowski-space in general these excitations are referred to as gravitons, and a spin-0 excitation $h(x, \phi)_5$ along the fifth dimension, called a Radion. Such excitation X can be decomposed into their fourdimensional wave functions $X^{(n)}(x)$ and the functions $f^{(i)}(\phi)$, called profile functions that describe the behaviour in the extra dimension

$$X(x, \phi) = \sum_n^\infty X^{(n)}(x) f_X^{(n)}(\phi) \ . \tag{1.25}$$

The profile functions and have a series of roots depending on kr. Usually the two parameters chosen to describe the theory are $\tilde{k} = k/\overline{M}_{Pl}$, with the reduced Planck mass $\overline{M}_{pl} = M_{pl}/\sqrt{8\pi} \approx 2.4{\times}10^{18}$ GeV, and the mass of the first resonance. $\tilde{\text{k}}$ is also commonly called coupling because it naturally appears as a parameter when the fivedimensional Lagrangian of matter fields is expanded around the excitation modes of g_{MN}.

The periodic root structure of the profile function leads to standing waves inside the warped dimension. Each of these standing waves has mass corresponding to the roots of the profile function thus resulting in a tower of resonances observable on the TeV brane. The resonances belonging to such a tower of resonances are called a KK-resonances [2]. In order for $kr \approx 11$ to hold the first KK-resonance of this kind should have a mass of a few TeV.

This thesis considers two warped extra dimensional models, the RS1 [3] model which considers every SM particle to be confined on the TeV brane (as shown in figure 1.2), and the Bulk-Graviton scenario, where the $\text{SU}(2)_L \times U(1)_y$ symmetry is expanded to reach into the bulk (see figure 1.3). For the case of bulk models, each SM particle allowed to propagate into the bulk causes a tower of KK-modes. The first, massless, resonance is assumed to be the normal SM particle, while the higher excitations only play a role in loop corrections at low energy scales. There are far more models suggesting a wide range of possible scenarios, however for the case of high energy physics searches it is advantageous to take relatively simple models that can stand in for a class of more sophisticated models.

1.2.2. Heavy Vector Triplet Models

Another benchmark model considered in this thesis is the Heavy Vector Triplet (HVT) model. This benchmark model is a spin-1 vector triplet, that is basically analogous to the weak force of the standard model. This scenario, describes an exotic resonance that can be either a charged or neutral spin-1 resonance, can arise in different theoretical scenarios. For example in composite Higgs models, where the Higgs boson is thought to be a composite particle emerging from the breaking of an overlying symmetry, a triplet of heavy spin-1 resonances are predicted that can be described by the HVT model [27]. The neutral spin-1 resonance is usually called Z', while the charged resonance is called W'. The HVT model is a simplified model which can describe the important qualities of a spin-1 resonance from the experimental point of view, without introducing too many contraints on the theoretical model the resonance can arise from. This is done using an effective Lagrangian and a parametrisation of all couplings that are used for limit setting. Two slightly different models are distinguished, they are commonly referred to as HVT

[2] KK stands for Kaluza and Klein, who first predicted such resonances in extra-dimensional models [21, 22].

[3] RS stands for Randall and Sundrum. The properties of such models are found in references [1, 23–25].

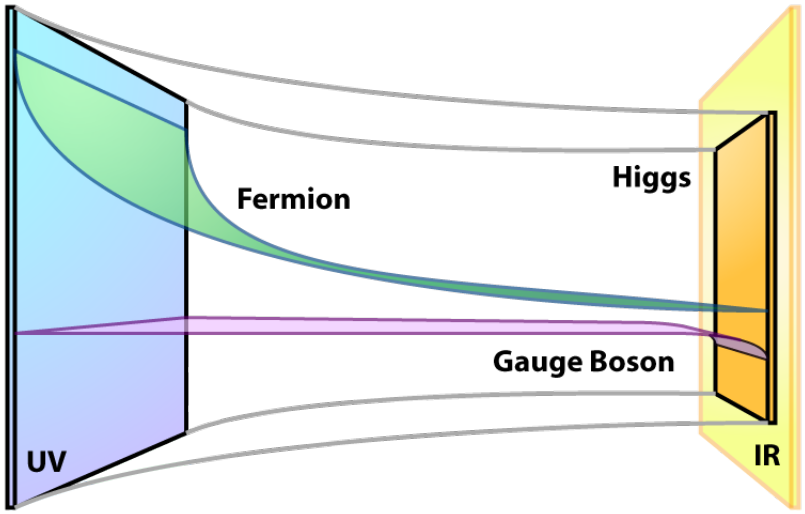

Figure 1.3.: Schematic picture of the two branes connected via a finite extra dimension in the Bulk-Graviton case, where the fermions and the electroweak bosons are extended into the bulk. In this case the Planck-brane is denoted with UV and the TeV brane with IR. Figure taken from [26].

model A and B. The difference between the two models lies in the coupling strengths to the fermion sector. These are suppressed in model B, while the couplings to fermions and gauge bosons are of similar strengths in model A.

1.2.3. Phenomenology at the Large Hadron Collider

In order to either discover one of the predicted exotic resonances or give exclusion bounds on the signal strength, the phenomenology of these models at the Large Hadron Collider is of great importance [28, 29]. The power of a physics analysis depends on the production mode, the coupling strengths to the considered final state, and other model specific quantities. Table 1.1 contains an overview of some of the important properties of the used benchmark theory models.

For WED spin-2 models the two parameters $\tilde{k}$, which is essentially the curvature of the extra dimension, and the first KK-resonance mass m_X are used to parametrise the models. In case of the HVT models, the generic phenomenological Lagrangian can be parametrised by the resonance mass m_X and the coupling to fermions c_F, to bosons g_V, and to the Higgs boson c_H. The Radion model can be parametrised the same way as the spin-2 WED resonances, by using the first KK-resonance mass as well as the coupling $\tilde{k}$, or alternatively kr where r, which is sometimes denoted as L, is the size of the extra dimension. Phenomenological parameters such as the decay width of the

Table 1.1.: Overview over the important qualities of the benchmark theory models used in this analysis. The letter l stands for longitudinally polarised vector bosons, t stands for transversal polarisation. The column PRODUCTION lists the production modes used for the MC samples. For MC generation, the dominant production mode, either gluon fusion (GF) or Drell-Yan (DY), was used.

BENCHMARK MODEL	SPIN	PRODUCTION	COUPLING TO VB	THEORY CLASS
RS1-Graviton	2	87% DY 13% GF	90% t 10% l	WED
Bulk-Graviton	2	GF	l	WED
W′	1	DY	l	HVT
Z′	1	DY	l	HVT
Radion	0	GF	l	WED

resonance and the cross section depend quadraticlly on the choice of $\tilde{k}$. The branching fractions, however, are independent of the exact parameter choices.

In the case of a spin-0 resonance, i.e. in the case of the Radion model, an interference with the SM Higgs boson is predicted by some models. Such a mixing can quite drastically change the couplings of the Radion to SM particles [30]. Since the interference also changes the phenomenology for the Higgs boson, severe restrictions on the coupling strength to the SM Higgs boson can be set, see for example reference [31]. A mixing with the SM Higgs boson would lead to a decline in coupling strenght to vector bosons, thus requiring a minimum of 50 fb^{-1} for a detection at the LHC with $\sqrt{s} = 14$ TeV. In the following a model without mixing with the SM Higgs boson is used.

Production

Since the Large Hadron Collider (LHC) is a proton-proton collider the important production modes of all considered models are either through Drell-Yan (DY) or gluon fusion (GF) processes (see figure 1.4). Although the considered models share a high branching ratio to vector bosons, the production mechanisms of vector boson fusion (VBF) and vector boson associated (VBA) production are negligible compared to the other two production modes. This is due to the presence of additional weak vertices and the high mass of the expected resonance, which lead to a small phase space. In figure 1.5 the production cross sections for all considered benchmark models are displayed as a function of the resonance mass for a given coupling. It can be seen that DY and GF production are the most important production mechanisms. In the Bulk-Graviton and the Radion theory models gluon fusion surpassed DY production since the coupling of both exotic particles are proportional to the fermion masses, as is the case with the SM Higgs boson. This means, that the coupling to top-quarks is the strongest, but the production via $t\bar{t}$ pairs is suppressed through the PDFs of the proton, while the gluon fusion via a top-quark

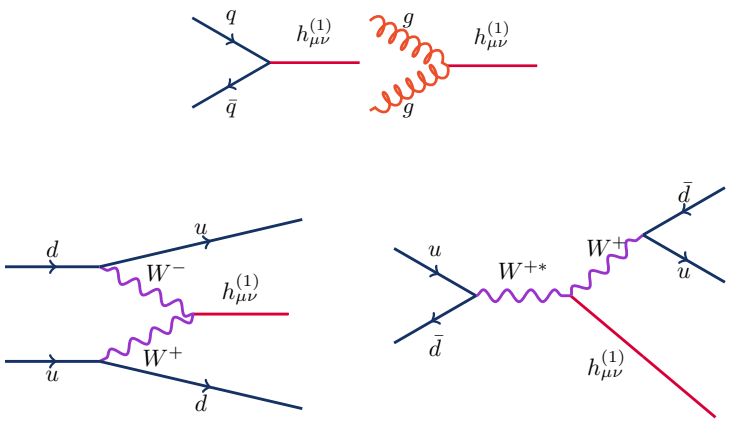

Figure 1.4.: The Feynman graphs for DY and GF production of a hypothetical spin-2 resonance (top). The Feynman graphs for Vector Boson Fusion (VBF) and Vector Boson Associated (VBA) production are shown on the bottom. This figure is taken from [19].

loop becomes the dominant production process. For the two HVT resonances a direct coupling to gluons is impossible due to the spin structure. In case of the W′ a direct coupling to gluons would also violate electric charge conservation. The production cross sections also drastically decrease with the resonance mass.

Decay Modes

The branching ratios to different final states can be seen in figure 1.6, for different theory models. The branching into vector bosons, which is the most important for this thesis, has a significant fraction for all models except for HVT model A, which was designed to maximise the couplings to the fermion sector. This benchmark model is not used in the following analysis. In addition to having one of the largest branching ratios for all considered theory models, the vector boson channel has the additional advantage of the existance of recently developed and highly effective techniques do deal with boosted topologies.

In all of the above mentioned theory models with the exception of the RS1-Graviton model, the coupling strength are vastly different. Most models derive a volume suppression for the coupling to the transverse degrees of freedom, while the longitudinal degrees of freedom that arise from electroweak symmetry breaking have couplings proportional to the mass of the vector bosons. The decay ratios given here are for longitudinally as well as transversally polarised vector bosons.

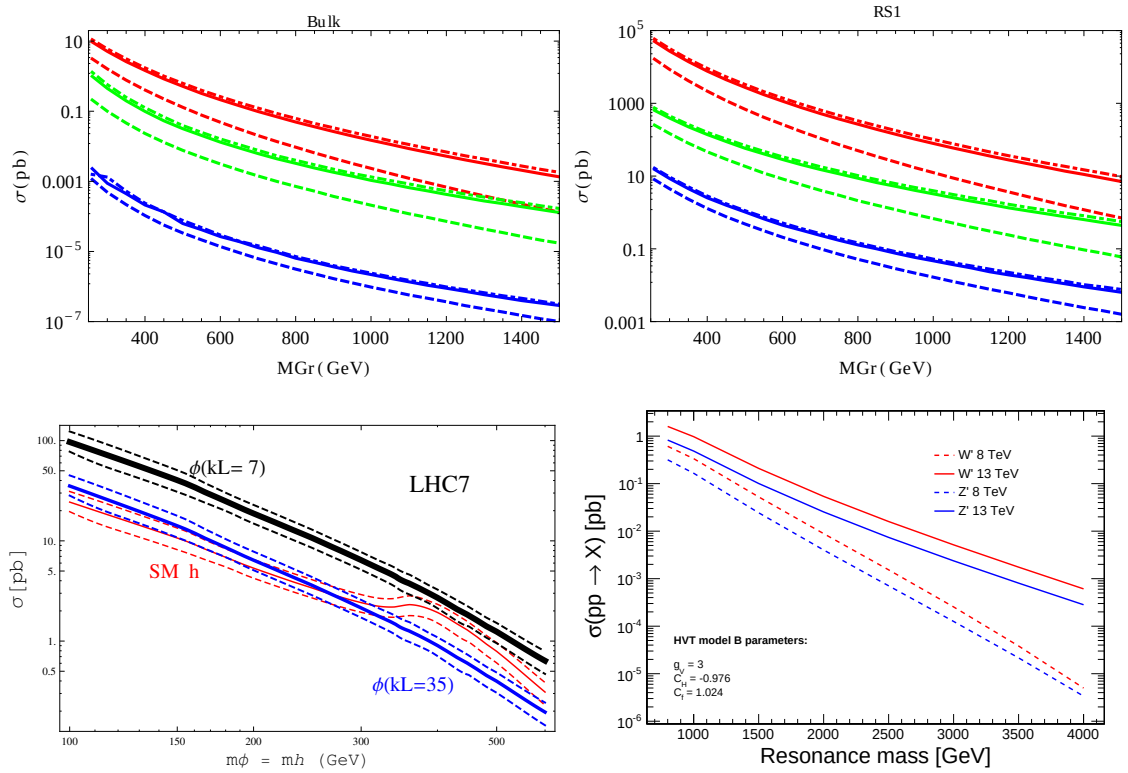

Figure 1.5.: The expected production cross sections for different theory models as a function of the resonance mass MGr or $m\phi$. Top left is the production for Bulk-Graviton and on the top right the one for the RS1 model (taken from [19]) with $\tilde{k} = 0.2$. The red curve corresponds to the inclusive production at the LHC, the green and blue ones to VBF and VBA production. Dot-dashed, continuous and dashed line styles correspond to center of mass energies of 14 TeV, 13 TeV and 8 TeV respectively. On the bottom left is the production cross section for a Radion model, taken from reference [32]. This cross section is given at 7 TeV center of mass energy for GF and $kL = 35$ (solid blue line) or $kL = 7$ (solid black line), the dashed lines represent theory uncertainties. On the bottom right the inclusive production cross sections for both HVT resonances in Model B are shown for 8 TeV center of mass energy (dashed line) and 13 TeV center of mass energy (solid line). The figure is taken from reference [33].

In the case of the RS1-Graviton model the suppression factor for transverse degrees of freedom is simply 1, which means that the decay rate primarily depends on the phase space of the decay.

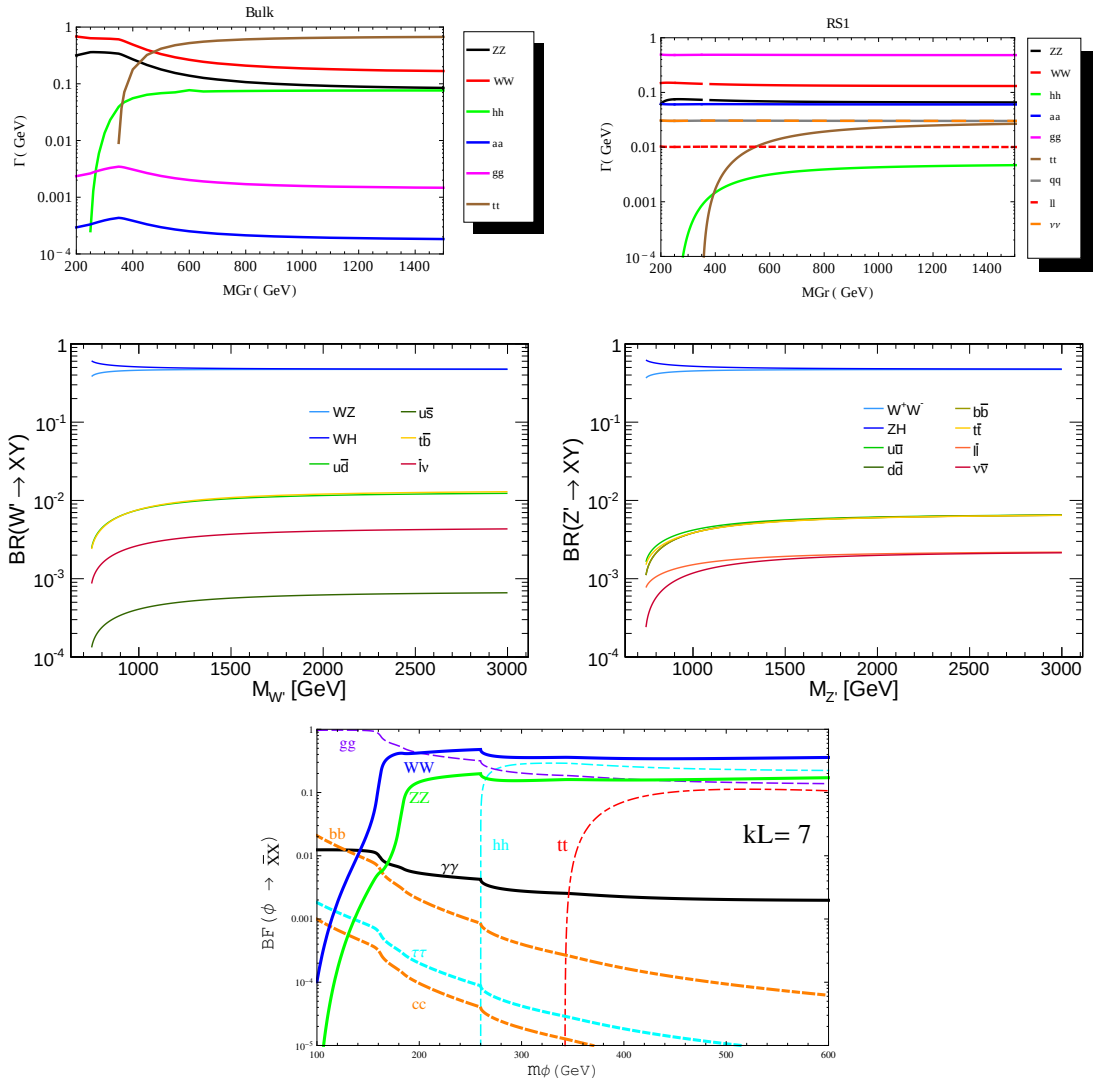

Figure 1.6.: Branching ratios for different benchmark theory models; from top left to bottom right they are Bulk-Graviton, RS1-Graviton [19] with a coupling $\tilde{k} = 0.2$. Below are branching ratios for W′ (left) and Z′ (right) taken from [33]. On the bottom are the branching ratios for a Radion model [32]. The ratios are given as functions of the resonance mass.

2. The Large Hadron Collider and the Compact Muon Solenoid Detector

In order to test the validity of the standard model and search for physics beyond the standard model, particle physics has to be tested at high energy scales, where the effects of new physics become apparent. The Large Hadron Collider (LHC), as of today the world largest scattering experiment, was built to search for new physics at a maximum center-of-mass energy of $\sqrt{s} = 14$ TeV. The scientists analysing LHC data have already successfully announced the discovery of the Higgs boson in 2012. The search for new physics beyond the standard model continues with the new data from 2015, which is the first data taken at a center-of-mass energy of 13 TeV.

For this thesis data taken with the Compact Muon Solenoid (CMS) detector from proton-proton collisions at a center-of-mass energy of $\sqrt{s} = 13$ TeV are used with an integrated luminosity of 2.1 fb^{-1} (2.6 fb^{-1}). This chapter contains a brief summary of the properties of the LHC and the CMS experiment. The first section (2.1) deals with the LHC. In section 2.2 a brief description of the CMS particle detector and its subsystems is given.

2.1. The Large Hadron Collider

The Large Hadron Collider [35] is a scattering experiment designed to give an insight into particle physics at the TeV scale. The collider itself is located at the European Organisation for Nuclear Research (CERN) at Geneva, Switzerland, and consists of a 26.7 km ring built almost 100 m underground. The collider was built in a preexisting tunnel previously occupied by the Large Electron-Positron Collider (LEP) and can reach a maximum center-of-mass energy of 14 TeV and a peak luminosity of 10^{34} cm^{-2}s^{-1}. These peak values can only be reached for proton-proton collisions but the collider can also be operated with heavy ions. The LHC is built with two different beam lines, where the protons are accelerated in opposing directions. A total of 1232 superconducting dipole magnets, which are cooled to a temperature of 2 K and have an 8 T magnetic field, are used to control the protons in the beam line. In addition about 4800 corrector magnets are necessary to correct the beam position, bunch localisation and focusing. High frequency cavities with a fundamental frequency of 400 MHz are used for the final acceleration and

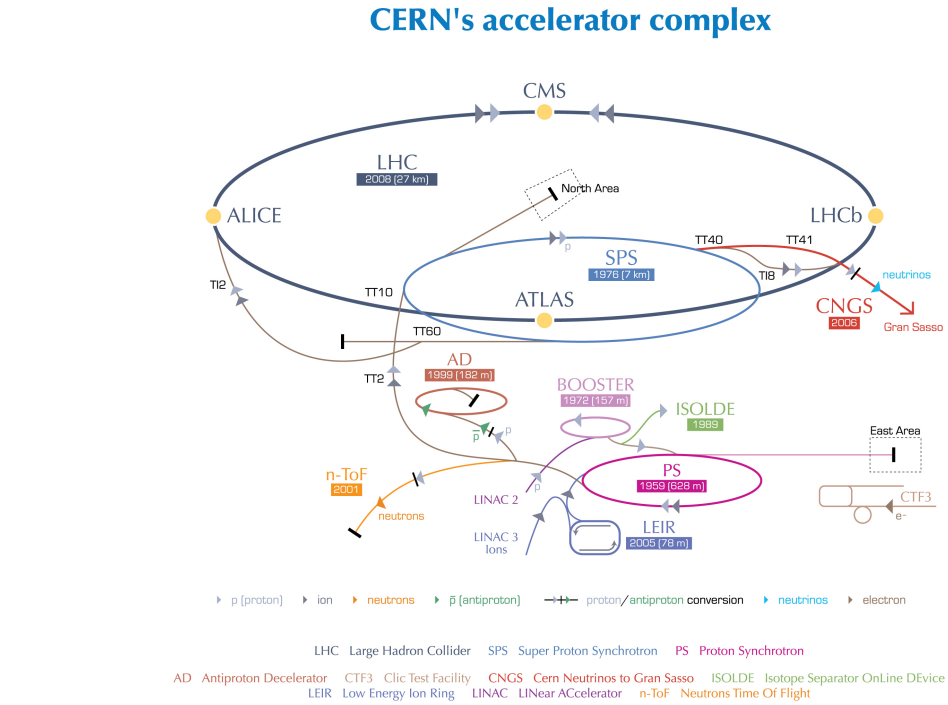

Figure 2.1.: A schematic of the structure of the LHC. The figure shows the position of the four main experiments, as well as the schematic location of the multiple preaccelerators, figure taken from reference [34].

storage of the protons. The protons are inserted into the main ring only after passing through a series of four preaccelerators. In figure 2.1 a schematic of the LHC ring is shown. The LHC has a total of 8 straight sections for potential interaction points, two of which are reserved for beam cleaning and one for the dumping of the beam. Only four of the interaction points are surrounded by particle detectors. CMS [36] at interaction point 5 and A Toroidal LHC ApparatuS (ATLAS) [37] at interaction point 1 are multipurpose detectors designed for proton-proton interactions at high luminosities. Both experiments have a large physics programm from SM precision measurement, the Higgs boson search to searches for dark matter particles. A Large Ion Collider Experiment (ALICE) [38] at point 2 is a detector specialised on heavy ion collisions to investigate the conditions and characteristics of a quark-gluon plasma. Lastly, LHCb (LHC beauty) [39] at point 8 was built to investigate the physics of b-hadrons, especially CP-violating processes involving b-quarks.

At this point in its operation the LHC manages to reach a number of 2808 bunches per proton beam with a bunch spacing of 25 ns and about 10^{11} protons per bunch. This results in an average of 21 proton-proton interactions per bunch crossing, which forces experiments to put a focus on the removal of particles coming from a different proton interaction from the main event, called pileup. The luminosity, which provides a measure for the number of particle collisions per time unit, depends on the number of bunches n_b, the frequency f with which they run around the accelerator, the number of particles N_b per bunch and the area of a bunch given, by $\sigma_x\sigma_y$ since the bunches are nearly Gaussian, $\sigma_{x,y,z}$ is the standard deviation of the gaussian beam profiel in $x/y/z$ direction. The luminosity is then given by

$$\mathcal{L} = \frac{N_b^2 n_b f \gamma_r}{4\pi\sigma_x\sigma_y} F \ , \tag{2.1}$$

$$F = \left(1 - \left(\frac{\theta_c \sigma_z}{2\sigma^*}\right)^2\right)^{-\frac{1}{2}} \ , \tag{2.2}$$

where F is an additional reduction factor due to the crossing angle θ_c at the collision point. γ is the relativistic gamma-factor and σ^* the transverse beamsize at the interaction point. The integrated luminosity L is

$$L = \int \mathcal{L} dt \ , \tag{2.3}$$

and can be used to calculate the number of events N expected for a particular process with cross section σ:

$$N = L\sigma \ . \tag{2.4}$$

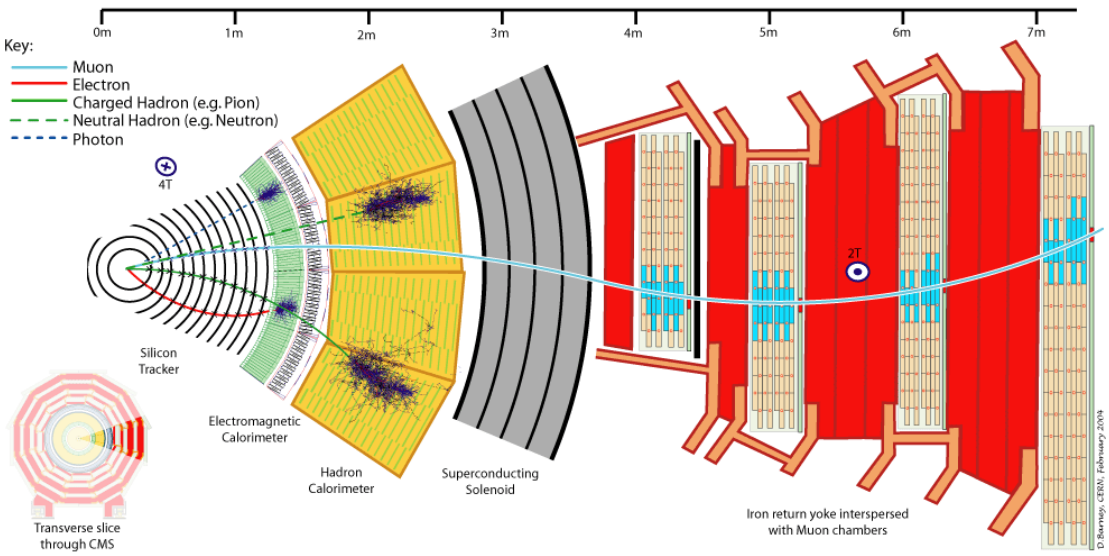

Figure 2.2.: A schematic cut through the CMS detector, taken from [40]. Starting from the interaction point the subdetector systems of tracker, ECAL, HCAL and the iron return yoke with the muon system can be seen. As an illustration the paths of a muon, electron, pion, neutron and photon are pictured as well as their interactions with the detector.

2.2. The Compact Muon Solenoid Experiment

The CMS detector [36] is approximatly cylindrical around the beam direction. It has a diameter of 14.6 m and a length of 21.6 m, and it weighs 12.500 tons, which makes it relatively compact in comparison to other particle detectors. The experiment consists of four subsystems, which in turn contain many subdetectors, of which three, the tracker, the Electromagnetic Calorimeter (ECAL) and the Hadron Calorimeter (HCAL) are contained inside a superconducting magnet generating an almost constant magnetic field of 3.8 T. The muon system is situated both directly inside and on the outside of an iron return yoke designed to guide the magnetic field lines. See figure 2.2 for a schematic cut through the CMS detector.

In the following sections a coordinate system is used defined by setting the origin at the collision point, the z-axis along the anti-clockwise beam direction, the x-axis pointing to the center of the LHC and the y-axis pointing upwards perpendicular to the plane of the LHC. The quantities θ, r and ϕ define a spherical coordinate system as follows. θ is the angle measured from the z-axis, ϕ is the azimuthal angle measured from the x-axis, and r is the distance to the interaction point. Another important detector variable is the rapidity y, i.e. the boost along the beam axis that transforms from the lab frame to a

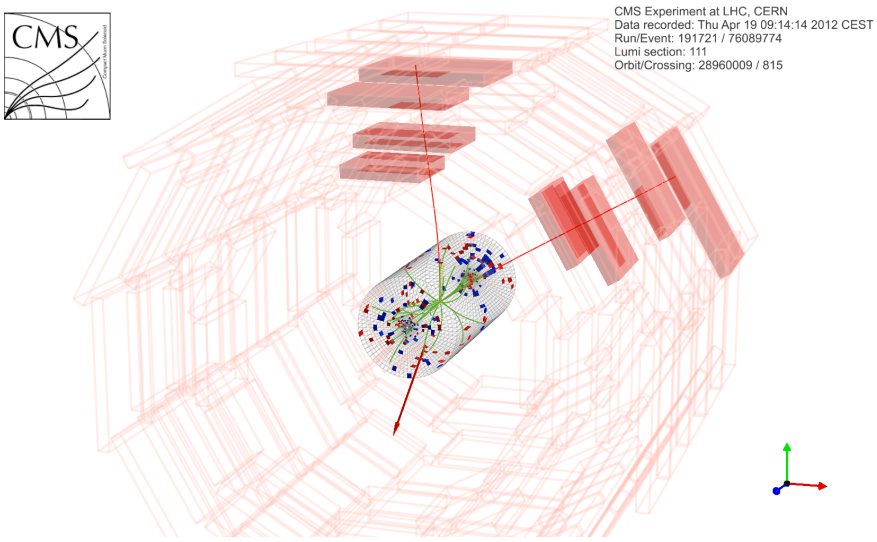

Figure 2.3.: An event display [41] from the CMS detector at a center-of-mass energy of 8 TeV. The display shows an event with two W bosons decaying into muons and neutrinos. The missing transverse energy is indicated with a red arrow.

frame where the particle moves only orthogonal to the beam axis

$$y = \frac{1}{2}\log(\frac{E + p_z}{E - p_z}) \ . \tag{2.5}$$

Here E is the energy of a particel while p_z is its momentum in z-direction. Along width the rapidity the pseudorapidity η

$$\eta = -\log(\tan(\frac{\theta}{2})) \tag{2.6}$$

is often used in measurements since it only depends on the polar angle of a particle and not its energy. The pseudorapidity can therefore be used to discribe the particles absolute location in the detector system. For massless particle η and y coincide. The quantity ΔR

$$\Delta R = \sqrt{(\Delta\eta)^2 + (\Delta\phi)^2} \tag{2.7}$$

is a measure of the angular distance of two particles. The transverse momentum of a particle is defined as

$$p_{\mathrm{T}} = \sqrt{p_x^2 + p_y^2} \ . \tag{2.8}$$

In figure 2.3 a typical event with two leptonically decaying W bosons is shown as an event display, i.e. the energy deposits in the ECAL and HCAL are shown as red/blue boxes, the tracks are shown as lines inside the tracker system, and the hits in the muon system are shown by highlighting the detector pannel that registers the hit.

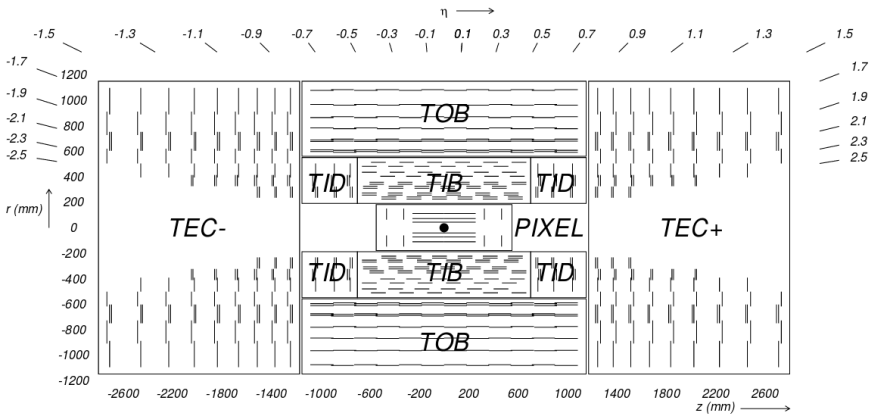

Figure 2.4.: A schematic layout of the CMS tracker, figure taken from [44]. The figure depicts the tracker in the coordinate system given by η, r and z. At the center lies the interaction point (black dot), which is surrounded by the pixel detector. The barrel part of the detector consists of the tracker inner barrel (TIB) and tracker outer barrel (TOB), while the endcaps are made of the tracker inner disc (TID) and tracker end caps (TEC). Each black line indicates a detector module.

2.2.1. Tracker

The CMS tracker [42,43] is situated directly around the beam axis, closest to the interaction point, and made entirely out of silicon. The tracker has an active silicon area of 200 m^2 and consists of an inner layer of silicon pixel detectors surrounded by another layer of silicon strip detectors. The whole detector has a total of 75 million readout channels. Both types of detectors are developed to result in high spatial resolution and response time, while at the same time the detector material is kept as sparse as possible to avoid multiple scattering or bremsstrahlung losses inside the tracker. This has to be balanced against the need for cooling, since the tracker produces a substantial amount of heat. These detector parts are also subjected to the highest particle fluxes and have to be as resistant to radiation damage as possible. The overall goal of the tracking system is an as precise as possible reconstruction of charged particle tracks, which are used to measure the direction and the magnitude of the particle momenta as well as the charge itself. These measurements rely on the bend in the particle tracks due to the 3.8 T magnetic field. A schematic layout of the CMS tracker is shown in figure 2.4.

Silicon Pixel Detector

The silicon pixel detector consists of around 65 million pixels made of 100×150 μm^2 silicon cells. If a charged particle hits one of those pixels it creates electron-hole pairs inside the semiconductor material. This gives rise to a small electric signal, which gets amplified and measured by readout chips mounted to the pixels-chips. The silicon pixel detector reaches a resolution of 15-20 µm in all spatial directions and covers a range of $|\eta| < 2.5$. The information of this subdetector is amongst other things used for a fast 3D reconstruction of the interaction vertices.

Silicon Strip Detector

The silicon strip detector is situated in 10 layers around the pixel detectors and is arranged to give a high spatial resolution in every direction when combining the measurements from two adjoining layers. These detectors work in the same way as the silicon pixel detectors but provide a spatial resolution of about 20 µm in the plane spanned by r-ϕ and of about 200 µm in the r-z plane.

2.2.2. Calorimetry

In contrast to the tracking system the main goal of the calorimeters is an energy measurement, which means that the particles should ideally be absorbed completely inside the detector material. Through interactions with the detector material the incoming particle produces a shower of secondary particles with decreasing energies. These particles deposit their energy in the detector by exciting or ionizing the atoms inside the detector material or they produce shower-particles themselves. The energy deposited by all shower-particles is proportional to that of the incident particle. Both the Electromagnetic Calorimeter (ECAL) and the Hadron Calorimeter (HCAL) of CMS operate under these principles.

Electromagnetic Calorimeter

The ECAL is situated in the next layer surrounding the tracker and consists of around 76 000 lead tungstate ($PbWO_4$) crystals, which work as a scintillating as well as an absorber material. A schematic picture of the CMS ECAL is shown in figure 2.5. The ECAL's primary purpose is the energy measurement of particles interacting through QED processes, like electrons or photons. For energies above about 10 MeV the interaction of electrons with the detector material leads primarily to the emission of bremsstrahlung

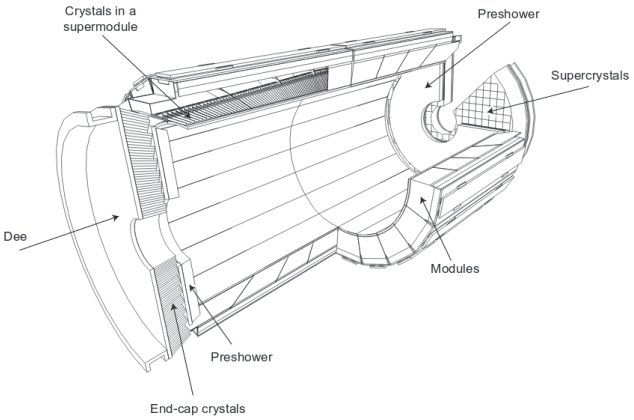

Figure 2.5.: The layout of the CMS ECAL, figure taken from [45]. In the barrel region the ECAL is made of modules comprised of lead tungstate crystals. In the endcap region an additional material the preshower is put before the crystals.

photons, while the interaction of photons with the detector leads to the production of electron positron pairs. This leads to the generation of showers consisting of secondary particles with decreasing energy until the energy of the shower particles falls under a critical value. The remaining energy is deposited in the detector material either by ionisation or thermal excitation in the case of electrons, or compton scattering and the photo-electric effect in the case of photons. In a scintillator material such as the one used for the CMS ECAL the excited atoms of the detector material emit photons of a specific wavelength for which the crystals are transparent. The total energy deposit is proportional to the number of photons, which are detected and converted into electrical signals by a series of photodetectors.

Many characteristics of electromagnetic showers can be described by the radiation length X_0, which is a material-specific constant defined by the energy loss of an electron to $1/e$ of its original energy. The lead tungstate crystals have a radiation length of 0.89 cm. The material was chosen to have a small radiation length in order to place the ECAL inside of the magnetic coil.

The transversal size of an electromagnetic shower is primarily given by multiple scattering of electrons and positrons and the subsequent bremsstrahlung from those scattered particles, which leads to relatively small spreads. The transverse spreads integrated over the whole shower are given by the Molière-radius R_M

$$R_M \approx \frac{21 \text{ MeV } X_0}{\epsilon} , \tag{2.9}$$

where ϵ is the critical energy of the material at which the energy losses of electrons due to bremsstrahlung and thermic excitation are equal [46]. The CMS ECAL has a small

Molière-radius of $R_M = 2.2$ cm.

The energy resolution of a calorimeter is given by

$$\frac{\sigma(E)}{E} = \sqrt{\left(\frac{a}{\sqrt{E}}\right)^2 + \left(\frac{b}{E}\right)^2 + c^2} \,. \tag{2.10}$$

The three constants a, b, c are dependent on the specific detector. The contributions in equation (2.10) have different sources. The $1/\sqrt{E}$ dependence is due to statistical fluctuations in the showering process and fluctuations in the number of photons detected in the photomultipliers and therefore called the stochastic term. The second term is the noise term and is mainly due to electronic noise in the readout chain. The third term is related to imperfections in readout, the detector geometry or the aging of detector units, in short everything that gives rise to contributions that do not depend on the particle energy.

Hadron Calorimeter

Similar to the processes in the ECAL particles also produce showers due to interactions with the material of the hadron calorimeter. Here the interactions are often QCD processes, which allow the detection of both charged and neutral hadrons. However, due to the production of neutral pions, which usually decay into two photons before they can interact strongly, a significant portion of energy gets deposited by purely electromagnetic interactions. The HCAL at CMS [47] consists of many layers of absorber materials alternated with scintillating materials. These scintillators are in turn connected to the readout apparatus. A special challenge for the HCAL is the large anglular range it has to cover in order to be able to measure the overall energy of an event as complete as possible. With this guaranteed CMS can use missing transverse energy measurements i.e. if the total energy deposits transverse to the beam direction do not sum up to zero, the missing amount of energy is called missing transverse energy. The HCAL consists of a calorimeter in the barrel region, one in the endcap region and a special forward calorimeter (HF), covering in total a pseudorapidity range of $|\eta| < 5.2$. The HF is a Cherenkov detector, utilizing the radiation of light from charged particles faster than the speed of light inside the material of the detector. This has the effect that only charged particles with sufficiently high velocities can be measured in the forward region. In this region a Cherenkov detector was chosen because of its radiation hardness. Similarly to the radiation length in the electromagnetic calorimeter an interaction length λ_0 can be defined for the hadronic particles. The energy resolution of the HCAL can be modelled by a stochastic and a constant term according to [47]

$$\frac{\sigma E}{E} = \sqrt{\left(\frac{a}{\sqrt{E}}\right)^2 + b^2} \,. \tag{2.11}$$

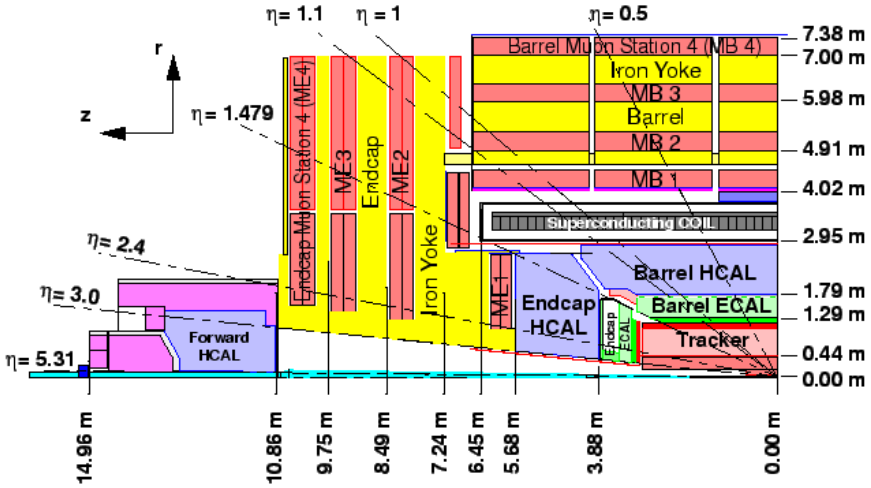

Figure 2.6.: A horizontal and vertical slice through the CMS detector, taken from [48]. The position of the main HCAL as well as the forward calorimeter are shown. The positions of the muon system as well as the iron return yoke and the superconducting coil are depicted.

For the CMS HCAL brass was chosen as an absorber material both because of its small interaction length $\lambda_0 = 16$ cm and its non-magnetic properties.

2.2.3. Muon System

Muons leave the detector system without being stopped in the calorimeters. This is due to the significantly lower energy loss through bremsstrahlung, which depends on the inverse of the particle mass and the long livetime of the muon, that allows it to leave the detector before it decays. In order to distinguish muons from other charged particles and to get a better measurement of their momentum, a system of muon detectors provides the last layer of the detector. The muon system consists of drift chambers in the barrel region, which are layered inside the iron return yoke, and cathode strip chambers in the endcap region. Interleaved layers of resistive plate chambers (RPC) are used as a trigger for the muon subsystem. The muon detectors measure a current when the muons ionize the gas inside the detectors in passing. With exception of the measurements from the RPC, these measurements can be used for tracking.

2.2.4. Triggering

Since at normal operation of the LHC there is a bunch crossing every 25 ns, with around 20 collisions each, the amount of produced data far exceeds the storage capabilities. Therefore a system is needed that quickly distinguishes between interesting events, which should be kept for future analyses, and those that can be discarded. For this purpose CMS has a trigger system containing the Level-1 (L1) trigger and the high level trigger (HLT). The L1 trigger is a hardware trigger that mainly relies on the data from the calorimetry and the muon system as well as availability of subsystems. The HLT is software based and uses information from all detector systems to further reduce event numbers. The combination of both triggers diminish the number of recorded events by about 10^5 allowing a pre-selection of data.

2.2.5. Computing Infrastructure

The Worldwide LHC Computing Grid (WLCG) [49,50] is built to distribute the collected data to analysis groups around the world. The WLCG has a hierarchical structure with one Tier-0 center at CERN laboratory, 13 Tier-1 centers around the world - one of them at the KIT- and many more Tier-2 and Tier-3 centers.

In figure 2.7 a schematic overview over the grid structure is provided. The primary task of the Tier-0 center is the safekeeping of the raw detector data as well as a first pass at reconstuction. These data get distributed to Tier-1 centers, via an optical-fiber network working at 10 gigbits per second. The Tier-1 centers distribute data to Tier-2 centers, store raw-data and processed data from CERN and process the raw-data further. Tier-2 centers are usually university clusters capable of handling the production of simulated events. Scientists can also gain access to the grid infrastructure through local (Tier-3) computing resources.

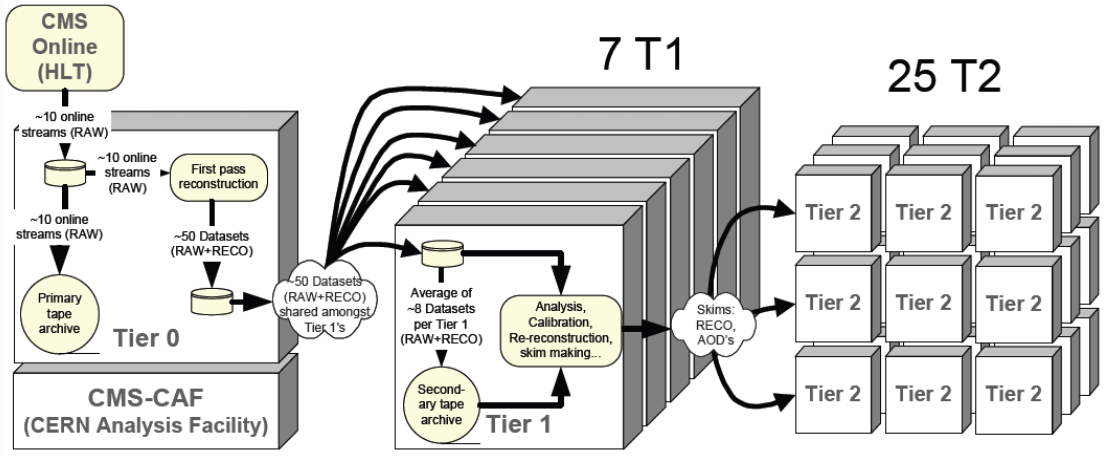

Figure 2.7.: Schematic flow of raw experimental data in the CMS computing model, figure taken from [49]. The distribution of data begins with the measuring and saving of events that pass the CMS HLT triggers. This data is either directly saved or passed through a first reconstruction procedure. The CERN Analysis Facility is responsible for calibration and alignment. From the central Tier-0 center the data gets distributed first to Tier-1 centers and from there further to Tier-2 and 3 centers.

3. Event Reconstruction and Simulation

This chapter gives an overview of the generation of simulated events and the reconstruction of measured events inside the detector. The first section contains a brief description of the characteristics of a proton-proton collision. Section 3.2 deals with the reconstruction of events inside the CMS detector. Section 3.3 describes the simulation of events using Monte Carlo (MC) event generators.

3.1. Characteristics of Proton-Proton Collisions

The LHC is a proton-proton collider. This means on the one hand that the accelerator can reach high center-of-mass energies of $\sqrt{s}$ of 14 TeV, which would in this configuration not be possible with an electron-positron collider due to synchrotron radiation. On the other hand collisions involving protons are more complicated for a number of reasons that are going to be discussed in the following sections. Due to the composite nature of the proton, its constituents take part in the scattering process. This leads to challenges concerning the modelling of the composite structure itself, the existence of proton remnants and the unknown fractions of the protons energy the parton (quark/gluon) involved in the hard process in question are carrying. Figure 3.1 shows a schematic of a proton-proton-collision.

3.1.1. Hard Process

The interaction on parton level with the highest momentum transfer in an event is called *hard process*. It can be approximately calculated in quantum field theory as

$$d\sigma(k_1 k_2 \to \sum_k p_k) = \frac{1}{4\sqrt{(k_1 \cdot k_2)^2 - m_1^2 m_2^2}} \cdot d\mathrm{LIPS}|\mathrm{ME}|^2 \ , \tag{3.1}$$

where LIPS denotes the Lorentz-invariant phase space and ME is the matrix element calculated to some order in perturbation theory using the Feynman rules derived from the interaction Lagrangian of the SM or some model with BSM physics.The four-momentum

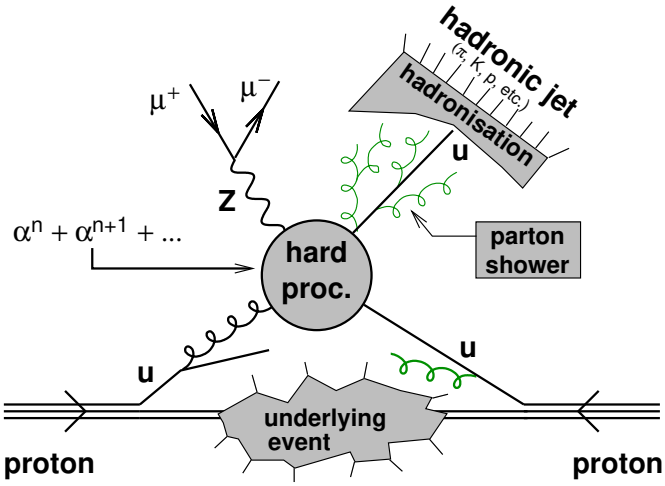

Figure 3.1.: A schematic of a proton-proton collision, figure taken from [51]. Due to the composite nature of the proton each event contains, in addition to particles from the hard scattering process, initial- and final- state radiation and particles coming from the underlying event.

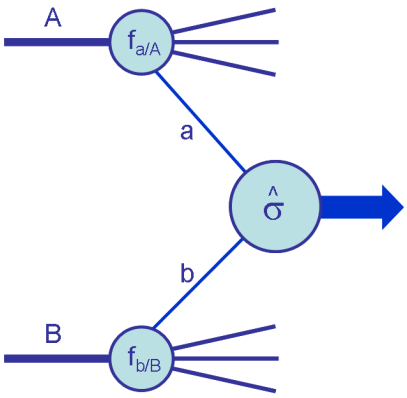

Figure 3.2.: A schematic of the hard scattering process in a proton-proton collision. Figure taken from [52]. $\hat{\sigma}$ denotes the hard scattering cross section of the partons a and b. $f_{\mathrm{a/A}}$ and $f_{\mathrm{b/B}}$ are the parton distribution functions for parton a/b from proton A/B.

of particle i is denoted as k_i. Equation 3.1 also assumes that only two initial state particles exist.

However, when dealing with proton-proton scattering the partons cannot be approximated as free particles. Instead the probability of a parton to carry a specific fraction of the proton momentum has to be evaluated. It is also important to note here that the final state particles can only be calculated to the level of non-composite particles i.e. the level of quarks and leptons.

3.1.2. Parton Distribution Functions

The proton is a bound state the structure of which cannot be calculated from QCD directly since perturbation theory is not applicable. In order to be able to calculate cross sections, however, it is necessary to know the probability of a particular parton, which carries a fraction x of the momentum of the proton, to be available for a scattering process.

The sets of functions providing this information are called Parton Distribution Functions (PDF). They depend on the momentum fraction x, the energy scale Q^2, and the quark/gluon flavour. PDFs cannot be calculated from first principles, however using the DGLAP [1] [53–55] equations it is possible to evolve the PDFs to another energy scale. The DGLAP equations are differential equations derived from scale invariance, which means that in principle they are true to all orders in perturbation theory.

The PDFs themselves are sets of either empirical functions or neural networks that are determined by measurements from deep inelastic scattering (DIS) at a lower energy transfer and then evolved to the energy scale of the LHC [56]. This procedure is far from straightforward, and different groups calculating PDFs observe large discrepancies between their predictions. This is, for example, caused by the use of different data sets for the fit of the PDFs to scattering data, by the choice of the value of the strong coupling constant, or the choice of function to fit to the DIS data. These discrepancies lead to systematic PDF uncertainties, which are evaluated for CMS analyses using the procedure described in reference [57].

The cross sections are calculated using PDFs $f_i(x, Q^2)$ as

$$d\sigma_{k_1 k_2 \to \sum_k p_k} = \int f_{i_1}(x_1, Q^2) f_{i_2}(x_2, Q^2) d\sigma_{k_1 k_2 \to \sum_k p_k}(x_1, x_2) dx_1 dx_2 \ , \qquad (3.2)$$

where $i_{1/2}$ denotes the quark/gluon flavour of the initial state particles, $x_{1/2}$ is the momentum fraction of particle 1/2 and σ is the hard scattering cross section from equation

[1] DGLAP stands for Dokshitzer, Gribow, Lipatow, Altarelli and Parisi.

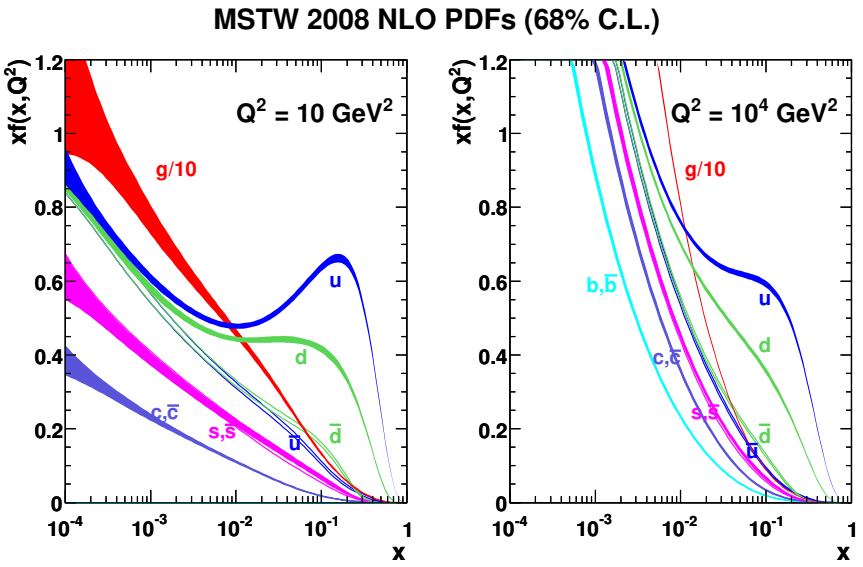

Figure 3.3.: The MSTW (Matin, Stirling, Thorne, Watt) parton distribution functions, taken from [58]. On the left hand side the PDFs are shown at a low energy scale of $Q^2 = 10$ GeV^2. On the right hand side the PDFs are propagated to the higher energy scale of $Q^2 = 10^4$ GeV^2.

(3.1). Figure 3.2 shows a schematic of the use of PDFs during cross section calculations. In Figure 3.3 an example of PDFs for different quark flavours is given.

3.1.3. Parton Showers and Hadronisation

Due to color confinement only colorless particles are measured in the detector. Instead of a single quark or gluon a multitude of different particles are detected in a cone around the initial parton direction. The exact process transforming colored particles into jets cannot be calculated from QCD, although the apperance of new colored particles, i.e. showering, can be modeled using QCD radiation. The hadronisation process, i.e. the merging of particles into one colorless hadrons, can be described by empirical models inspired by QCD.

3.1.4. Underlying Event

In proton-proton collisions there are partons that do not directly take part in the hard process of interest. However these particles still need to be taken into account since their

existence can lead to secondary particles in the detector or even a secondary scattering of final state particles. This contribution to the whole event is called Underlying Event (UE). The UE is modeled in MC generators using phenomenological models with paramters adjusted to data.

3.1.5. Pileup

If there were only one proton per bunch, the chance of ever measuring an interaction would be practically zero. At the LHC one bunch contains of the order of 10^{11} protons. This leads to multiple proton-proton interactions during one bunch crossing thus particles from secondary interactions are also measured in the detector. This additional noise source is called pileup. Pileup leads to tracks and energy deposits in the detector that do not come from the primary event and can therefore distort the measurement. Two different kinds of pileup can be distinguished. The first is in-time pileup, which comes from scattering processes happening at the same bunch-crossing as the primary process. The second is out-of-time pileup. These are events from a different bunch crossing that get associated with the primary event due to the finite detector temporal resolution and its finite response time.

3.2. Reconstruction of Measured Events

After an event is measured the output from the various subdetectors has to be combined in order to reconstruct physical objects. The reconstruction also has to deal with pileup and detector noise. In this section some techniques used by CMS on subdetector level are discussed in sections 3.2.1-3.2.3. These techniques will later be combined for the reconstruction of actual physical particles such as electrons or muons (section 3.2.4-3.2.7). For this task the CMS experiment uses the particle flow algorithm (PF), for a detailed description, see reference [59–61].

3.2.1. Particle Tracks

The basic problem of reconstructing particle trajectories from tracker hits is of high combinatorical complexity. The algorithm used for this reconstruction is called Combinatorial Track Finder (CTF) [62]. The CTF uses a sequential procedure, removing the tracks with high p_{T} and many associated hits, which are easiest to reconstruct, from the tracker hits, and then resuming the reconstruction process. The track reconstruction is started from seeds which are in the first iteration required to consist of at least 3 hits in the innermost layers of the pixel detector. The algorithm then uses Kalman filters [63–65]

to extrapolate the trajectory through the detector layers. This iterative method uses all the tracker hits from lower layers to extrapolate to a region in which the next hit is estimated, taking into account energy loss due to the tracker material and effects from coulomb scattering. This iteration is stopped either when the particle leaves the tracker, or when the p_{T} of the reconstructed particle sinks below a threshold value.

In order to cope with the high energy losses due to bremsstrahlung of electrons a different algorithm is used to reconstruct electron tracks (see section 3.2.4).

3.2.2. Vertices

The reconstructed interaction points are called vertices. For the HLT a quick vertex reconstruction using only hits in the pixel tracker is used. The primary event vertex is considered to be the one with the highest transverse momentum tracks associated to it. This is calculated as the sum over the p_{T} of all associated tracks, weighted with a goodness of fit value for each track. The reconstruction of vertices allows for a removal of all objects that are associated with a secondary vertex, from an event. This is used for pileup removal at CMS. The adaptive vertex reconstruction algorithm [66] is used for a more differentiated three dimensional reconstruction of event vertices. It is an iterative procedure that sorts through all reconstructed tracks and finds those which share a common origin. The vertex reconstruction at CMS reaches a resolution of about 30 µm.

3.2.3. Clustering of Energy Deposits

In each of the calorimeters energy deposits are clustered separately [67]. First local maxima are identified as calorimeter cells with a local maximum of energy. Then adjoining cells with energy deposits above a given threshold are clustered into particle flow clusters. The threshold is defined as the detector noise level plus approxately 2σ, where σ is the energy resolution. These particle flow clusters are later used in the reconstruction of various physics objects, starting with the reconstruction of charged hadrons, leptons and neutral hadrons and photons.

3.2.4. Long-Lived Leptons

Muons

Muon reconstruction uses tracks in the CMS tracker in combination with hits in the muon system. If a muon is reconstructed with a sufficient amount of hits in both systems it is called a global muon. Most muons with a sufficiently high transverse momentum can be reconstructed using hits in the muon system, extrapolating them to tracks in the inner tracker. Muons reconstructed in such a way are used to reduce the tracks the particle flow algorithm has to match to energy deposits. If the number of hits in the muon system is insufficient to find the matching tracks, the matching is done by extrapolating the tracks found in the main tracker and matching them to the hits in the muon chambers. Muons reconstructed this way are called tracker muons. If only hits in the muon chambers are available for reconstruction the reconstructed muon candidate is called standalone muon. In this thesis global muons are used in the reconstruction.

Electrons

Electrons are reconstructed from tracks and energy deposits in the ECAL. However, since electrons lose much more energy due to bremsstrahlung in the tracker than other charged particles, a special track reconstruction [68] as well a specialized approach of clustering the energy deposits [69] are needed. As a starting point for the reconstruction of electrons energy deposits in the ECAL which exhibit a spread in ϕ, as is expected due to bremsstrahlung emissions along the electron trajectories, are clustered together as Super Clusters (SC). Using the SCs as seeds the electron tracks are reconstructed using the Gaussian Sum-Filter [70] algorithm. This method is sufficient to reconstruct most electrons with p_{T} larger than 5 GeV. The rest of the electrons are reconstructed by recalculating tracks with either too few hits or too large a χ^2 fit value with the Gaussian Sum-Filter algorithm.

3.2.5. Charged Hadrons

Charged hadrons are pieced together by the particle flow algorithm, combining tracks and energy deposits inside the hadron calorimeter. Tracks associated with hits in the muon chambers are not considered in this reconstruction step in order to not falsely reconstruct a muon as a charged hadron. In order to remove pileup each hadron that does not originate from the primary vertex is removed from the event; this is called charged hadron subtraction. If the energy deposit in the calorimeter exceeds the one

expected from track reconstruction an additional neutral hadron or photon has to be assumed, based on the calorimeter in which the bulk of energy was deposited.

3.2.6. Photons and neutral Hadrons

When all tracks are associated with energy deposits in the calorimeters, the remaining deposits above detection threshold are considered to be either photons or neutral hadrons, depending on wether the bulk of the energy was deposited in the ECAL or HCAL. For these neutral particles only the calorimeters can be used to reconstruct ϕ, η and the transverse momentum, resulting in a larger uncertainty in the angular variables for neutral hadrons.

3.2.7. Jets

Due to quark confinement, instead of a single quark a jet of particles in a cone around the original radiation angle is detected, see for example [71, 72]. In order to identify QCD objects the individual reconstructed physics objects like hadrons or photons have to be reliably clustered into jets. Such jet clustering algorithms have to be infrared safe, i.e. be robust against the radiation of low energy particles, and collinear safe, i.e. a collinear splitting of their constituents should lead to the same jet properties. The algorithm is also required to be compatible with pileup removal. Two different types of algorithms exist, cone-type algorithms like Iterative Cone or SisCone [73], and sequential clustering algorithms like the Cambridge-Aachen (CA) algorithm [74, 75] and anti-k_T [76, 77] algorithm.

However, in this thesis only the anti-k_T algorithm will be discussed in more detail, since it is the only one used in the following analysis.

The anti-k_T algorithm starts with a physics object i, and combines it with the nearest object j into one pseudo-jet. The next step combines the pseudo-jet object with its nearest particle. This procedure is repeated until the distance of the pseudo-jet to the nearest particle is greater than the distance to the beam d_{iB}. Here distance d_{ij} between two pseudo-jet objects is defined as

$$d_{ij} = \min(k_{T,i}^{-2} k_{T,j}^{-2}) \frac{\Delta_{ij}^2}{R^2} \ , \tag{3.3}$$

$$\Delta_{ij}^2 = ((y_i - y_j)^2 + (\phi_i - \phi_j)^2) \ , \tag{3.4}$$

$$d_{iB} = k_{Ti}^{-2} \ , \tag{3.5}$$

where R is a radius parameter (0.4 or 0.8 for this analysis), and k_{Ti} is the transverse momentum of object i. This clustering per definition is collinear- and infrared safe. In

this thesis fat jets, i.e. jets with a large radius parameter are used in order to take the highly boosted topology from high-p_{T} vector boson decays into account. Jets with a large radius parameter for the clustering are called fat jets. The mass of a jet is defined as the invariant mass of all particles clustered into its cone.

After the jets are clustered and therefore available for reconstruction some corrections have to be applied in order to map the measured jet energy to its physical value, the energy of the parton from which the jet emerged. This is necessary mostly because of nonlinearities in the detector, which have to be corrected after the measurement is taken, as well as discrepancies between Monte Carlo simulated samples and data. The corrections applied in this analysis follow the recipe of recommended jet energy corrections provided by the CMS jet energy corrections subgroup [78]. The corrections are applied sequentially in the order indicated by the numbering as η and p_{T} dependent scale factors on the jet four-momentum. L2L3 residual corrections are only applied to data, while the rest of the corrections is applied to both MC and data.

- **L1**
  The main goal of the L1 corrections [79] is to reduce pileup. This is particularly necessary since pileup from neutral particles cannot be removed by the reconstruction of primary vertices. To remove this pileup contribution the average energy deposit per unit-area of the detector is subtracted from the jet energy.

- **L2L3**
  Scale factors dependent on jet η and p_{T} and applied to correct detector efficiencies to that the jet response is independent of the η range. They also contain scale factors, based on Monte Carlo truth to correct for contributions from missing energy.

- **L2L3 Residual**
  These corrections are applied to data only, in order to further correct the L2L3 corrections for discrepancies between data and Monte Carlo.

Since this analysis depends on a good separation of QCD jets and jets coming from a boosted vector boson decays, the jet pruning algorithm [80] is, for example, used to further reduce soft wide-angle QCD radiation coming from pileup events or initial state radiation, and to improve the mass resolution and reduce systematic effects of the jet clustering algorithms. For this the constituents of the anti-k_T jets are reclustered discarding soft components. A component is regarded as soft if either $\min(p_{Ti}, p_{T,j})/p_{Tij} < 0.1$, i.e. if the transverse momentum of one of the constituents is too small compared to the combined momentum, or if $\Delta R_{ij} > m_{orig}/p_{T,orig}$, i.e. the angular separation between the constituents is larger than the ratio of original jet mass and p_{T}. The mass of such a pruned jet is called pruned jet mass m_{jet}^{pruned}.

3.2.8. Jet Substructure Techniques

In order to further reduce background from QCD events, techniques depending on the substructure of jets are used.

B-tagging

The procedure to classify jets according to their probability of originating from a bottom quark is called b-tagging. The technique uses the relatively long lifetime of B-mesons. This long lifetime comes from the suppression of a decay to up- and charm-quarks, due to the small CKM matrix element. The decay to the top quark is suppressed as well because the top quark is much heavier than a B meson. This results in a displaced secondary vertex of the jet, which can be resolved by the tracker if the distance between primary and secondary vertex is large enough. In the analysis described here the Combined Secondary Vertex (CSV) algorithm ([66,81]) is used to further suppress background from top quark pair production ($t\bar{t}$) or single top events. The CSV algorithm combines information about track parameters and secondary vertices of the jets into a likelihood discriminant. Thus providing a method to discriminate jets coming from a b-quark, from those originating from light quarks, gluons, or charm-quarks. There are different working points (WP) for the CSV algorithm, which are defined as the values of the b-tagging discriminant that achieve a certain mistag rate. If a jet coming from light quarks is misidentified as a b-jet, the jet is considered to be *mistaged*.

In this analysis all anti-k_T jets are considered to be from B-meson decays if their b-tagging value is larger than the CSV medium working point [81], which has a misidentification probability of about 1.5 %. In figure 3.4 a schematic of a jet with a secondary vertex is shown.

N-Subjettiness

In order to further discriminate between jets from SM background and jets coming from a boosted vector boson decay, a quantity called n-subjettiness [83] is used. For this the jet is reclustered into N subjets using the anti-k_T algorithm. The n-subjettiness is then defined as

$$\tau_n = \frac{1}{d_0} \sum_k (p_{T,k} \min(\Delta R_{k1} \Delta R_{k2} \dots \Delta R_{kN})) \ , \tag{3.6}$$

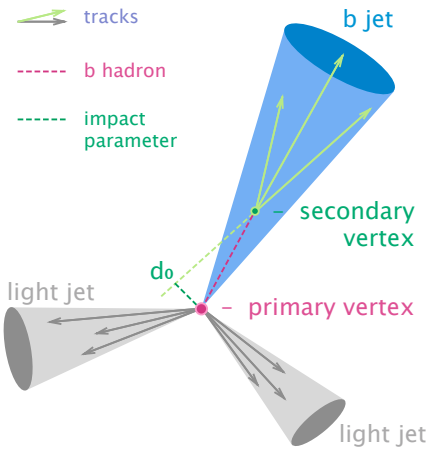

Figure 3.4.: An illustration of the principle of the CSV algorithm. The blue jet has a displaced secondary vertex coming from the decay of a B-meson. The tracks coming from the B-meson do not point to the primary vertex but rather are displaced by an impact paramter d_0. The displaced tracks can be used to reconstruct the secondary vertex at a distance from the primary event vertex. Figure taken from [82].

The index k runs over all particles in the original jet, $d_0 = \sum_k p_{T,k} R_0$ and R_{ki} is the distance of particle k to the candidate subjet i. The quantity 2-1-subjettiness

$$\tau_{21} = \frac{\tau_2}{\tau_1} \tag{3.7}$$

is used to identify jets clustered from two subjets. Jets coming from a W/Z decay are characterized by lower values of τ_{21} compared to the SM background [84, 85]. Figure 3.5 shows a schematic of the difference between a fat QCD jet and one coming from a boosted W decay. The use of the τ_{21} ratio to discriminate between QCD jets and jets coming from a boosted vector boson decay, is called *V-tagging*.

3.2.9. Missing Transverse Energy

The missing transverse energy (MET) is calculated after all other objects are reconstructed as

$$E_T^{miss} = -\sum_k p_{T,k} \ , \tag{3.8}$$

where $p_{T,k}$ is the transverse momentum of the kth particle and the sum goes over all reconstructed PF objects originating from the primary vertex [86]. Since the two protons that take part in the scattering have approximately zero momentum in transverse

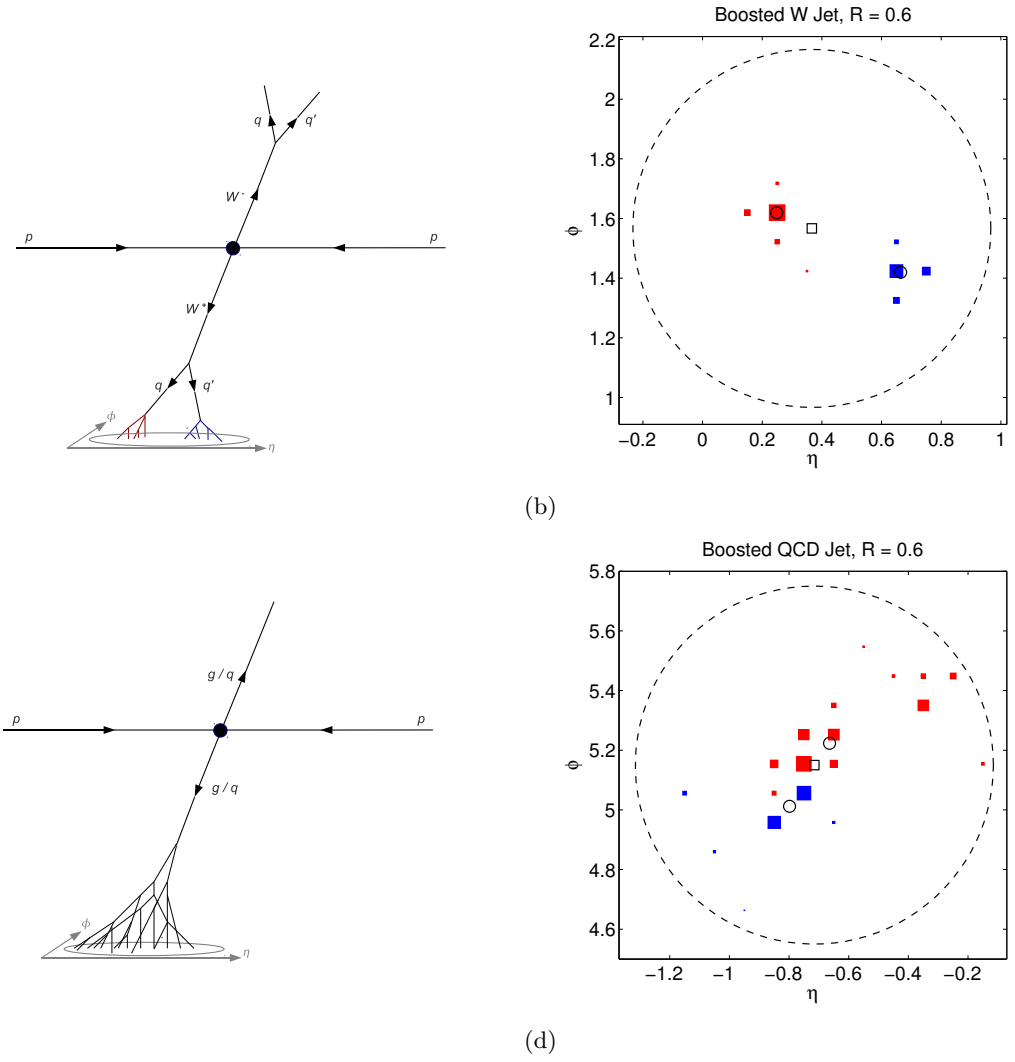

Figure 3.5.: Figure (a) shows an event with boosted W^+ W^-production. Figure (b) shows the typical substructure of a fat jet coming from such an events; as is illustrated two distinct subjets can be distinguished. Figure (c) shows a typical QCD dijet event and (d) the corresponding event display. All jets were clustered using the anti-k_T algorithm. Figure taken from [83].

direction, the sum over all transverse momenta from scattered particles should also be zero. The small momentum of the partons in transversal direction is considered to be negligible. If an event has MET not equal to zero, this can arise from particles that are lost in the beam-pipe, in non-active detector material or from detection inefficiencies. But MET can also originate from neutrinos or other particles which are very unlikely to interact with the detector, such as a potential dark matter candidates.

3.3. Generation of Monte Carlo Events

In order to find new physics detailed predictions of standard model and BSM processes have to be made of both the inclusive and differential cross sections. For these predictions various Monte Carlo event generators can be used. These generators tackle the highly non-trivial problem of event simulation utilizing the idea of scale factorization, i.e. the idea that the process in question can be divided into subprocesses according to their energy scales. The first step is the calculation of the matrix element of the hard process, which takes place on a high momentum scale where pertubative calculations are valid even for QCD processes. The next step is all order soft and collinear QCD radiation, the so-called showering. Afterwards phenomenological models for hadronisation are used. However, for a prediction that can be used for comparisons to experimental data, the simulation must also include the decay of unstable hadrons, deal with the underlying event, and undergo a full detector simulation. This process also deals with the proton-structure using PDFs and includes the modelling of soft initial- and final- state radiation. A schematic of these processes is shown in figure 3.6. MonteCarlo methods are used to deal with the large multi-dimensional phase space of final state particles.

The following chapter is based on [87–89].

3.3.1. Matrix Element Calculation

Most event generators allow the user to chose a process, the matrix element of which is calculated to leading order (LO) or next to leading order (NLO) in perturbation theory. Since many processes that are interesting in the search for new physics are extremely rare the event generator produces only events for the chosen process, using MC methods for integration to deal with the phase space of the final state particles. In this calculation two main sources of uncertainty are present. One is that the matrix element is only calculated to some order in perturbation theory, since in each order the number of Feynman graphs to be calculated rises, and therefore computation time rises. The second source of uncertainty is the difficult proton-structure, which makes the use of PDFs for the calculations necessary. Some additional ambiguities are introduced due to the choice

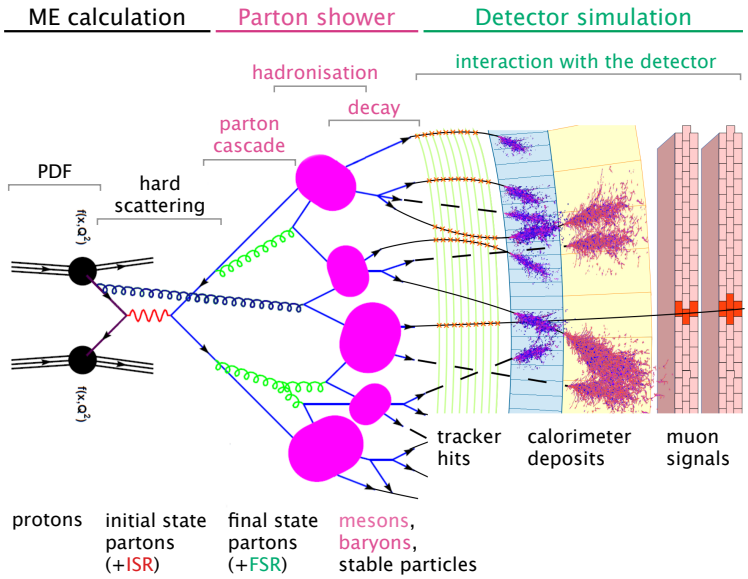

Figure 3.6.: A schematic view of the stages of MC event generation. Figure taken from [90].

of the renormalisation scale.

3.3.2. Showering and Hadronisation in Simulation

Showering describes the scale evolution from the high momentum scales where the scattering takes place to a scale of about 1 GeV, where colored particles begin to be confined inside of hadrons. Showering itself, which describes the initial- and final- state QCD radiation, is process-independent, i.e. factorizes from the process cross section in the collinear and soft limit and only depends on the radiation energy with respect to the parton and angle of emission. Leading collinear logarithmic parton shower algorithms are used to calculate the collinear emission of QCD particles. The algorithms work iterativly, where the next final state, formed by two collinear partons, is only kept for the next iteration if their distance is larger than a resolution-based minimal separation. Most shower-generators also include soft wide-angle radiation. The challenge of initial-state radiation is addressed by backwards evolution of an initial state parton to higher momentum fractions using the DGLAP equations. Since parton shower algorithms usually only describe collinear and soft scattering, the calculation of next-to-leading-order matrix elements is needed whenever the process in question strongly depends on multijet final states. When using matrix element calculation to NLO double counting has to be avoided [87]. This refers to the fact that with NLO matrix element calculations,

each emission can arise from two different paths, once from the ME calculation and once from the showering algorithm. The procedure used to avoid this double counting of components is called matching [91].

The hadronisation process cannot be derived from QCD but is instead described through phenomenological models like the Lund-string model or cluster models. In the lund-string model [92–94] a set of colored particles is connected via a linear confinement potential at low energies. As soon as the potential energy stored in this "string" becomes large enough a quark-anti-quark pair is created. This process continues until all colored particles are in sufficient proximity to other color charges, thus forming hadrons. In cluster models [95,96] the notion of preconfinement, i.e. the color structure arising from showering algorithms, as well as gluon splitting are used to cluster shower constituents into colorless objects.

In order to simulate the whole event as it would occur for example at the LHC, the decay of unstable hadrons has to be simulated after the hadronisation step. In addition MC generators also simulate the underlying event by allowing the possibility of multi-particle interactions which can lead to additional soft jets in the event. The effects of the underlying event on the hard process due to color screening or rescattering are not known well [97] and therefore not addressed by most MC generators.

3.3.3. Detector Simulation

After all physical objects like leptons and hadrons are simulated on generator level, the events have to undergo a full detector simulation before they can be compared to data. The CMS detector is simulated using the Geant4 software [98,99]. This software package simulates the interactions of the collision particles with matter, including effects like ionization, bremsstrahlung losses, multiple scattering and hadronic and electromagnetic showering.

3.3.4. Monte Carlo Generators

There are many MC-event generators which are distinct in their implementation and their usage. Some generators such as MadGraph and Powheg are only able to do matrix element calculations; their output is in the Les Houches (LHE) event format in order to be easily usable by parton shower generators such as Pythia. General purpose event generators are able to do the full simulation including showering and hadronisation.

MadGraph
The MadGraph [100] package is able to calculate leading order matrix elements for SM processes, but is also able of doing matrix element calculations for exotic models

with additional packages. In this thesis the RS MODEL [101, 102] is used to simulate the production of a Spin-2 resonance. The package TAUDECAY [103] is used to simulate leptonic τ decays. MADGRAPH is capable of simulating the phase space including PDFs and adding initial- and final- state radiation. Using MADEVENT it is also possible to calculate leading order cross sections for the given process.

POWHEG
The event generator POWHEG [104] provides next to leading order accuracy in QCD. POWHEG calculates the hardest radiations with NLO accuracy while soft radiation is calculated to leading order. It can therefore be interfaced with any shower generator that is either p_{T} ordered or is capable of including a p_{T} veto.

PYTHIA
Although PYTHIA [105] is a general purpose event generator, it is often used as a shower generator, that is interfaced to other generators that allow NLO calculations. PYTHIA includes the calculation of the underlying event, and offers different models for hadronisation for example the Lund string model.

TAUOLA
As a last step the decays of τ-leptons are simulated using the TAUOLA [106] package.

4. Statistical Methods

In this chapter the main statistical methods and tools used to interpret data in this thesis are discussed. First, a brief description of the merits and pitfalls of hypothesis testing is given. In the second part the CLs technique [107] for limit setting in its complete and asymptotic form is discussed. The handling of systematic uncertainties as nuisance parameters and the handling of shape parameters within this framework is described. These methods are implemented in various statistics tools for particle physics such as the Combine framework, which is used to calculate limits in this thesis. The following sections are based on references [108], [109] and [110].

4.1. Maximum Likelihood Estimation

The goal of maximum likelihood parameter estimation is to find values for the parameters θ for a given probability distribution function $f(x, \theta)$ that maximize the probability of measuring a given sample $\{x_i\}$. θ is a set of parameters that parametrise the probability density function f. First the joint density function F

$$F = \prod_{i=1}^{n} f(x_i, \theta) \ , \tag{4.1}$$

is defined. If we take F to be a function of the parameters θ instead of the set of observed values $\{x_i\}$ the resulting function is called the likelihood l. For many purposes it makes sense to look at the logarithmic likelihood

$$L = \ln(l) \ , \tag{4.2}$$

because its derivatives are easier to compute than for the likelihood function. The best values for the parameters θ in a maximum likelihood estimation are the values that maximize the likelihood function or equivalently the logarithmic likelihood function.

4.2. Hypothesis tests

The idea behind hypothesis tests is to have a reproducible and understandable measure of whether a given model actually fits the data, which is subject to statistical errors. For this approach a null hypothesis H_0 has to be formulated; for example, the null hypothesis could be that the measured data follows a given probability density function. In order to test whether or not the null hypothesis should be rejected, a test statistic V is defined. V is a quantity that is expected to have different distributions for alternative hypotheses compared to its distribution $f(V)$ under the null hypothesis. In order to have a consistent way of rejecting H_0 a level of significance α has to be agreed on beforehand. This level of significance is then compared to the p-value

$$p = \int_{V_0}^{\infty} f(V)dV \ , \tag{4.3}$$

where V_0 is the observed value of the test statistic. The p-value quantifies the probability, under the assumption that H_0 is true, to see a variation between the prediction under H_0 and data as large as observed or larger. The null hypothesis gets rejected if the calculated p-value is smaller than the chosen level of significance α. The significance parametrises errors of the first kind; this means that in α percent of cases H_0 is rejected although it is true. It is important to note that this approach only deals with errors of the first kind and not with errors of the second kind. The latter are defined as the probability of accepting H_0 although it is false. The p-value therefore does not measure the probability of H_0 being true, but quantifies the level of significance with which the data differs from the distribution given by the null hypothesis.

χ^2 Tests:

As test statistic many quantities can be chosen; in this thesis χ^2 is used. χ^2 is the quadratic difference of expected events N_{0k} to observed events N_k per bin k

$$\chi^2 = \sum_k \frac{(N_k - N_{0k})^2}{N_{0k}} \ . \tag{4.4}$$

The χ^2 variable is normalised with the variance of the probability function under the null hypothesis, in this case Poission distributed values are assumed; thus the variance is equal to N_{0k}. The sum goes over all bins. A test using this quantity as test statistic is called a χ^2 test. The expectation value of χ^2 per construction is

$$< \chi^2 > = n_{d.o.f} \ , \tag{4.5}$$

where $n_{d.o.f}$ is the number of degrees of freedom. The quantity $n_{d.o.f}$ can be calculated as

$$n_{d.o.f} = (n_k - 1 - n_f) \ , \tag{4.6}$$

where n_k is the number of bins and n_f is the number of parameters of the probability distribution function for H_0 that are fixed by data. For large values of $n_{d.o.f}$ the χ^2 distribution can be approximated by a Gaussian function with $x_0 = n_{d.o.f}$ and $\sigma = \sqrt{2n_{d.o.f}}$, which greatly simplifies the calculation of the p-value. The χ^2 test assumes that the disagreement per bin of the measured values follows a Gaussian distribution, which is only a good approximation if the number of expected events per bin is sufficiently large, see for example reference [108].

4.3. CLs Limits

The goal of any particle physics analysis searching for new physics is to either find new phenomena or to give exclusion limits on BSM phenomena. For this a quantitative approach is needed in order to evaluate the probability that the observed phenomenon cannot be described with background only, in case of a discovery, or that the observed data does not exclude exotic phenomena smaller than a given maximum signal strength, in case of exclusion.

As is the case for any hypothesis test, the null hypothesis, which is in this case denoted with the subscript b for background only, has to be separated from the signal-plus-background $s + b$ hypothesis. When setting exclusion limits, a mere separation of the two scenarios is not sufficient. Instead the value μ should be found with which the signal needs to be scaled in order to reject $\mu \cdot s + b$ with a given confidence level of $1 - \alpha$. One of the challenges in this scenario is to define the test statistic in a way that includes uncertainties on the background and signal modelling. Another challenge is to define a quantity similar to the p-value, that accounts for the problem of sensitivity. If normal p-values, as defined in section 4.2, would be used it were possible that the chosen test statistic had similar values for the case of background and signal-plus-background hypotheses. In such a case the analysis is said to have a low sensitivity. In those cases where it is hard to distinguish between the signal-plus-background and background hypothesis, no statements about the validity of the signal hypothesis should be made. Therefore a quantity called CLs is defined such that if the signal hypothesis is rejected when CLs $< \alpha$, it will only be rejected if the description using the signal-plus-background hypothesis leads to small p-values, while the background only hypothesis leads to a good description of the data. In case of low sensitivity when the p-values for both hypothesis are similar, the signal-plus-background hypothesis cannot be rejected in favour of the null hypothesis. The CLs quantity is defined as

$$\mathrm{CL_s} = \frac{P(Q \geq Q_{obs}|s+b)}{P(Q \geq Q_{obs}|b)} \coloneqq \frac{p_{s+b}}{1-p_b} \ . \tag{4.7}$$

Here Q is the test statistic and Q_{obs} is its observed value.

$$\mathrm{CL_\mu} = \frac{P(Q \geq Q_{obs}|\mu \cdot s + b)}{P(Q \geq Q_{obs}|b)} := \frac{p_\mu}{1 - p_b} \tag{4.8}$$

is defined in order to give a maximum value of the signal scale μ for which the signal-plus-background hypothesis can be rejected with the given confidence limit. This is done by calculating a μ such that $\mathrm{CL_\mu} = \alpha$. It remains to define the test statistic in a meaningful way that also allows to deal with systematic uncertainties on the background and signal estimation. For limit calculations this can be done using the profile likelihood ratio which gives the maximum separation power of background hypothesis and signal hypothesis in case of no nuisance parameters, according to the Neyman–Pearson lemma, see for example reference [110]. If the nuisance parameters are well constraint, the Neyman-Pearson lemma remains approximately true. The profile likelihood ratio is

$$\lambda(\mu) = \frac{L_p(\mu)}{L(\hat{\mu}, \hat{\theta})} \ , \tag{4.9}$$

where θ denotes the so-called nuisance parameters, $L_p(\mu)$ is the profile likelihood function, i.e. the likelihood with all nuisance parameters set to values that maximize the likelihood for this particular μ. $L(\hat{\mu}, \hat{\theta})$ is the likelihood function where $\hat{\theta}$ and $\hat{\mu}$ denote the values that maximize the profile likelihood function L. The test statistic Q_μ for setting upper limits is then defined as

$$Q_\mu = \begin{cases} -2\ln(\lambda(\mu)) & , \hat{\mu} \leq \mu \\ 0 & , \hat{\mu} > \mu \end{cases} \ . \tag{4.10}$$

The reason for setting Q_μ to zero for values smaller than $\hat{\mu}$ is that when the goal is to set an upper limit, samples with data where $\hat{\mu} > \mu$ do not represent less compatibility with μ than the data obtained. Therefore these cases are removed from the rejection region of the text. If the goal is to define a test statistic for discovery, a different definition for the test statistic should be used see for example reference [110]. The p-value is

$$p_\mu = \int_{Q_{obs}}^{\infty} f(Q_\mu|\mu) dQ_\mu \ , \tag{4.11}$$

where $f(Q_\mu|\mu)$ denotes the distribution of the test statistic under the assumption of a signal hypothesis corresponding to $\mu \cdot s + b$.

There are two different approaches of dealing with nuisance parameters to account for systematic uncertainties in the modelling of signal and backgrounds. In the frequentist approach the nuisance parameters are fixed to the values that maximize the likelihood function for given signal hypothesis of $\mu \cdot s + b$. The nuisance parameter are fitted within the contraints of a Gaussian prior distribution given by the assigned uncertainties.

The resulting likelihood function $L_p(\mu)$ is called profiled likelihood. In a Bayesian-like approach the nuisance parameters are handled by constructing the marginal likelihood

$$L_m(\mu) = \int d\theta L(\mu, \theta)\pi(\theta) \ . \tag{4.12}$$

The function $\pi(\theta)$ is called a prior probability density function and describes the probability distribution of the nuisance parameters θ.

When calculating the full CLs limit the distribution of the test statistic, which is important for the calculation of the p-value, is determined by generating pseudo-experiments samples for profiled values of the nuisance parameters and a given μ, or using the marginal likelihood, which is evaluated using MC integration. These toy-data sets are generated using MC methods and assuming a Poisson distribution of data. This results in a high number of pseudo-experiments samples that need to be generated for this kind of calculation. The expected $(1-\alpha)$-CLs limit is then defined as the median of solutions to $\mathrm{CL}_{\mu'} = \alpha$ using MC data sets according to the background-only hypothesis. The expected 1 and 2σ error bands are defined as the values of μ that mark the intervalls containing 68% and 95% of the μ distribution around μ'. Here σ denotes the standard deviation of a normal distribution. To calculate the observed limits, the profile or marginal likelihood functions are estimated with respect to data.

4.3.1. Asymptotic CLs Method

The asymptotic CLs method is an approximation of the full CLs limit that allows to skip the generation of most of the necessary pseudo-experiments. This method is described in detail in reference [110]. It relies on the asymptotic behaviour of the profile likelihood ratio used as test statistic (see reference [111]) of

$$-2\ln(\lambda(\mu)) = \frac{(\mu-\mu')^2}{\sigma^2} + O(1/\sqrt{N}) \ , \tag{4.13}$$

in the limit of a large sample $N \to \infty$. The standard deviation σ and mean μ' are then estimated using the covariance matrix of the estimators for all nuisance parameters. These quantities are calculated using a special artificial data set called "Asimov Data Set", which is defined as the data set that has the profiled estimators for all parameters equal to the true values or, equivalently, the values of all quantities in the Asimov data set are equal to their expectation values. This method significantly reduces the computational effort. However, although the method often produces limits similar to the computational expensive method even for small sample sizes, it is strictly mathematically valid only in the limit of large sample sizes and has to be used with some caution.

4.3.2. Shape Parameters

Many physics analyses use the shapes of distributions in order to distinguish between signal and background processes. This introduces additional systematic uncertainties that do not have a direct influence on the event yields, but rather on the overall shapes of the distributions. Uncertainties like these can also be addressed in the limit setting procedure by including these uncertainties as nuisance parameters. This analysis uses the Combine framework [112] to calculate all limits; this means that the signal and background shape models are used to calculate the expected number of events to compare to data. In principle the uncertainties on shape parameters are included as nuisance parameter with a unit Gaussian prior distribution. When analytical functions are used for the prediction of yield and shape, this approach is called unbinned shape analysis. It is used in this thesis for the description of both background and signal functions. If an unbinned likelihood is used in combination with this approach, the evaluation of the analytical modelling is straightforward. In the case of a binned likelihood used together with analytical functions for the shape modelling attention has to be paid to the coarseness of data-binning, because of the way Combine evaluates the event prediction from analytic functions. Since Combine uses the analytic shape function evaluated at the center of the bin for each data point, this can lead to a systematic under- or overestimation of data if the binning in the dataset is too coarse. In such cases a binned shape analysis should be used, which requires a histogram instead of an analytic function, with the bin widths corresponding to the binning used in data.

5. Search for Massive Resonances Decaying into Pairs of Boosted Vector Bosons in the Semileptonic and All-Hadronic Final State with the CMS Detector

5.1. Introduction

The work presented in this thesis is an expansion of two existing CMS analyses, which are described in this chapter. Both analyses are searches for a diboson resonance, however, they differ in the final state. The first final state is VV decaying to two fat jets, i.e. jets with a large clustering parameter R of 0.8, where VV denotes WW or ZZ. This final state is denoted as all-hadronic channel in the following. The second final state is WW or WZ decaying to one fat jet and a lepton plus neutrino, which is called semileptonic channel. The resonance searches differ also in their background estimation techniques and in the limit setting procedure. The analyses are based on data taken at $\sqrt{s} = 13$ TeV in proton-proton collisions with the CMS detector, at an integrated luminositiy of 2.1 fb^{-1} (2.6 fb^{-1}) and use jet substructure techniques to reconstruct diboson events in a highly boosted regime, in order to search for a resonance in the reconstructed mass spectrum. In the following sections the important aspects of the CMS analyses for this thesis are discussed. For a more detailed description of the semileptonic analysis see reference [113] and for a description of the all-hadronic analysis see reference [114]. Section 5.2 contains a description of the topologies of expected signal events as well as of the main background of the analysis. In section 5.3 the reconstruction of physics objects such as leptons or the vector bosons is described. Section 5.3 contains the selection cuts used for the final event reconstruction, and section 5.5 contains the estimation and modelling of dominant backgrounds. The last section, 5.6, is dedicated to the systematic uncertainties used for the final limit setting.

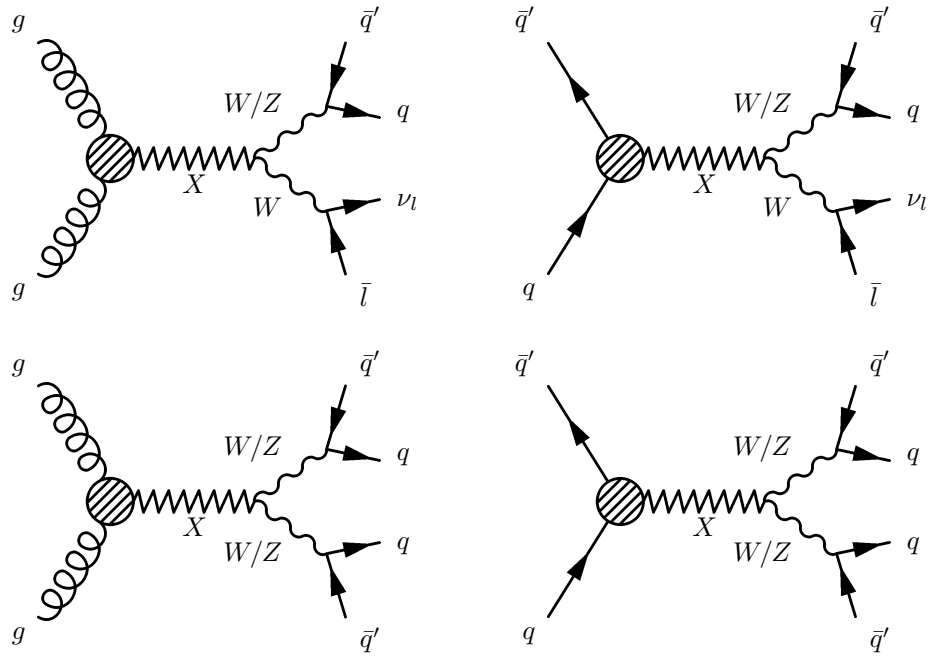

Figure 5.1.: The Feynman graphs for the considered signal processes. At the top is the production of a heavy resonance through gluon fusion (left) and Drell-Yan (right) in the semileptonic decay channel. On the bottom are the same production mechanisms for the all-hadronic channel. The circle stands in for the coupling of the exotic resonance to gluons or quarks.

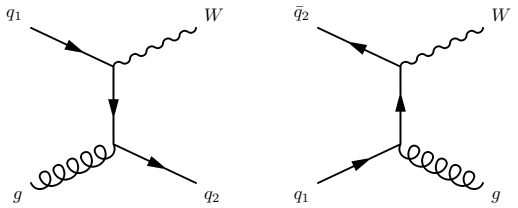

Figure 5.2.: Representative Feynman graphs for W+jets processes. In the semileptonic decay channel W+jets is the dominant background.

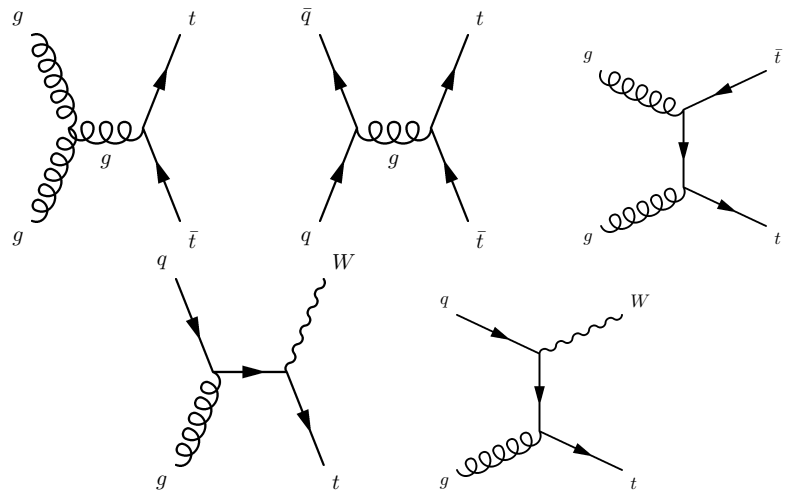

Figure 5.3.: The figure displays the most important Feynman diagrams for $t\bar{t}$ and single top processes. These processes are subdominant backgrounds in the semileptonic case.

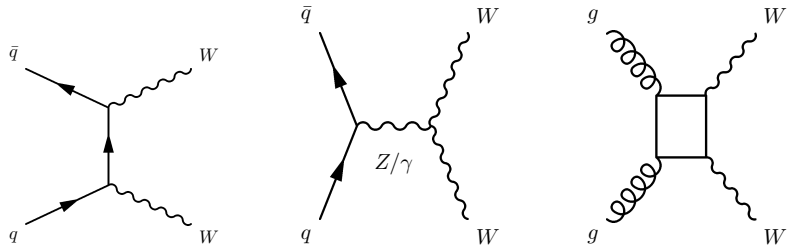

Figure 5.4.: The leading Feynman graphs for SM processes that produce two W bosons in the final state. These diagrams contribute to the backgrounds for diboson resonance searches.

5.2. Event Topology

The standard model of particle physics does not predict any resonant behaviour in the reconstructed diboson mass spectrum. In this mass spectrum the background of standard model processes is expected to have a more or less exponential decay. Many theory models for example models predicting warped extra dimensions (see chapter 1) do predict heavy exotic particles decaying into two highly boosted vector bosons. The Feynman graphs for such processes can be seen in figure 5.1. The vector bosons in turn decay before detection into the final state particles of the event. This thesis covers both the semileptonic and all-hadronic final states. The semileptonic final state includes the decay of W bosons to τ as long as the τ decay leptonically. The signal region of the analyses is defined as the intervall in the m_{VV} spectrum between 800 and 4500 GeV in the semileptonic case, or between 1200 and 4000 GeV in the all-hadronic case.

5.2.1. Signal Processes

The main analysis is optimised and carried out for three different theory models, HVT model B as well as a Bulk-Graviton model. Both analyses use the narrow width approximation for the modelling of the signal shapes. The resonance is assumed to have and intrinsic width smaller than the full-width-half-maximum (FWHM) of the detector resolution. In this approximation the signal shape modelled by a function describing the detector resolution. In the semileptonic case a double sided Crystal-Ball function see 5.1, i.e. two power-law-functions modelling the tails around a Gaussian core, is used to model the detector resolution.

$$\mathrm{DCB} = \begin{cases} e^{\frac{x-\bar{x}}{\sigma 2}^2} & \text{for} \quad -\alpha_1 < \frac{x-\bar{x}}{\sigma} < \alpha_2 \\ \frac{n_1}{|\alpha_1|}^{n_1} \cdot e^{-\alpha_1^2/2} \cdot \left(\frac{n_1}{|\alpha_1|} - |\alpha_1| - \frac{x-\bar{x}}{\sigma} \right)^{-n_1} & \text{for} \quad \frac{x-\bar{x}}{\sigma} < -\alpha_1 \\ \frac{n_2}{|\alpha_2|}^{n_2} \cdot e^{-\alpha_2^2/2} \cdot \left(\frac{n_2}{|\alpha_2|} - |\alpha_2| - \frac{x-\bar{x}}{\sigma} \right)^{-n_2} & \text{for} \quad \frac{x-\bar{x}}{\sigma} > \alpha_2 \end{cases} \tag{5.1}$$

The parameters $n_1,\ n_2$ are the free parameters of the two power-law tail functions, while σ and $\bar{x}$ are the normal deviation and mean of the gaussian core function.

In the all-hadronic case the sum of a Gaussian function and a single sided Crystal-Ball function is used to model the signal shape.

Monte Carlo simulated samples of signal events are produced for W′, Z′, RS1-Graviton, Radion and Bulk-Graviton models using MADGRAPH5_AMC@NLO. For the W′, Z′ and Bulk-Graviton models twelve mass points between 800 and 4500 GeV are produced

in the narrow width approximation for both considered final states. For the W′, Z′, RS1-Graviton and Radion models an additional 5 points between 800 and 4000 GeV are produced for relative widths of 0.1, 0.2 and 0.3 for both final states. Each generated sample contains 50 000 events in the semileptonic case and 30 000 for the all-hadronic final state. All parton showering and hadronisation is done with PYTHIA using the CUETP8M1 tune [115]. The NNPDF 3.0 [56] parton distribution functions are used.

5.2.2. Background Processes

The dominant background in the semileptonic channel comes from QCD processes with a W boson emission; this background is called W+jets. For this background it is important to discriminate between QCD jets and jets that come from a hadronically decaying W decay. Since the resonance search is optimised for heavy resonances, highly boosted W decays are expected, which lead to the hadronically decaying W decaying into one fat jet. Jet substructure techniques are used to determine if a jet is likely to come from a vector boson decay. Subdominant but still important backgrounds in the semileptonic channel are $t\bar{t}$ production, single top production and standard model processes involving the production of two vector bosons, in the following called VV.

The dominant backgrounds in the all-hadronic case are QCD multijet events. As in the semileptonic case V-tagging is used to reduce this background. The other backgrounds of the semileptonic analysis, like VV or single top, are small compared to the QCD multijet background in the all-hadronic case.

For the validation and correction of backgrounds Monte Carlo simulated samples of background processes are used. The W+jets background is simulated using MADGRAPH5_aMC@NLO. The $t\bar{t}$ and single top-quark events are generated with the MC generators POWHEG v2 and MADGRAPH5_aMC@NLO respectively. Standard Model diboson processes are generated with PYTHIA v8.205. Parton showering, hadronisation and PDFs are implemented the same way as in the signal sample generation. The simulated samples are corrected for differences in the lepton trigger efficiency, the lepton identification efficiency, the lepton isolation and the b jet identification efficiency between simulation and data.

5.3. Physics Object Selection and Event Reconstruction

In the CMS detector events are reconstructed combining information from all subdetector systems with the particle flow algorithm in order to reconstruct stable particles like electrons, muon and charged hadrons. To reduce pileup, all hadrons not associated with

the primary vertex are discarded in the jet clustering process. For this analysis events are preselected using the triggers found in table 5.1 for the semileptonic channel and the triggers in table 5.4 for the all-hadronic channel. The kinematic selections used in the analyses are chosen to such that selected events lie in the region with nearly constant trigger efficiency.

5.3.1. Electrons

For the reconstruction of semileptonic events in the electron channel each event is required to contain one electron passing the HEEP6.0 electron ID [69]. This ID already contains isolation requirements and excludes the transition region between the ECAL barrel and the endcaps. The HEEP6.0 electron ID also contains requirements on the transverse energy, measured from track reconstruction compared to the one measured in the ECAL, as well as requirements on the number of ECAL crystals with energy deposits. The variable is designed to discriminate between physical electrons and detector noise, misidentified QCD background or electrons coming from conversions. An electron used for the reconstruction of the leptonically decaying W boson also needs to have a transverse momentum larger than 120 GeV and a pseudorapidity $|\eta|$ smaller than 2.5.

5.3.2. Muons

Events are selected if they contain at least one global muon candidate, that passes the HighPt muon ID [116] with a transverse momentum larger than 53 GeV and $|\eta| < 2.1$. In addition an isolation requirement of $i_t/p_T < 0.1$ is applied to suppress QCD multijet background where jet constituents are misidentified as muons, here i_t is the track isolation, i.e. the sum of transverse momenta of all PF objects in a cone surrounding the muon track. As is the case with all physics object identification the HighPt ID is primarily used to reduce detector noise and contributions from misreconstruction. The HighPt muon ID requires the detection of the muon candidate in the tracker and the muon chambers, to suppress muons from in-flight decays or cosmic rays. The track reconstruction has to have a small χ^2 value and must start closely from the primary vertex. The HighPt ID is optimised for the reconstruction of muons with high transverse energy.

5.3.3. Jets

Both analyses use the anti-k_T algorithm with a clustering parameter of $R = 0.8$ for the clustering of hadron candidates into jets. In the semileptonic analysis a second anti-k_T

clustering with a distance of $R = 0.4$ is used. These jets are then required to pass the inclusive CSV medium working point. Events containing at least one of those jets are discarded in order to suppress the $t\bar{t}$ and single top background. All jets are corrected by applying L1, L2 and L3 jet energy corrections. The jets clustered with a clustering parameter of $R = 0.8$ and $R = 0.4$ are in the following called AK8- and AK4-jets. Jets are furthermore required to either pass a loose jet identification (semileptonic case) or a tight jet identification (hadronic case) [117]. This means that certain conditions on the energy fraction carried by charged/neutral particles as well as on the number of constituents have to be met. This is done in order to discriminate between real jets and detector noise or misidentified other particles. In both analyses the jets are required to have no overlap with reconstructed leptons that pass the criteria in table 5.3, thus requiring the distance between a reconstructed lepton and the jets used for the W boson reconstruction to be larger than $\Delta R = 0.8$.

5.3.4. Semileptonic Final State

A complete overview over all used selection cuts in the semileptonic analysis can be seen in table 5.1. The selection cuts on electron and muon kinematics are designed to reject QCD background as well as select a reconstruction region within the trigger efficiency plateau. In addition selection cuts on the missing transverse energy are applied. These cuts are designed to suppress multijet background. Each event is required to contain exactly one lepton passing the criteria for leptons in table 5.1 and no additional leptons passing the cuts in table 5.2. The events are further required to contain no b-tagged AK4-jet, where the medium working point of the CSV algorithm is used for b-tagging. This cut suppresses $t\bar{t}$ and single top backgrounds. For the hadronically decaying W candidate each event is required to contain at least one anti-k_T jet clustered with $R = 0.8$ and with a p_T larger than 200 GeV. The jet with the largest p_T per event is used to reconstruct the hadronically decaying W boson. Three additional requirements on angular variables (see table 5.1) are used to select a back-to-back topology, as it is expected from the decay of a heavy particle. The pruned mass of the jet reconstruction candidate is used to define four categories. The signal region of 65 GeV $< m_{jet}^{pruned} <$ 105 GeV, which in turn is separated into two categories for WW events 65 GeV $< m_{jet}^{pruned} <$ 85 GeV and WZ events with 85 GeV $< m_{jet}^{pruned} <$ 105 GeV, the lower sideband region 40 GeV $< m_{jet}^{pruned} <$ 65 GeV, and the upper sideband region 135 GeV $< m_{jet}^{pruned} <$ 150 GeV.

5.3.5. Hadronic Final State

A complete overview over all selection cuts in the hadronic final state is listed in table 5.4. Each event must at least contain two anti-k_T jets with a radius parameter of $R = 0.8$

Table 5.1.: All selection cuts and triggers used by the resonance search in the semileptonic WV channel.

physics object	selections
trigger	HLT_Ele105_CaloIdVT_GsfTrkIdT
	HLT_Ele115_CaloIdVT_GsfTrkIdT
	HLT_Mu45_eta2p1
electron	$p_T > 120$ GeV
	$\|\eta\| < 2.5$
	HEEP6
	$E_T^{miss} > 80$
muon	$p_T > 53$
	$\|\eta\| < 2.1$
	trackIso/$p_T < 0.1$
	HighPt
AK8-jet	$p_T > 200$ GeV
	$\|\eta\| < 2.4$
	$65 < m_{jet}^{pruned} < 105$
	loose jet ID
	$\Delta R(j, l) > 1.0$
	HP: $\tau_{21} < 0.6$
	LP: $0.6 \geq \tau_{21} < 0.75$
	highest p_T jet satisfying the cuts is used for reconstruction
W_{lep}	$p_T > 200$ GeV
W_{had}	$p_T > 200$ GeV
WV-System	$700 < m_{VV} < 5000$
	$\Delta\phi(W_{had}, W_{lep}) > 2$
	$\Delta R(l, W_{had}) > \pi/2$
	$\Delta\phi(W_{had}, E_T^{miss}) > 2$
AK4-jets	$p_T > 30$
	$\|\eta\| < 2.4$
	$\Delta R(j, j^{AK8}) > 0.8$
	$\Delta R(j, l) > 0.3$
	CSV medium WP: 0.89
	event must contain no jets passing these selections

Table 5.2.: Lepton selection requirements for the second-lepton veto of the semileptonic analysis.

muon	electron
$p_T > 20$ GeV	$p_T > 35$ GeV
$\|\eta\| < 2.4$	$\|\eta\| < 2.5$ except $[1.4442, 1.566]$
trackIso/$p_T < 0.1$	
HighPt	HEEP6

Table 5.3.: Lepton selections for the jet isolation requirement of the all-hadronic analysis.

muon	electron
$p_T > 30$ GeV	$p_T > 35$ GeV
$\|\eta\| < 2.1$	$\|\eta\| < 2.5$ except $[1.4442, 1.566]$
trackIso/$p_T < 0.1$	
HighPt	HEEP6

and a separation of ΔR larger than 0.8 from any lepton in the event. Lepton candidates used for the overlap veto must pass the cuts in table 5.4. In addition the transverse momentum p_T for each jet has to be larger than 200 GeV. If there are more than two possible candidates the jets with highest p_T are used for the reconstruction. To reduce the dominant QCD multijet background the two jets used for reconstruction are additionally required to pass $|\eta_{\text{jet}_1} - \eta_{\text{jet}_2}| < 1.3$. Furthermore the jet with the highest p_T per event is required to pass the tight jet ID whether or not it is used as a reconstruction candidate for the hadronically decaying vector bosons.

5.4. Event Reconstruction

For the final event reconstruction, events are first preselected according to the criteria described in section 5.3. The vector bosons are then reconstructed and in case of a successful reconstruction of the whole event, final cuts on m_{VV} are applied. The requirements are 500 GeV $< m_{VV} <$ 5000 GeV for the semileptonic channel and $m_{VV} > 1000$ GeV for the all-hadronic channel. The higher mass cut in the all-hadronic case is chosen in order to reach a the trigger efficiency plateau.

5.4.1. Reconstruction of Leptonically Decaying W Boson

In case of a semileptonically decaying W boson, the neutrino, which cannot be directly measured in the detector, has to be reconstructed. For this the measurement of the

Table 5.4.: All selection cuts and triggers used by the resonance search in the all-hadronic VV channel.

physics objects	selections
trigger	HLT_PFHT650_WideJetMJJ900DEtaJJ1p5
	HLT_PFHT650_WideJetMJJ950DEtaJJ1p5
	HLT_PFHT800 or HLT_AK8PFJet360_TrimMass30
	HLT_AK8PFHT700_TrimR0p1PT0p03Mass50
AK8-jets	$p_T > 200$ GeV
	$\|\eta\| < 2.4$
	$65 < m_{jet}^{pruned} < 105$ GeV
	tight jet ID
	no overlap $\Delta R(\text{jet}, l) < 0.8$ with leptons as defined in 5.3
VV-system	$\|\eta_{\text{jet}_1} - \eta_{\text{jet}_2}\| < 1.3$
	$m_{VV} > 1000$ GeV
	$\tau_{21}^{\text{jet}} < 0.45$
	HP: both jets must pass τ_{21} cut
	LP: only one jet must pass τ_{21} cut

missing transverse energy is used as the transverse momentum of the neutrino. The longitudinal momentum, however, cannot be directly reconstructed without using some assumptions. In this analysis the known W mass is used for the reconstruction of the longitudinal neutrino momentum, neglecting the neutrino mass and the mass of the lepton. This leads to a quadratic equation for the transverse momentum of the neutrino $p_{z,\nu}$ following from

$$p_W = p_l + p_\nu \ . \tag{5.2}$$

The solution for $p_{z,\nu}$ is

$$p_{z,\nu}^{(1/2)} = \frac{\mu p_{z,l}}{p_{T,l}^2} \pm \sqrt{\frac{\mu^2 p_{z,l}^2}{p_{T,l}^4} - \frac{E_l^2 p_{T,\nu}^2 - \mu^2}{p_{T,l}^2}} \coloneqq b \pm \sqrt{y} \ , \tag{5.3}$$

$$\mu = \frac{M_W^2}{2} + p_{T,\nu} p_{T,l} \cos(p_{\phi,\nu} - p_{\phi,l}) \ , \tag{5.4}$$

where p_ν is the four momentum of the neutrino, p_l is the four momentum of the lepton and p_W is the four momentum of the leptonically decaying W boson. The mass of the W boson is denoted with M_W and set to $M_W = 80.38$ according to reference [118]. The solutions are chosen according to

$$p_{z,\nu} = \begin{cases} b & , y < 0 \\ \min(|b + \sqrt{y}|, |b - \sqrt{y}|) & , y > 0 \ . \end{cases} \tag{5.5}$$

The choice of $p_{z,\nu}$ in case of imaginary solutions leads to a high mass tail for the reconstructed leptonically decaying W boson.

5.4.2. W/Z Boson Reconstruction using Jet Substructure

To reconstruct the hadronically decaying W boson one fat jet that has to pass requirements on its substructure is used. This reconstruction is basically the same for the semileptonic and all-hadronic final states, except for the substructure requirements on the jets, which are tighter in the all-hadronic case. After preselecting the events, the jets which pass the kinematic analysis selections with the highest and second highest transverse momenta are used as reconstruction candidates. The selected jets are required to have a pruned jet mass within the signal region of the analysis. For the generic limit calculation it suffices if they are within the WW/WZ combined signal window. For the high-purity (HP) category both jets have to pass a 2-to-1-subjettiness requirement of $\tau_{21} < 0.45$ in the all-hadronic case. In the semileptonic channel the reconstruction candidate needs to pass a requirement of $\tau_{21} < 0.6$ for the high-purity category.

5.5. Background Estimation

In order to give limits on a potential signal model the backgrounds of the analysis decay channels have to be estimated and modelled which is done using two different approaches for the considered final states. In the all-hadronic channel the background is modelled via a smooth three-parameter-function, which is fitted alongside the signal function in the limit setting procedure. The semileptonic channel on the other hand uses a data-driven sideband-interpolation method to extract the W+jets background while the $t\bar{t}$ and single top backgrounds normalisations are fixed to the theory cross sections multiplied by the V-tagging scale factors. In the final limit fit, the background parameters are fixed within their uncertainties. Since both background estimations are data-driven, a potential mismodelling in the SM MC samples has only a small effect on the analysis predictions.

5.5.1. V-tagging Scale Factors

V-tagging scale factors are used to correct the differences in MC predictions of the efficiency for the τ_{21} subjettiness cut compared to data. To extract these scale factors the shape in m_{jet}^{pruned} signal region in a control region is fitted to the $t\bar{t}$ MC sample and data. This control region is defined the same way as the signal region of the main analysis only instead of a b-jet veto, one b-tagged jet is required to be in the event. The subjettiness cuts for $\tau_{21} < 0.6$ and $\tau_{21} < 0.45$ are then applied, both to MC and data, to estimate the difference between MC prediction and data due to V-tagging. The scale factors extracted using this method are applied to the background MC samples.

A similar strategy is used to estimate differences in the V-tagging efficiency for signal events. Once again the $t\bar{t}$ MC sample and the top enriched control region are used to estimate the V-tagging efficiencies. Contributions from real reconstructed W bosons and combinatorial background are separated by matching the jets to the W bosons at generator level. The V-tagging efficiencies are then derived through a fit of the functional forms of both real and combinatorial contributions to data. The fit is done simultaneously on events passing the τ_{21} cut and on events failing the cut. Thus four efficiencies are extracted, ϵ_{HP}^{MC} the efficiency of real W bosons to pass the τ_{21} cut in MC, ϵ_{HP}^{data} the efficiency of real W bosons to pass the τ_{21} cut in data and two efficiencies for failing the cut in MC or data ϵ_{fail}. The V-tagging scale factors are then calculated as

$$S_V = \frac{\epsilon_{HP}^{data}}{\epsilon_{HP}^{MC}} \ . \tag{5.6}$$

The scale factors for the low-purity categories are derived using the relation

$$1 = \epsilon_{HP} + \epsilon_{fail} + \epsilon_{LP} \ . \tag{5.7}$$

5.5.2. Background Modelling for the Semileptonic Channel

The semileptonic analysis uses a data-driven sideband interpolation method, called alpha method, to completely determine the dominant background contributions. For this the functional forms of the three main backgrounds W+jets, $t\bar{t}$ and single top production and VV are extracted from simulation. Two different functional forms are extracted for each background, one described the distribution in the m_{jet}^{pruned} spectrum and the second forms describe the distribution in the invariant mass spectrum. For the normalisation of the $t\bar{t}$, single top and VV backgrounds the NLO theory cross section is multiplied by V-tagging scale factors derived from a data-MC comparison in a top-enriched control region. The normalisation of the dominant W+jets background is determined through a fit in the lower sideband. The functional shapes that are used can be found in reference [113]. The functional shape in the m_{VV} signal region is derived via a transfer function $\alpha^{MC}(m_{VV})$ using the lower sideband only

$$\alpha^{MC}(m_{VV}) = \frac{F_{SR}^{MC}(m_{VV})}{F_{SB}^{MC}(m_{VV})} \ , \tag{5.8}$$

where $F_{SB}^{MC}(m_{VV})$ is the functional shape of the W+jets background in the sideband and $F_{SR}^{MC}(m_{VV})$ is its functional shape in the signal region. This function is completely derived from MC predictions. In order to calculate the complete background prediction in the signal region, the probability distribution function of W+jets derived from the low sideband region $F_{SB}^{data,corrected}(m_{VV})$ is propagated to the signal region using the alpha function defined in equation (5.8). $F_{SB}^{data,corrected}(m_{VV})$ is corrected by subtracting the

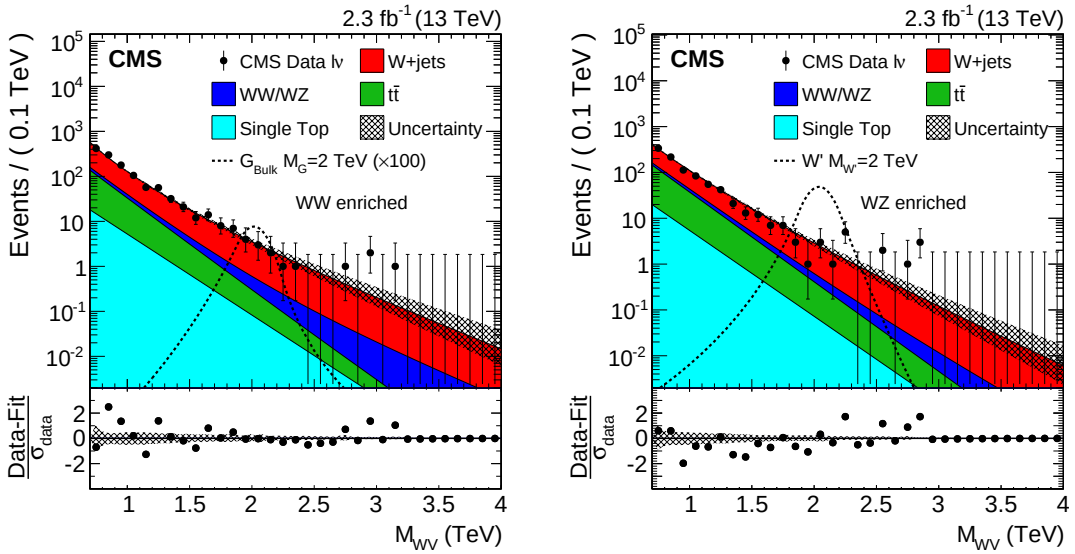

Figure 5.5.: The final observed m_{VV} distribution in the signal region for the semileptonic channel. On the left is the result for the WW category and on the right for the WZ category; the electron and muon channel are combined. The backgrounds are fixed as described in section 5.5.2. As an example a narrow Bulk-Graviton resonance with a mass of 2 TeV is shown enlarged by a factor of 100. In each figure the solid curve represents the background estimation provided by the alpha ratio method. The hatched band includes both statistical and systematic uncertainties. The data are displayed as black markers. At the bottom of each plot, the bin-by-bin fit residuals, $(N_{Data}-N_{Fit})/\sigma_{Data}$, are shown together with the uncertainty band of the fit normalised by the statistical uncertainty of data, σ_{data}.

contributions of the smaller backgrounds. The background prediction thus looks like

$$N_{SR}^{BKG}(m_{VV}) = C^{V+jets} \cdot \alpha^{MC}(m_{VV}) \cdot F_{SB}^{data,corrected}(m_{VV}) + \sum_k C^k F_{MC,SR}^k(m_{VV}) \ , \tag{5.9}$$

where C^i denotes the normalisation for different backgrounds and $F_{MC,SR}^i$ is the probability density function for different backgrounds in the signal region. This method fixes all background contributions before the limit setting, thus introducing no potential biases when extending the analysis to broader resonances, see chapter 6.

In figure 5.5 the final m_{VV} distribution in the signal region is shown, with the shapes and normalisations of the MC backgrounds fixed as described above.

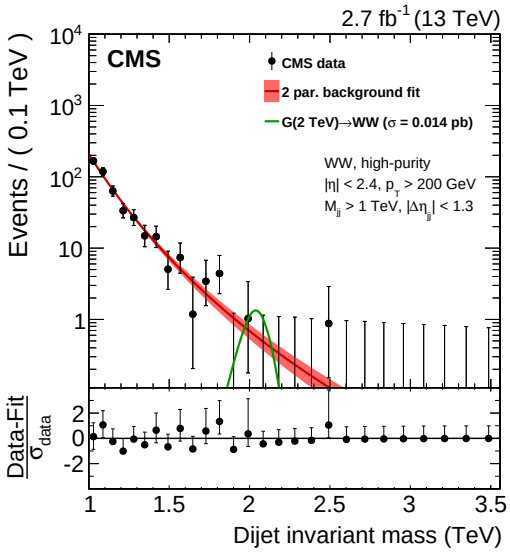

Figure 5.6.: The final observed m_{VV} distribution in the signal region for the all-hadronic channel. As an example only the high-purity WW category is displayed. The solid curve represents a background-only fit to the data distribution where the filled red area corresponds to the 1 sigma statistical error of the fit. The data are shown as black markers. At the bottom of each plot, the bin-by-bin fit residuals, $(N_{Data} - N_{Fit})/\sigma_{Data}$, are shown with σ_{Data} being the statistical uncertainty of data. As an example the signal shape for a Bulk-Graviton model is shown for a resonance mass of 2 TeV.

5.5.3. Background Modelling for the All-Hadronic Channel

In the all-hadronic channel one functional form is used to fit all backgrounds. In the original analysis for different regions in m_{jet}^{pruned} a two- or three-parameter function is used; however, in the simplified analysis categories of this thesis only one three-parameter function

$$\frac{dN}{dm} = \frac{P_0 \cdot (1 - \frac{\sqrt{s}}{m})^{P_1}}{(\frac{\sqrt{s}}{m})^{P_2}} \tag{5.10}$$

is used to determine background contributions. The fit function is chosen based on MC studies; m denotes the dijet invariant mass, $\sqrt{s}$ the center of mass energy and the P_i are fit parameters. It was tested on data in a sideband region defined by selecting events with one jet with a pruned mass between 20 GeV and 65 GeV, that the functions are sufficient in describing the backgrounds of the dijet channel and that for narrow signals no bias is introduced through the choice of fit function. In figure 5.6 the final observed m_{VV} distribution is shown with a background-only fit.

5.6. Systematic Uncertainties

In the following the systematic uncertainties are discussed for both decay channels. A summary of all uncertainties can be seen in tables 5.5, 5.6 and 5.7. In principle two kinds of uncertainties can be distinguished. Those are scale uncertainties, which only affect the overall scale, i.e. the number of expected signal or background events, and shape uncertainties, which affect the shapes of signal or background distributions. Both sources of uncertainties are considered in the semileptonic and all-hadronic case. Uncertainties on the scale can have various causes; they can be caused by uncertainties in the measurement of important quantities or be related to the modelling procedure. Most uncertainties that are caused by the measurement of quantities affect both background and signal predictions. The most straightforward of those is the uncertainty on the integrated luminosity of the sample, which affects the numbers of both non-data-driven background and signal events. In addition to this there are uncertainties for the efficiency of lepton triggers and identification assigned, which are derived from a sample of $Z \to ll$ events. The effects of uncertainties on the energy scales are estimated by propagating the uncertainties throughout the entire analysis, including MET in the semileptonic case. This is done for the lepton and jet energy scale and resolution, affecting both the measured signal efficiency and the mean and width of the fitted signal peak. Another source of systematic uncertainties in both analyses is the V-tagging scale factor, the uncertainty of which is applied as an uncertainty on the event yield.

There are two uncertainties that originate in the modelling procedure, one is the limited number of events in the sideband fit, the other are uncertainties due to the choice of fit function. These have to be evaluated for each background that is fitted separately, as well as for the signal shapes and normalisations.

Lastly, uncertainties due to the overall renormalisation and factorisation scales are evaluated by reweighting the scales independently by factors of 2 and 1/2 and redoing the MC production. PDF uncertainties are evaluated similarly using the PDF4LHC prescription found in reference [57] in order to take the effects of different PDF models on the signal efficiency into account.

5.6.1. Systematic Uncertainties for WV $\to$ lvjj

The shape and scale uncertainties due to a limited amount of events in data and due to the choice of fit function are evaluated for the W+jets background only, its dominant contribution comes from the uncertainties on fit parameters due to the limited amount of events in the data sideband. For the minor backgrounds shape uncertainties are neglected and the uncertainty on the scale is taken to be the V-tagging and NLO cross section prediction uncertainties added in quadrature. In addition to these background

source	signal norm.	mean	RMS
luminosity	5%	-	-
PDF	13%	-	-
scales	11%	-	-
V-tagging	14%	-	-
trigger	1%		
lepton ID	1%(μ) 3%(e)		
jet energy scale	+[16%-33%] −[15%-25%]	1.3%	1%-3%
jet energy res.	$< 0.1\%$	0.1%	3%
lepton energy scale	0.7%(μ) 0.2%(e)	0.1%(μ) 0.1%(e)	0.5%(μ) 0.1%(e)
lepton energy res.	0.1%	0.1%	0.1%
b-tag ID	0.2%	-	-

Table 5.5.: A summary of all systematic uncertainties for the signal modelling in the semileptonic decay channel in terms of the effect on shape and/or normalisation of the signal. The uncertainties are only given for the HP category. The impact of the uncertainties are given on the mean of the reconstructed mass and on the smearing (RMS) of the signal width.

uncertainties the jet and lepton energy scale and resolution uncertainties are propagated throughout the analysis. Since the effects of uncertainties of the energy scales and resolutions are propagated to the MET, effects of uncertainties in MET energy scale and resolution do not have to be evaluated independently. However, in the semileptonic case the difference in mean mass values for the fitted W-peak between data and simulation in the top-enriched control region of the m_{jet}^{pruned} mass spectrum is taken as another systematic uncertainty on the pruned jet mass, and its effects on the signal yield are also taken into account. The uncertainty on the signal yield due to b-tagging is evaluated through a scaling of signal weights in MC. With the exception of the lepton energy scale and resolution uncertainties and the trigger uncertainties of the two lepton categories, which are assumed to be uncorrelated, the analysis assumes all other uncertainty sources to be fully correlated for the different signal categories. In tables 5.5 and 5.6 all uncertainties and their impacts on the model parameters are listed.

5.6.2. Systematic Uncertainties for VV $\rightarrow$ jjjj

In the all-hadronic final state the systematic uncertainties of jet energy scale and resolution, V-tagging scale factors and luminosity are taken into account. Only the jet energy scale and resolution are propagated to estimate the error on the signal shape, all other uncertainties are taken as uncertainties on the event yield. Since the parameters of the background functions are left floating in the final limit calculation there are no uncertainties assigned to the background estimation. A list of all considered uncertainties and

source	W+jets	$t\bar{t}$ and single top	VV
luminosity	-	5%	5%
PDF	-	5%	3%
V-tagging	-	-	14%
background norm.	8%(μ) 9%(e)	5%(μ) 8%(e)	13%
background shape	error fit par.$\times\sqrt{2}$	-	-
trigger	-	1%	1%
lepton ID	-	1%(μ) 3%(e)	1%(μ) 3%(e)

Table 5.6.: A summary of all systematic uncertainties for the background estimation in the semileptonic decay channel. Uncertainties affect shape and/or normalisation. The uncertainties are only given for the HP category. For the W+jets shape uncertainty the error of the fit parameters is taken, scaled by a factor of $\sqrt{2}$.

source	yield	migration	shape
luminosity	4.3%	-	-
pileup	2%	-	-
jet energy scale	0.4%-1.5%	1%-46%	2%
jet energy resolution	0.1%-1.3%	-	10%
V-tagging		44%	

Table 5.7.: A summary of all systematic uncertainties in the all-hadronic decay channel. Uncertainties affect shape and/or normalisation of the signal. The values given are only for the HP category.

their respective values can be found in table 5.7.

5.7. Limit Setting Procedure

To calculate the 95% CLs limits both analyses use the Combine framework [112]. All systematic uncertainties are added as nuisance parameters in the limit setting procedure. Systematic uncertainties are treated as nuisance parameters and profiled in the statistical interpretation using log-normal prior distributions for normalisation uncertainties and Gaussian prior distributions for shape uncertainties. Both channels use unbinned shape analysis with different background estimations. The limits shown in figure 5.7 are statistical combinations of both final states for each signal model. In the combination the uncertainties of the jet energy scale and resolution, the V-tagging scale factors and luminosity are assumed to be 100% correlated. In figure 5.7 the combined limits can be seen, along with the theory prediction for a Bulk-Graviton and W$'$ model. For both theory models upper limits on the production cross section are given for a mass range of

1000 to 4000 TeV, which are the most stringent today in this final state. The expected and observed limits are compatible thus giving stringent upper limit on the production cross sections of the considered models.

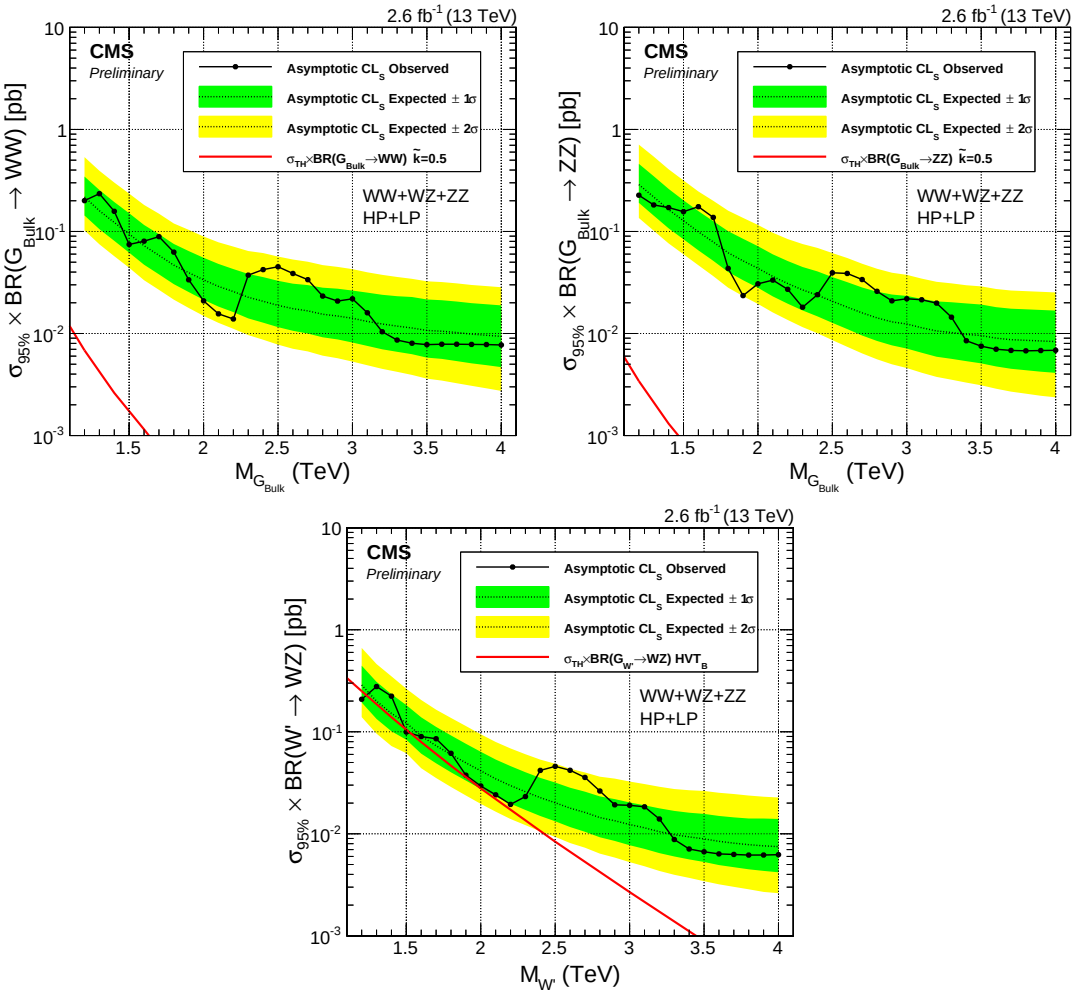

Figure 5.7.: Limits for the all-hadronic and semileptonic channels combined. The limits are given on the branching fraction multiplied with the cross section of the theory model and as a function of the resonance mass. The top left figure contains limits for a $G_{Bulk} \to WW$ model; on the top right are limits for a $G_{Bulk} \to ZZ$ model. On the bottom limits for the HVT model B are shown.

6. Model-Independent Limits

The goal of this work is to provide a set of generalised limits and a framework that allows the calculation of exclusion bounds for generic models. This way theorists can profit from the results of the CMS diboson resonance search of 2016 even if their specific model was not considered in the main limit setting procedure. Since numerous models exist that address beyond-the-standard-model physics, it is impossible for a dedicated analysis to address every possible model. Instead most analyses use one or two specific models which are either considered important, or they use an effective field theory generalisation of a class of different models. But even so only a part of possible theory models can be addressed in this way.

The first section of this chapter contains a description of the analysis strategy as well as the intended usage for model-builders and theorists. In section 6.2 the analysis categories are discussed followed by the signal parametrisation in section 6.3 and the signal shape modelling in section 6.4. Section 6.5 discusses the calculation of the two dimensional grid of model-independent limits. The last section of this chapter contains a proof of concept, through applying the described method on the example of an RS1-Graviton model. Although this work builds on two distinct analyses realised for two different final states, in this thesis the two final states will be referred to as the all-hadronic channel and the semileptonic channel, respectively.

6.1. Analysis Strategy

In order to derive a model-independent limit, the model dependence needs to be eliminated in each step of the main analysis. To accomplish this the following steps are implemented: The analysis categories are simplified to facilitate the usage of the model-independent framework, at a moderate price in terms of performance. A model-independent estimation of the reconstruction and identification efficiencies within the analyses is developed in order to provide an estimation of the signal yield for generic models. The systematic uncertainties due to imperfections of this estimation are included in the calculation of the model-independent limits as an additional uncertainty on the signal yield. This procedure has the advantage that no uncertainties have to be applied in the estimation of signal yields for a generic model, since the necessary systematics are

already included in the model-independent limits. The generalisation to a generic model interpretation makes an expansion of the signal shape modelling to broad resonances necessary, since the assumption of a signal width smaller than the detector resolution is no longer applicable. The model-independent limits are then calculated for a two-dimensional grid of different resonance masses and widths. As a last measure the limits are given on the number of signal events, instead of on the cross sections in order to remove the model dependence of the signal yield expectation, which depends on the reconstruction efficiency.

6.2. Definition of Categories

In order to avoid a dependence on model-specific assumptions and to simplify the analyses several categories of the main analysis are discarded or combined. In particular the low-purity category in both the semileptonic and the all-hadronic channels is discarded, since its efficiency strongly depends on the polarisation. This means a small loss in sensitivity which is, however, low over a large mass spectrum and almost exclusively affects the limits for large resonance masses. In light of the considerable simplification the loss in sensitivity is acceptable, since it would otherwise be necessary to calculate all efficiency histograms for the high- and low-purity categories separately. Furthermore the two mass categories are combined into one signal category with a pruned jet mass between 65 GeV $\leq m_{jet}^{pruned} \leq$ 105 GeV to retain efficiency if the produced W or Z bosons do not fall into their respective mass windows and also to reduce model dependent migration effects. The two lepton categories in the semileptonic case are retained and combined statistically in the limit setting procedure.

6.3. Generalisation of Signal Yields

This section is dedicated to describing and testing a generalised method to determine signal yields for arbitrary theory models. There are two reasons for this generalisation of the signal yield of the analyses. One objective is to get a scheme with which to calculate the expected signal yield of a generic model. For this the identification and reconstruction efficiencies are parametrised and calculated using the MC samples of the Bulk-Graviton an W′ models. The second reason is to eliminate the dependence of the limit on the model-specific expected yield of signal events. To eliminate this dependence the limit is calculated on the number of signal events instead of on the cross section, and additional uncertainties on the signal yield are added in the limit calculation. These uncertainties include possible differences in the reconstruction efficiencies due to variations in kinematics or resonance widths. In the following chapter the product of acceptance and efficiency will be denoted as acceptance×efficiency for the sake of brevity.

Table 6.1.: Selection criteria on the generator level kinematics for the semileptonic channel. The selection cut on the missing transverse energy has to be applied to the transverse momentum of the neutrino.

Objects	Requirements
Muons	$\lvert\eta\rvert < 2.1$
	$p_T > 53$ GeV
Electrons	$\lvert\eta\rvert < 2.5$
	$p_T > 120$ GeV
E_T^{miss}	$p_T > 40$ GeV (muon channel)
	$p_T > 80$ GeV (electron channel)
W$\rightarrow l\nu$ or W$\rightarrow l\nu\nu\nu$	$p_T > 200$ GeV
W/Z$\rightarrow$ q$\bar{\text{q}}'$	$p_T > 200$ GeV
WV system	700 GeV $< m_{WW} <$ 5000 GeV
	$\Delta\phi(V_{had}, W_{lep}) > 2$
	$\Delta\phi(V_{had}, E_T^{miss}) > 2$
	$\Delta R(V_{had}, l) > \frac{\pi}{2}$

Table 6.2.: Selection requirements on the generator level kinematics for the all-hadronic channel.

Objects	Requirements
V $\rightarrow q\bar{q}'$	$p_T > 200$ GeV
	$\lvert\eta\rvert < 2.4$
VV system	1000 GeV$< m_{VV}$
	$\lvert\eta_{V_1} - \eta_{V_2}\rvert < 1.3$

6.3.1. Analysis Acceptance

The analysis acceptance is defined as

$$\text{GE} = \{e \in \text{all Events generated}\} \,, \tag{6.1}$$

$$\text{GE}_{passed} = \{e \in \text{generated Events that passed kinematic cuts}\} \,, \tag{6.2}$$

$$\text{Acceptance} = \frac{\sum\limits_{i \in \text{GE}_{passed}}}{\sum\limits_{i \in \text{GE}}} \,. \tag{6.3}$$

The events in the numerator are required to pass the kinematic cuts found in table 6.1 for the semileptonic channel or table 6.2 for the all-hadronic channel. It is important to note that the acceptances of the analyses also depend on the model predictions. Since many kinematic selections are chosen in order to reach the plateau in the trigger efficiencies the dependence of these selections on model predictions is small.

Since the recipe for the calculation of efficiencies for generic signal models depends on a seperation of acceptance and efficiency the possibility of migration of events has to be considered. Migration means that it is possible that events do not pass the analysis selections on generator level but do pass the analysis selections after the showering, hadronisation and detector simulation steps have been applied, or vice versa. This effect is largest for samples of small resonance masses, where the lepton or quark kinematics are closer to the selections on the respective variables. Differences in efficiency of up to 20% between a selection on generator and on reconstruction level is observed. Due to the procedure of the calculations of the reconstruction efficiencies the effects of downward migration are already included in the given efficiency tables. The effects of upward migration cannot be included in this procedure but they are addressed in the uncertainties used for the final limit setting.

6.3.2. Identification and Reconstruction Efficiencies

In order to be able to reweight specific theory models according to the identification and reconstruction efficiencies of the analyses, those efficiencies are calculated as a function of the generated W or Z boson kinematics. The efficiencies are calculated from MC samples for different resonance masses of a Bulk-Graviton model and a W′ model. Since all efficiencies are extracted from MC samples, the V-tagging efficiency scale factors are applied to correct the differences between MC and data. The reconstruction and identification efficiencies within the two CMS analyses are listed in the tables in appendix A. In order to reproduce the complete analysis efficiency the efficiency of the vetoes and the generator cut on $\Delta\eta_{jj}$ have to be considered separately. The effects of W or Z boson polarisation on the efficiency has to be taken into account as well. These quantities are discussed in subsection 6.3.3.

Calculation of Identification and Reconstruction Efficiencies

The identification and reconstruction efficiencies include in addition to the efficiency of identifying and reconstructing a certain physics object also the trigger efficiencies, V-tagging efficiencies, b-tag veto efficiency and the downward migration of events over selection cuts. An additional scale factor $\epsilon_{polarisation}$ corrects the differences in V-tagging efficiency for transverse and longitudinal polarised vector bosons. In principle they are calculated using the ansatz

$$\epsilon = \epsilon_1\left(p_T^{V_1}, \eta^{V_1}\right) \cdot \epsilon_2\left(p_T^{V_2}, \eta^{V_2}\right) \cdot \epsilon_{veto} \cdot \epsilon_{polarisation} \ , \tag{6.4}$$

$$\epsilon_i\left(p_T^{V_i}, \eta^{V_i}\right) = \frac{N_{sel}\left(p_T^{V_i}, \eta^{V_i}\right)}{N_{gen}\left(p_T^{V_i}, \eta^{V_i}\right)} \ . \tag{6.5}$$

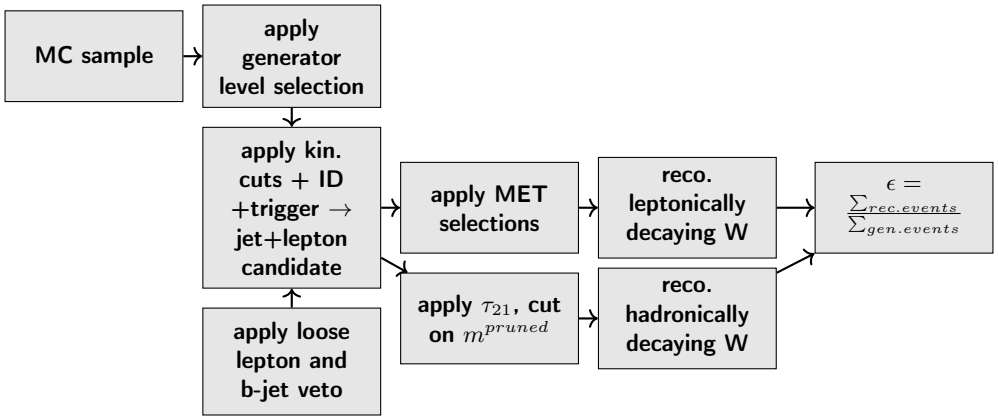

Figure 6.1.: A schematic overview over the calculation scheme for the reconstruction and identification efficiencies in the semileptonic channel. Bulk-Graviton and W′ MC samples are used for the calculation.

Here N_{sel} is the number of events passing all analysis selections, including the selections found in table 6.1 and 6.2, while N_{gen} is the number of events passing the generator level kinematic selections. For this calculation all cuts are applied on the final kinematics of the event i.e. the Monte Carlo kinematics after the full detector simulation. The efficiencies are parametrised using the generated kinematics of the reconstructed W bosons or Z bosons in order to allow an easy application of the efficiency tables to generated MC events. Only events passing the kinematic selections on generator level are used, thus upward migration over kinematic selection cuts is not taken into account. A schematic overview over the efficiency calculation for the semileptonic channel is shown in figure 6.1. A similar procedure is used for the all-hadronic case, see figure 6.2. In this channel the efficiencies are separately calculated for W^+ bosons and W^-bosons, or for the Z boson with leading and subleading p_T. The resulting distributions for the efficiencies of either a hadronic W^+ or W^-boson are added and provided as one efficiency in figure 6.4.

As can be seen in equation (6.5) the efficiencies are parametrised after the generated kinematic variables of the vector bosons, in particular the transverse momentum and pseudorapidity. These variables are chosen following the assumption that the angle of production ϕ around the z-axis does not impact the efficiency of reconstructing or identifying the event, since the detector is rotationally symmetric with respect to this axis.

The calculation scheme also assumes that the respective reconstruction and identification efficiencies of both vector bosons are independent, which is a reasonable assumption even in the all-hadronic case where the same subdetectors are used for the reconstruction of both fat jets, since the vector bosons are still separated in their angular distribution. This is also the reason why for the all-hadronic decay channel only one efficiency distribution is sufficient for both hadronically decaying vector bosons.

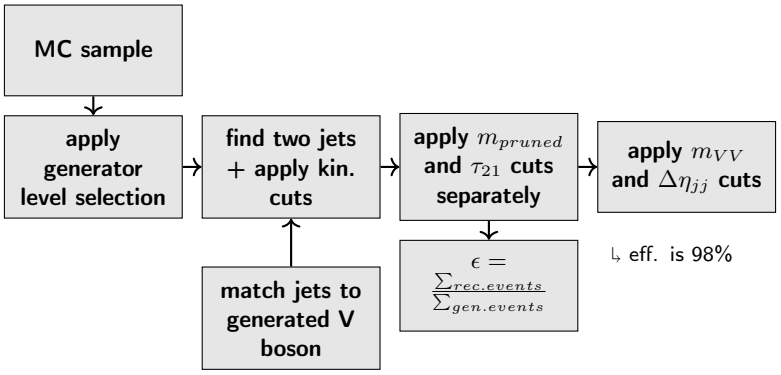

Figure 6.2.: A schematic of the calculation scheme for reconstruction and identification efficiencies in the all-hadronic channel. The jets are matched to W^+ and W^-or to the Z bosons ordered in p_T with $\Delta R < 1$. Events with unmatched jets are discarded. The efficiency for the $\Delta\eta_{jj}$ cut is calculated afterwards and amounts to an overall factor of 98%.

In figure 6.3 the resulting efficiencies are shown for the semileptonic decay channel and in figure 6.4 they are shown for the all-hadronic decay channel. The efficiencies were calculated using Monte Carlo samples of a Bulk-Graviton model and a W' model, respectively. Varying bin sizes are used to accommodate a similar number of events per bin. Comparing the efficiencies for the hadronically decaying V boson for both final states it is apparent that the semileptonic analysis has a higher efficiency for this object. This is due to the tighter τ_{21} selection in the all-hadronic channel.

In a series of consistency tests, the applicability and plausibility of this approach was thoroughly tested. For this the efficiency obtained using all analysis cuts on reconstructed simulated events and the efficiency obtained by using the parametrisation scheme supplied within this thesis are compared for different scenarios. As a result of these tests it is concluded that the calculation scheme for the analysis efficiencies works well for the five different theory models tested; it is therefore reasonable to assume that this approach gives plausible results for arbitrary models.

Efficiency Dependence on the Resonance Width

To test the dependence of the efficiency on the resonance width the efficiency is calculated for resonance masses of 800, 1200, 2000, 3000 and 4000 GeV and relative widths of 0.1, 0.2, and 0.3. For the calculation two different approaches are used. The real efficiency is calculated by applying the selections of the analyses whereas the parametrised efficiency is calculated following the description detailed in section 6.6. The results for both efficiency calculation schemes can be seen in appendix B. The kinematic distributions of

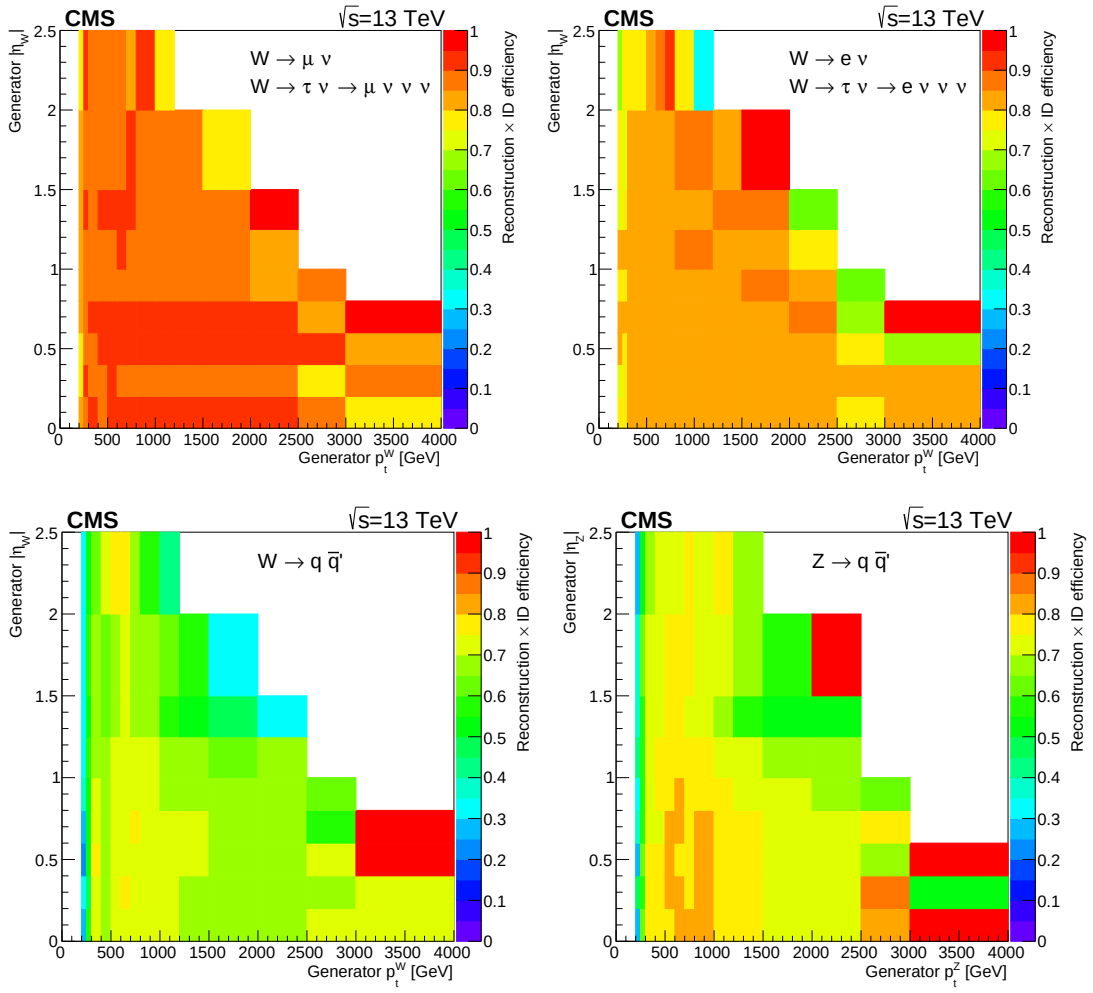

Figure 6.3.: The reconstruction and identification efficiencies for the $W \to \mu\nu$ and $W \to \tau\nu \to \mu\nu\nu\nu$ (top left) and $W \to e\nu$ and $W \to \tau\nu \to e\nu\nu\nu$ (top right), $W \to q\bar{q}'$ (bottom left) and $Z \to q\bar{q}$ (bottom right) bosons. The efficiencies are given as a function of the generated p_T and η of the W boson or Z boson, respectively.Bins at the edge of the covered phase space contain few events and are therefore mostly driven by statistical fluctuations.

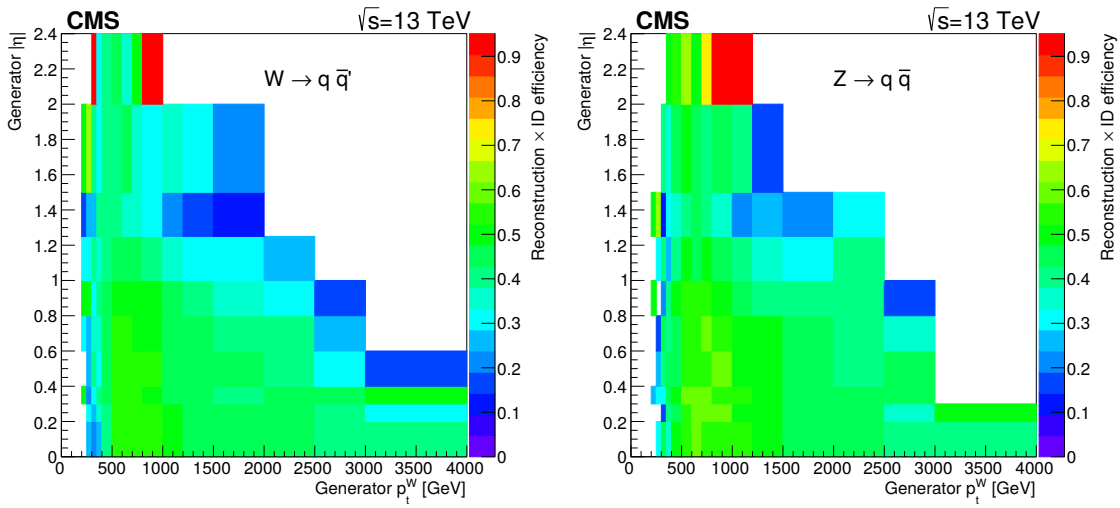

Figure 6.4.: The reconstruction and identification efficiencies for the WW→ $q\bar{q}'q\bar{q}'$ decay channel as a function of the generated transverse momentum p_{T} and the absolute value of the generated pseudorapidity η of the W boson. On the right hand side is the reconstruction and idendification efficiency for the ZZ→ $q\bar{q}q\bar{q}$ channel, likewise as a function of the generated transverse momentum and the pseudorapidity of the hadronically decaying Z boson. Bins at the edge of the covered phase space contain few events and are therefore mostly driven by statistical fluctuations.

samples for broad resonances are spread over a larger region in phase space, for example the p_{T} distribution contains a wider spectrum of values. Due to the parametrisation of efficiencies as functions of p_{T} and the pseudorapidity, potential effects of a larger kinematic spread are already covered by the parametrisation. The overall dependence of the efficiency on the resonance widths is small- about a relative difference of 2% between widths- since the bulk of the events is in the same kinematic region for each sample of the same mass. As an example the real acceptance×efficiency is shown as a function of the resonance width for a Z' model decaying to the semileptonic final state and for a Radion model decaying to the all-hadronic final state, see figure 6.5.

It should be noted that although the efficiencies do not have a strong dependence on the resonance width, the acceptance of the analysis can change significantly when introducing signals with large widths. Such a drop in acceptance can be expected when the mean value of the resonance mass is in the vicinity of one of the mass cuts. If a resonance is produced with a larger spread in the m_{VV} spectrum more events will fail the acceptance cut on the resonance mass, thus leading to significantly lower acceptances.

Efficiency Dependence on the Resonance Mass

As can be seen in figure 6.6 and the tables in appendix B the efficiency depends on the resonance mass. It shows a significant loss for higher masses. The reason for this lies in the high transverse momentum of the produced vector bosons, which results in highly collimated jets. Since the substructure techniques used for V-tagging depend on a separation between the two subjets the V-tagging efficiency decreases with the p_{T} of the vector boson. Figure 6.6 shows the acceptance×efficiency of the analysis over the resonance mass for all considered final states and for different models. In the semileptonic channel the mass dependence of the efficiency shows a turn on behaviour for small masses, since the phase space for such resonances contains more events that do not pass the kinematic selections of the analysis. For high masses both channels display the discussed reduction in efficiency due to the substructure selections. These effects are more pronounced in the all-hadronic channel because of tighter requirements that have to be met by two jets. In principle the loss of efficiency for larger resonance masses is already properly taken care of with the used parametrisation that depends on the transverse momentum of the hadronically decaying vector boson. As can be seen in the tables in B the agreement between parametrised and real efficiencies is stable over almost the whole mass range, with the exception of the smallest mass point in the respective analysis i.e. 800 GeV for the semileptonic case and 1200 GeV for the all-hadronic case. The large disagreement between the true analysis efficiency and the modelling through parametrisation and reweighting of events in this bin is due to the migration of events over kinematic cuts. In particular there are some samples where the upward migration over the MET cut far outweighs the downward migration. These migration effects are especially pronounced when in total few events pass the selection criteria, as is the case for small resonance

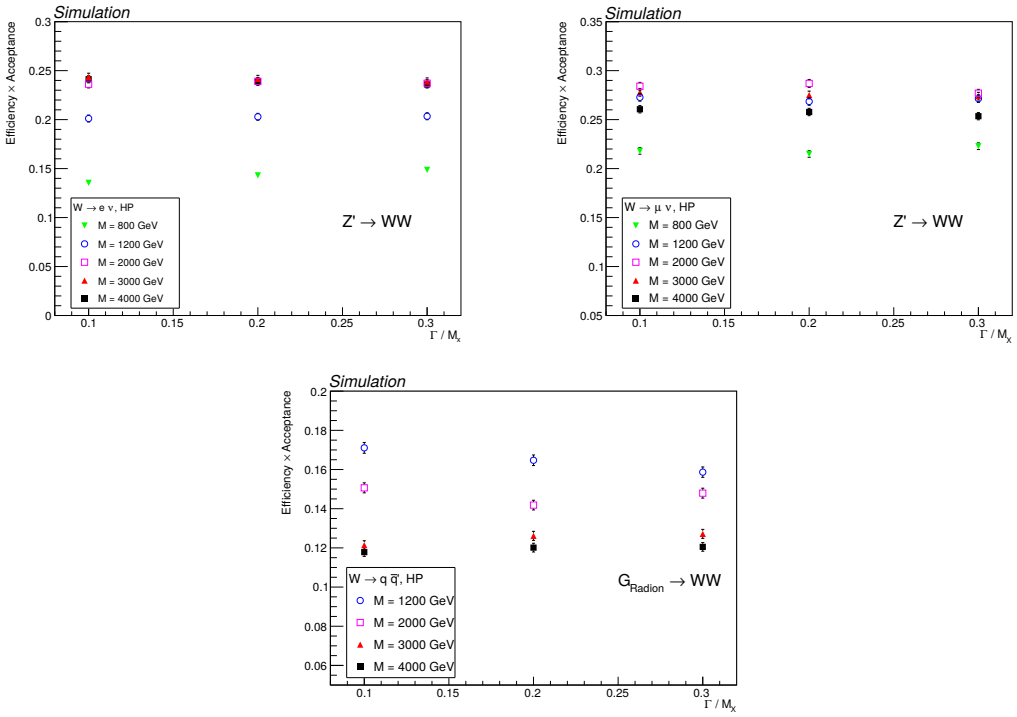

Figure 6.5.: The analysis efficiency×acceptance over the relative resonance width Γ/m_{VV} for different mass points. On the top a Z′ model is used for the calculation of efficiencies. On the left is the electron channel and on the right the muon channel. On the bottom the efficiency is extracted from MC samples of a Radion model with two W bosons as intermediate state and a fully hadronic final state.

Table 6.3.: The scale factors for the vetoes of the semileptonic analysis, the polarisation scale factors and the scale factor for the $\Delta\eta_{jj}$ cut of the all-hadronic analysis. All scale factors are derived from MC.

	semileptonic channel		all-hadronic channel
intermediate state	WW	WZ	WW/WZ/ZZ
loose lepton veto	0.999	0.998	-
b-jet veto	0.94	0.96	-
polarisation factor	0.76	0.76	0.74
$\Delta\eta$ cut	-	-	0.98

masses beyond the narrow width approximation. In these cases the migration effects can cause a relative difference in efficiency of around 20%, which leads to larger uncertainties in the limit calculation for small masses, as discussed in section 6.3.4.

6.3.3. Veto and Polarisation Efficiencies

In order to correctly model the complete analysis efficiency the vetoes on a second lepton and on b-tagged jets of the semileptonic analysis, as well as the effects of vector boson polarisation on jet substructure techniques have to be taken into account. Since the all-hadronic analysis uses a cut on $\Delta\eta$ of the two fat jets used for the vector boson reconstruction the loss in efficiency due to this selection has to be taken into account as well. All of these effects are independent of the kinematics of the vector bosons produced in the exotic decay and can therefore be described by a single scale factor each. In table 6.3 the efficiency scale factors are listed.

Second-Lepton Veto

The semileptonic analysis requires the existence of exactly one lepton per event. Events with an additional loose lepton, as defined in section 5.3, are not used in the analysis. This veto is independent of the vector boson kinematics since the additional lepton does not originate in the signal process directly. For signal events a real lepton can only be produced in a pileup event or inside a jet during the interaction with the detector or in $Z \to b\bar{b}$ events, where a lepton leaves the jet cone. Another possibility is the misidentification of another particle. Such events that contain a second lepton with enough energy to pass the kinematic requirements and isolation of a loose lepton are rare. There are, however, SM background processes which can lead to the production of a second lepton that are suppressed by the second-lepton veto.

The efficiency of this veto is calculated by summing all events containing a second lepton

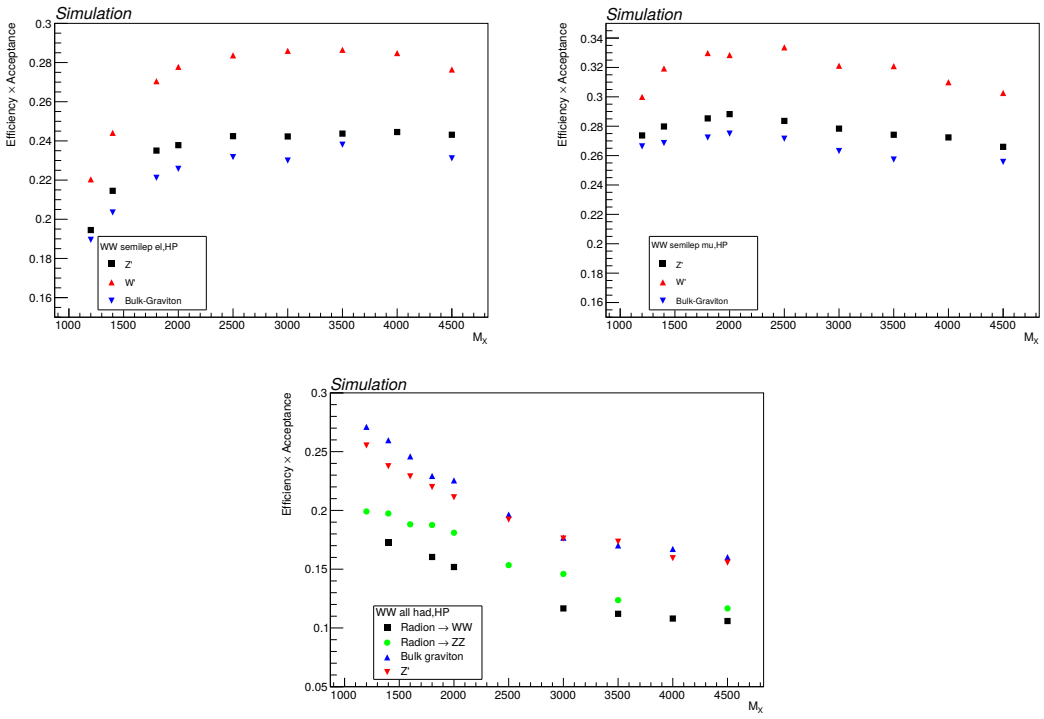

Figure 6.6.: The analysis efficiency×acceptance over the resonance mass for different models. On the top the efficiency×acceptance in the electron category (top left) and in the muon category (top right) is shown for narrow width Z′, W′ and Bulk-Graviton models. On the bottom MC samples for narrow width Radion, Bulk-Graviton, Z′ models were used for the calculation. The W′ model has an intermediate state of one W and one Z boson, while for the Bulk-Graviton, Z′ and Radion models intermediate states with two W bosons are used for the calculation. For the Radion model a second set of MC samples with two Z bosons as intermediate states are used for the calculation in the all-hadronic final state.

with loose requirements and dividing by the number of generated events. For these calculations all mass points of the narrow width Bulk-Graviton and W′ MC samples are used. The efficiency for the second-lepton veto amounts to 0.999 in case of a WW intermediate state and 0.998 for an intermediate state of one W boson and one Z boson.

B-Jet Veto

In order to reduce the background from $t\bar{t}$ production a veto on additional anti-k_T jets with a clustering parameter of $R = 0.4$ that pass the medium WP of the CSV algorithm is introduced. The jets used for this veto are also required to have an angular separation of ΔR larger than 0.8 from the fat jet reconstruction candidate, and an angular separation of ΔR larger than 0.3 from the lepton in the event. As in the case of the additional leptons such a jet can be produced through the emission of a b quark from one of the final or initial state partons for signal processes. The probability for this emission is higher than for the appearance of an additional lepton, since the emission can arise from a strong interaction. The amount of signal process events containing such a b-tagged jet, either through real emission or due to a mistagging, is, however, low. This veto works well to suppress backgrounds due to $t\bar{t}$ production or single top production since the top quark decays into a bottom quark and a W boson with a branching ratio of almost one hundred percent. The efficiency for this veto for signal processes is calculated the same way as the second-lepton veto. Its value is 0.94 for a WW intermediate state and 0.96 for a WZ intermediate state. The higher rejection rate for WZ intermediate states is due to events where the hadronic Z boson decays to a $b\bar{b}$ pair, which can be accidentally rejected if at least one of the quarks gets clustered into a slim jet.

Effects of Vector Boson Polarisation

Since most models predicting an exotic resonance in the diboson channel are attempts to include gravity into the standard model, the couplings to longitudinally polarised vector bosons are usually larger than those to transversely polarised vector bosons. This means that most of the models considered by this analysis produce almost exclusively longitudinally polarised vector bosons. However, the effect of the vector boson polarisation has to be considered to allow model-builders to use the framework even if their specific model does not primarily produce one polarisation. The dependence on the vector boson polarisation is studied using MC samples produced for the RS1-Graviton model, in which 90% of all produced vector bosons are transversely polarised. this difference in efficiency between polarisations exists only for hadronically decaying vector bosons, for the leptonically decaying W bosons there is no difference in the reconstruction efficiencies since this difference is already included in the analysis acceptance.

For the reconstruction of hadronically decaying bosons fat jets that fulfil certain requirements on the substructure are used for the reconstruction. The polarisation does have an impact on the efficiency of the τ_{21} cut and the cut on the pruned jet mass. The first effect, which is investigated in detail in reference [85], is a larger asymmetry in the fractions of transverse momentum carried by the quarks from the vector boson decay, which results in a higher probability for the pruning algorithm to reject the particles coming from the quark with lower transverse momentum. This leads to the calculation of smaller pruned jet masses than in the case of longitudinally polarised vector bosons. For transversely polarised W bosons the probability of the two quarks being emitted with a relatively large angular separation is larger than in the case of longitudinal polarisation. This leads to a larger fraction of events where the radius parameter of 0.8 is too small for the quarks to be clustered together into one fat jet. Which of those effects is dominant depends on the p_{T} of the produced vector boson. As examined in reference [85] the efficiency for the τ_{21} cut is also lower for transversely polarised vector bosons due to the two effects described above. The remarks in this section are valid for both hadronically decaying W bosons and Z bosons [119].

Figures 6.7 and 6.8 show that the effect of the polarisation is largely independent of the vector boson kinematics. Although a slight dependence on the p_T of the W boson can be seen, this effect is small enough to be negligible compared to the uncertainties on the efficiency fluctuations due to model-dependent kinematics. As an approximation it is sufficient to apply a p_{T} and η independent factors whenever hadronically decaying W bosons or Z bosons are produced with a transversal polarisation. The parametrised efficiencies in appendix B are calculated using a single scale factor to account for effects of vector boson polarisation. The effects of using one polarisation efficiency for all events is smaller than the differences between models. The values of the polarisation scale factors $\epsilon_{trans/long}$ can be found in table 6.3. They are calculated using RS1-Graviton MC samples as

$$\epsilon_{trans/long} = \frac{\sum_{\mathrm{samples}} N_{\mathrm{RS1}}}{\sum_{\mathrm{samples}} N_{\mathrm{BG}}} \ , \tag{6.6}$$

where N_{RS1} is the number of events passing all analysis selections using RS1-Graviton MC samples, and N_{BG} is the number of events passing all analysis selections using Bulk-Graviton MC samples.

6.3.4. Signal Yield Uncertainties

The efficiencies that are calculated and discussed in the previous sections are extracted from Monte Carlo and as such their systematic uncertainties are due to limited Monte Carlo statistics and the uncertainties on the V-tagging scale factors, which were applied to scale the MC events to data. These uncertainties are of the order of 1% and therefore

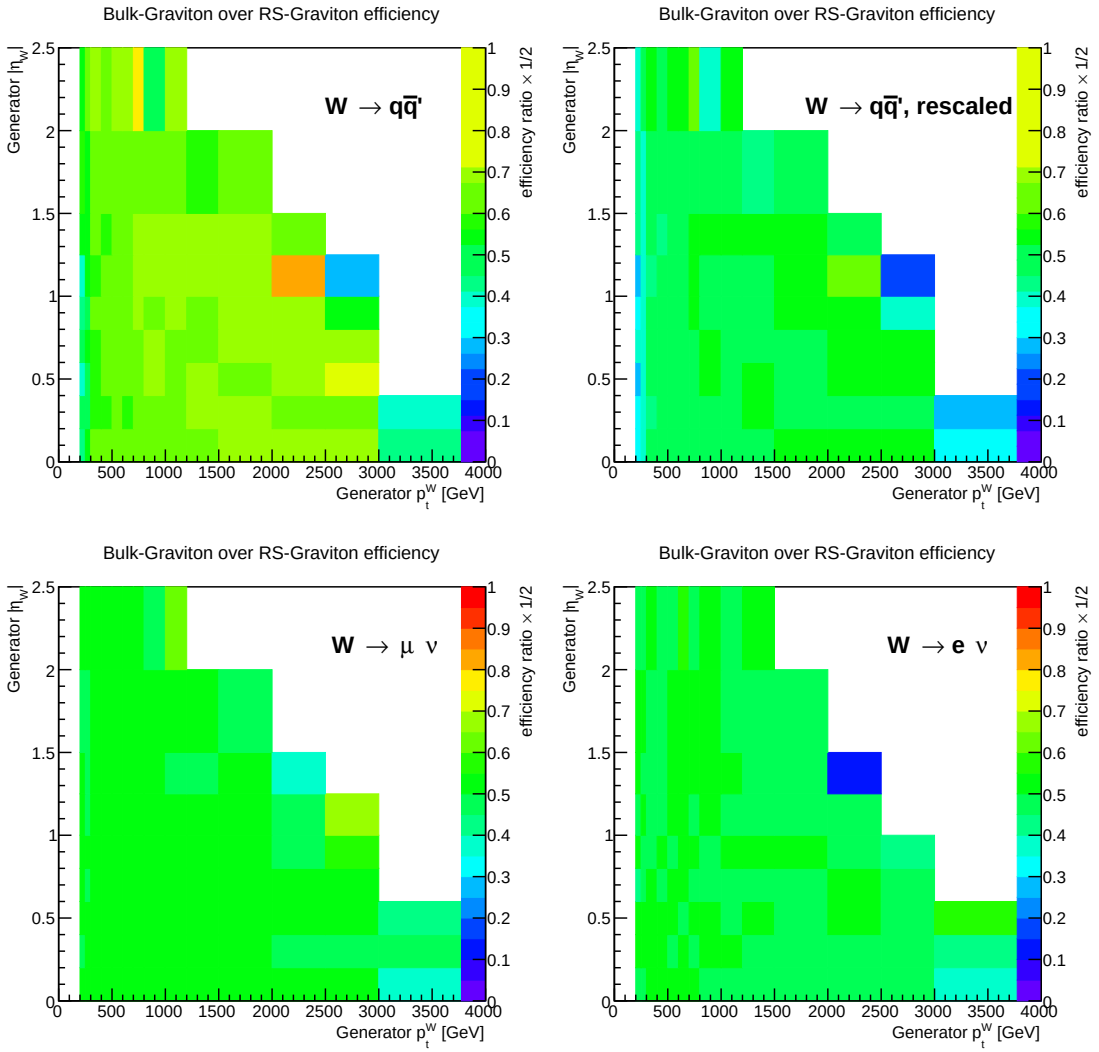

Figure 6.7.: The reconstruction and identification efficiency efficiency for a Bulk-Graviton model divided by the reconstruction and identification efficiency of an RS1-Graviton model, as a function of the generated p_{T} and η of the W boson for the semileptonic analysis. The top left graphic contains the ratio of reconstruction efficiencies for a hadronically decaying W boson. The top right graphic contains the ratio of reconstruction efficiencies for a hadronically decaying W boson, where the Bulk-Graviton sample was rescaled with the polarisation factor of 0.76. On the bottom are the efficiency ratios for a W boson decaying to a muon and neutrino (left) and a W boson decaying to an electron and a neutrino (right).

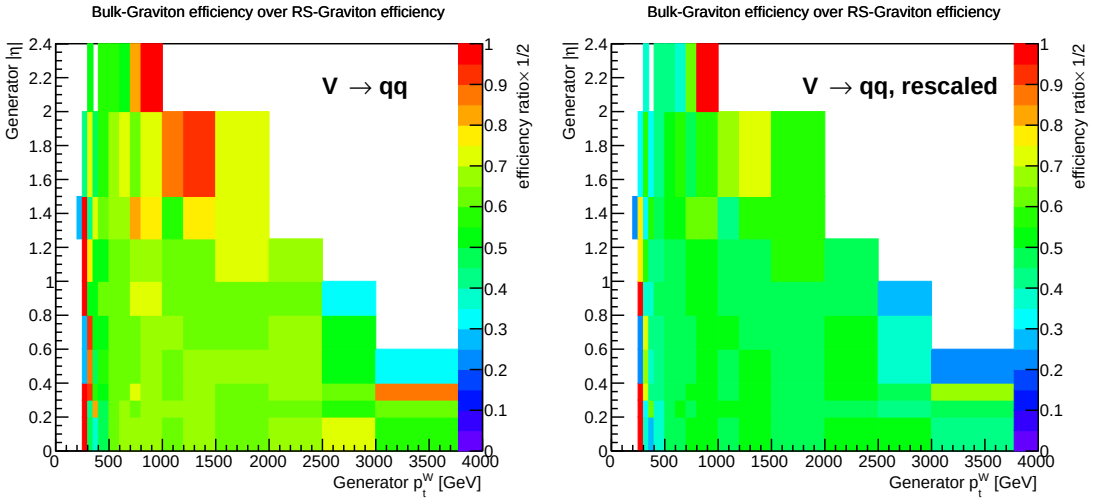

Figure 6.8.: The reconstruction and identification efficiency for a Bulk-Graviton model divided by the reconstruction and identification efficiency of an RS1-Graviton model, as a function of the generated p_{T} and η of the W boson for the all-hadronic analysis. The left histogram contains the same efficiency ratio but the Bulk-Graviton sample was reweighted with the polarisation scale factor of 0.76.

negligible compared to differences in efficiency due to varying distributions of kinematic variables in different theory models. All other uncertainties are already discussed in section 5.6. Since the goal is to calculate limits that are valid for a wide range of theory models, those differences in the reconstruction and identification efficiency have to be included in the limit calculation. They are applied as additional uncertainties on the signal yield. When using this framework one therefore does not have to apply uncertainties in the signal yield calculation. The uncertainties used for the limit calculation are extracted from the tables found in appendix B by comparing the difference between the exact sample efficiency, which is calculated by using all analysis selections on the reconstructed events, with the efficiency obtained by using the recipe described in section 6.6 on different signal models. As final values for the uncertainties found in table 6.4 and 6.5 the largest relative differences for each mass samples is rounded to the nearest multiple of 5. This is a conservative appraisal of the necessary uncertainties to address the remaining imperfections in the parametrisation of efficiencies, but since only a handful of theory models have been tested with this method a conservative estimation is a valid course of action. In section 6.5 for each region in m_{VV} the different uncertainties derived here are added to the uncertainty on the signal yield.

Table 6.4.: Uncertainties of the signal reconstruction efficiencies for limit calculations in the semileptonic WV channel. The uncertainties are taken from the studies in appendix B and rounded up to the nearest multiple of 5.

M_X [GeV]	Uncertainty electron channel	Uncertainty muon channel
800-1200	0.40	0.25
1200-2000	0.25	0.20
2000-3000	0.15	0.10
3000-4000	0.15	0.10
> 4000	0.15	0.10

Table 6.5.: Uncertainties of the signal reconstruction efficiencies for limit calculations in the all-hadronic decay channel. The uncertainties are taken from the studies in appendix B and rounded up to the nearest multiple of 5.

M_X [GeV]	Uncertainty
1200-2000	0.35
2000-3000	0.20
3000-4000	0.25
> 4000	0.20

6.4. Generalisation of Signal Shapes

The resonance searches that are described in chapter 5 are restricted to the narrow-width approximation, where only resonances with a decay-width smaller than the full width half maximum of the detector resolution are considered. In this approximation the resonance shape is fully described by the detector resolution function, which is in principle determined by the energy resolution of the subdetectors involved in the analysis. In the all-hadronic channel a single sided Crystal-Ball function added to a Gauss curve is used to model the signal shape in the m_{VV} mass spectrum. For the semileptonic channel a double-sided Crystal-Ball function is used. There are two slightly different descriptions of the detector resolution, since the in the two final states the detector resolution is driven by different detector components. In the all-hadronic channel the resolution of the HCAL energy measurement plays and important role, but the ECAL energy resolution also contributes due to π^0 decays. Since both analyses use objects with high transverse momenta, the tracker resolution is not important in this case. In the semileptonic channel the ECAL plays an important role for events with a W boson decaying into an electron. For the case where the W boson decays into a muon, the resolution in the muon system is important. Since the semileptonic channel uses MET measurements for the reconstruction of the neutrino, the MET energy resolution also plays a role in this channel. However due to the constrain of the z component of the MET with the W boson mass in the neutrino reconstruction its resolution does not

play a leading role in this analysis but it still warrants the choice of a more asymmetric resolution function than in the all-hadronic channel.

6.4.1. Extension to Broad Signal Shapes

Since the search takes place in the invariant mass spectrum of the expected resonance, all parametrisations of signal shapes refer to the shape of the resonance in this spectrum. To extend the signal shapes to widths larger than the detector resolution, a convolution of S_{narrow}, the detector resolution function and a relativistic Breit-Wigner function (BW)

$$\text{BW}(m) = \frac{N}{(m^2 - M^2)^2 - M^2\Gamma^2} \ , \tag{6.7}$$

is used. Here Γ is the width of the resonance, M its peak mass and N is a normalisation constant. The signal shape for broad resonances thus is

$$S(m_{VV}) = S_{\text{narrow}} \otimes \text{BW} \ . \tag{6.8}$$

It is important to note that with this modelling of signal shapes no new free parameters are introduced. The relativistic Breit-Wigner function depends on the peak of the resonance and its width. The width Γ is not a free parameter but is fixed to the width of the produced MC sample. The peak mass is fixed along with the other free parameters of the detector resolution function by a fit to the narrow-width MC samples of the Bulk-Graviton model. The signal hypothesis for all available models is tested using a χ^2-test between the signal shape function and the histograms in the m_{VV} spectrum filled with events passing the full analysis selections. A confidence level of $\alpha = 0.05$ is used to determine if the probability density function defined by the shape hypothesis has to be rejected. The results of the χ^2-tests can be found in appendix D.

In appendix C the m_{VV} histograms derived from simulation and their corresponding signal shape functions are plotted for different masses, widths and theory models and for both final states. The histograms are filled from reconstructed MC events passing the complete analysis selections, as described in section 5.3. It can be seen that the shape description works well for small masses- except for shifts of the mean value, which are considered in 6.4.2, but breaks down for large resonance masses and widths. A closer examination of this issue can be found in section 6.4.3.

Consequently the signal shapes are modelled as follows for the limit calculation:

- $m_{VV} \leq 2000$ GeV:
  For the semileptonic final states the original signal hypothesis S provides an adequate description and is therefore used in the limit setting procedure. For the all-hadronic channel a shift in the mean value is introduced as described in section 6.4.2.

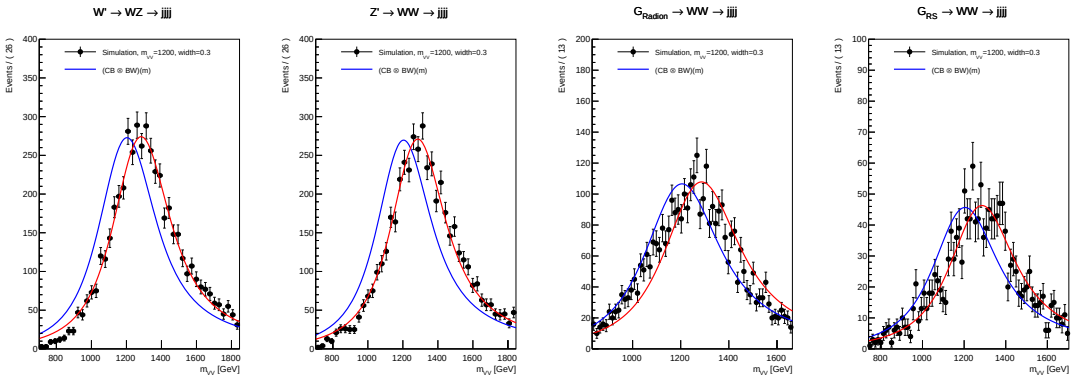

Figure 6.9.: Shape test for the all-hadronic channel and a resonance mass of $m_{VV} = 1200$ GeV for various signal models. The black dots are reconstructed events from MC, the blue curve is the resolution function convoluted with a Breit-Wigner. The red curve is the same functional shape with the mean value shifted as in the limit setting procedure. The MC samples used here have a relative width of $\Gamma/m_{VV} = 0.3$.

- $2000 \leq m_{VV} \leq 2800$ GeV:
  The shapes are accurately described by a convolution between the detector resolution function and a relativistic Breit-Wigner function for all final states considered.

- $M_X > 2800$ GeV:
  The convolution of S_{narrow} and the BW function is multiplied by a Chebyshev polynomial of degree one, with the extra degree of freedom is fixed as described in section 6.4.3.

6.4.2. Peak Mass Shift for $m_X < 2000$ GeV

As can be seen in figure 6.9 and appendix C for small masses the peak mass values for the signal hypothesis are shifted with respect to the prediction from simulation. This shift also exists in the semileptonic channel, but is small enough to be fully contained inside uncertainties assigned to the peak mass value from the fit of the detector resolution function. In the all-hadronic channel, however, a shift for resonance masses smaller than 2000 GeV is introduced. These shifts in the peak value of the m_{VV} distribution originate in the residual p_{T} dependence of the jet energy scale and resolution.

The necessary shift is determined through fits for all available masses, widths and theory models. For use in the limit calculation the resulting shifts are interpolated linearly

between mass points for all widths, with the shift in the narrow-width case being zero. Between those resulting points a second linear interpolation between the widths is used to get the final value for the shifted mass peak m_S. This is done for all theory models for which simulated samples are available. The value for the shift m_S is then averaged over all signal models, taking the difference between maximum and minimum of the observed shifts for all theory models as additional uncertainty on the parameter. The resulting uncertainty is much larger than those originating from the fit. The signal function resulting from this procedure (red curve) can be seen in figure 6.9 overlaid over the histograms filled with reconstructed events from the simulation for different signal models. As can be seen the resulting shift shows good agreement for all used theory models, and it is a clear improvement from the previous signal shape without mean shift (blue curve).

6.4.3. PDF Correction for $m_X \geq 2800$ GeV

For high masses and widths the signal shapes display an excess of contributions from small masses with respect to the expectation from the signal shape modelling, as can be seen in figure 6.10 and in appendix C. The reason for this behaviour is that those resonances are spread over a large spectrum of energies and thus partons with different energy fractions are involved in the production. This leads to an evaluation of the particle density function of the partons over a larger range in the energy spectrum as opposed to a narrow resonance. Due to the increase of the value of PDFs for smaller momentum fractions an increase in contributions from smaller resonance mass values can be seen. This effect of the PDFs on the shape of the resonance is significant for large masses and widths while it plays no role for resonance masses smaller than 2 TeV. In the case of Drell-Yan processes this effect can be corrected for the whole range of the analysis by introducing an extra degree of freedom in the form of a Chebyshev polynomial of degree one, see figure 6.10. In the case of gluon fusion processes the effect is stronger and cannot be corrected for all masses and widths in the range of the analysis. In figure 6.11 the difference in signal shapes between quark-anti-quark annihilation and gluon fusion production can be seen. Since for some simulated samples for large resonance masses the introduction of the extra degree of freedom for gluon fusion does not lead to a valid description of the expected signal shape, a shaded area is introduced in the final limits to indicate the region where the limits are not valid for gluon fusion produced models.

The determination of the value of the new fit parameter a_0 for the Chebyshev polynomial is analogous to the method of determining the mean shift described in section 6.4.2, with two exceptions. For the fits and interpolation only the models with more than 80% Drell-Yan production are used, effectively excluding the Radion model. This is a sensible choice since the introduction of the Chebyshev polynomial is not enough to fully describe the shapes extracted from simulation in this case. The second difference is that instead of introducing a mass cut from which the new signal model is used, this mass is determined

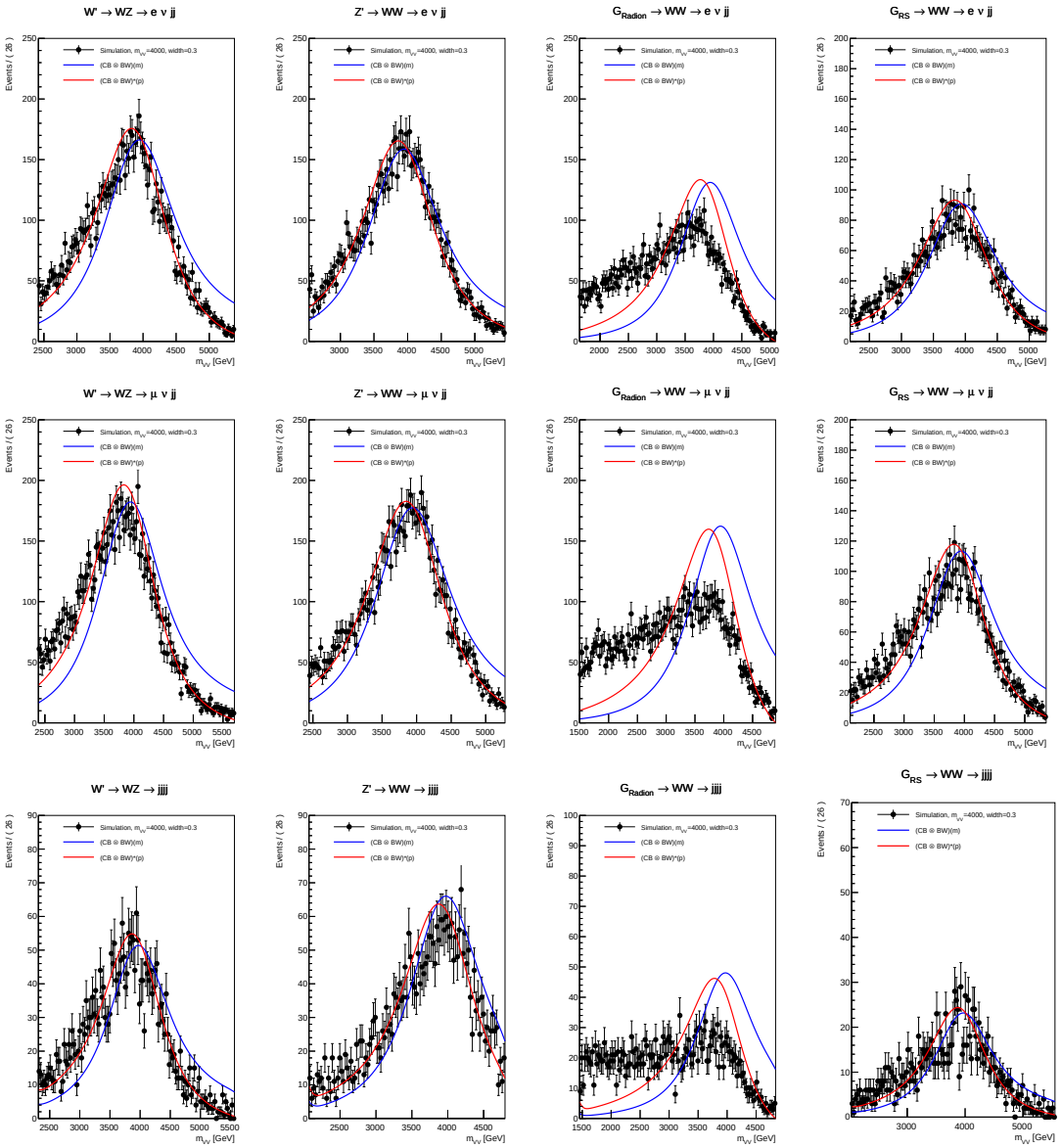

Figure 6.10.: Shape test for a mass $m_{VV} = 4$ TeV and a relative width of $\Gamma/m_{VV} = 0.3$ for different theory models. The reconstructed events from MC prediction are drawn as black dots, the blue line is the signal shape model consisting of the narrow shape convoluted with a Breit-Wigner function. The red line is the signal shape model multiplied with a Chebyshev polynomial of degree one that is fitted to the histogram. A Chebyshev polynomial was chosen because of its well defined normalisation properties. The interval in m_{VV} is chosen to contain about 90% of signal events. In the top are the shape tests for the electron channel, while the shape tests for the muon channel are in the middle. On the bottom are the shape tests for the all-hadronic analysis.

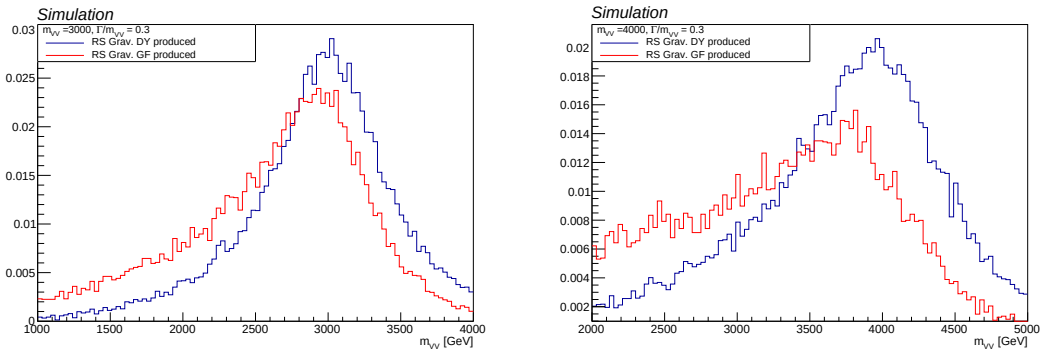

Figure 6.11.: The normalised generated m_{VV} spectra for an RS1-Graviton model, separated based on the production mechanism. The red histogram contains events from gluon fusion (GF) and the blue one from Drell-Yan (DY) production. On the left a simulated sample with a resonance mass of 3 TeV and a relative width Γ/m_{VV} of 0.3 is considered while the right plot is made with a simulated sample of a resonance mass of 4 TeV and a relative width of Γ/m_{VV} of 0.3.

for each width dynamically by using the extra degree of freedom until the interpolation leads to a change in sign of a_0, thus taking corrections for smaller resonance masses into account for which no samples where simulated. This leads to the use of the extra degree of freedom to a mass of 2800 GeV for the largest widths of 0.3.

The signal function resulting from this procedure (red curve) can be seen in figure 6.12 overlaid over the histograms filled with simulated events passing all analysis selections for different signal models, produced widths and resonance masses. Except for masses above 4000 GeV and a mass of 3000 GeV with a width larger than 0.3 in the Radion model the resulting agreement between MC prediction and signal shape hypothesis is acceptable, as can be seen in the tables shown in appendix D.

6.5. Calculation of Model-Independent Limits

The limits are calculated with the asymptotic CLs method (see chapter 4) with the Combine framework [112], using all systematic uncertainties of the main analysis and adding the uncertainties calculated in section 6.3, and listed in table 6.4 and table 6.5, as efficiency uncertainties on the event yield. The limits are calculated for a 2D grid spanned by the signal widths and masses. The calculation is done for relative widths between the narrow-width approximation and 0.3 in regular intervals of 0.05 and for masses between 800 (1200) GeV and 4500 (4000) GeV in intervals of 100 GeV for the semileptonic (all-

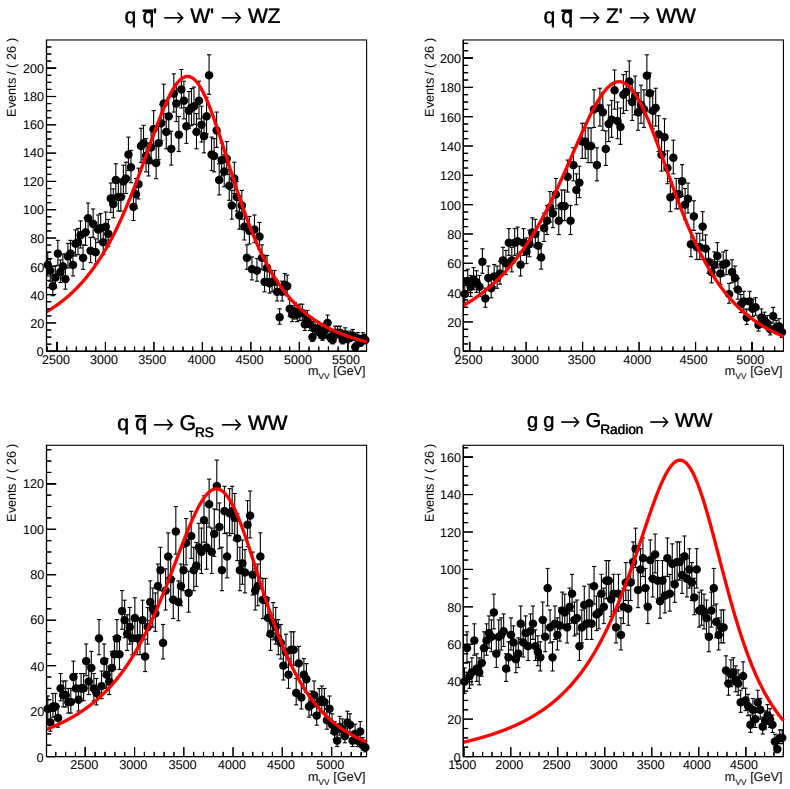

Figure 6.12.: The signal shape and MC prediction of the m_{VV} spectrum plotted for different models. The black dots are reconstructed MC events and the red curve is the final signal function. The interval in m_{VV} is chosen to contain 90% of signal events. As an example the comparison is given for a mass point of $m_{VV} = 4$ TeV and a relative width of $\Gamma/m_{VV} = 0.3$ for the muon channel of the semileptonic analysis.

hadronic) channel. The signal shapes are modelled as described in section 6.4 with a shaded area added to indicate the region in which the limits cannot be applied to models with gluon fusion as primary production mechanism. To calculate limits for resonances with a mass different from those produced as Monte-Carlo samples, the signal shapes are interpolated. The two final states use different procedures for the interpolation and the limit setting procedure; see section 6.5.1 for the semileptonic channel and 6.5.2 for the hadronic channel. The limits are given on the number of signal events to avoid the model-dependence on the cross sections.

The limits given in figures 6.14 and 6.15 have the following meaning:

The expected limits represent the numbers of signal events necessary in order to reject an exotic signal model with a 95% level of confidence. The expected limits are determined by the power of the analysis to distinguish between background and signal events and therefore also by the uncertainty on the numbers of background and expected signal events. These limits are determined without using CMS measurements of the signal region.

The observed limits represent the number of signal events that are necessary in order to reject an exotic signal model with a confidence level of 95%, given the actual measured data. The fluctuations in the exclusion power are due to statistical fluctuations in data. For very high masses, where the background estimation is almost zero, the exclusion power is essentially limited by Poisson statistics of the data. The tables in appendix E contain the results of the limit calculation.

6.5.1. Results for the Semileptonic Channel

The semileptonic channel uses an unbinned shape analysis with a fixed background estimation, see section 5.5. For the limit setting procedure the signal shapes are calculated for arbitrary mass points by using a linear interpolation between the fit values of the double-sided Crystal-Ball function for different simulated mass points. For broad signal models the shape modelling described in section 6.4 is used together with the interpolation between mass points for narrow resonances. A shape test of this procedure is shown in figure 6.13. The normalisation of the signal shapes is fixed to the expected event yields of the narrow-width Bulk-Graviton model, the signal yield for the limit calculation is extracted from this as integral over the shape function over the range $m_{VV} \in [700, 5000]$, thus taking into account that more events fall out of the analysis acceptance if the width of the signal increases. The signal efficiency uncertainties found in table 6.4 are added as uncertainties on the signal yield.

The expected and observed limits for the semileptonic final states are shown in figure 6.14. The corresponding values for $N_{expected}$ can also be looked up in the tables in appendix

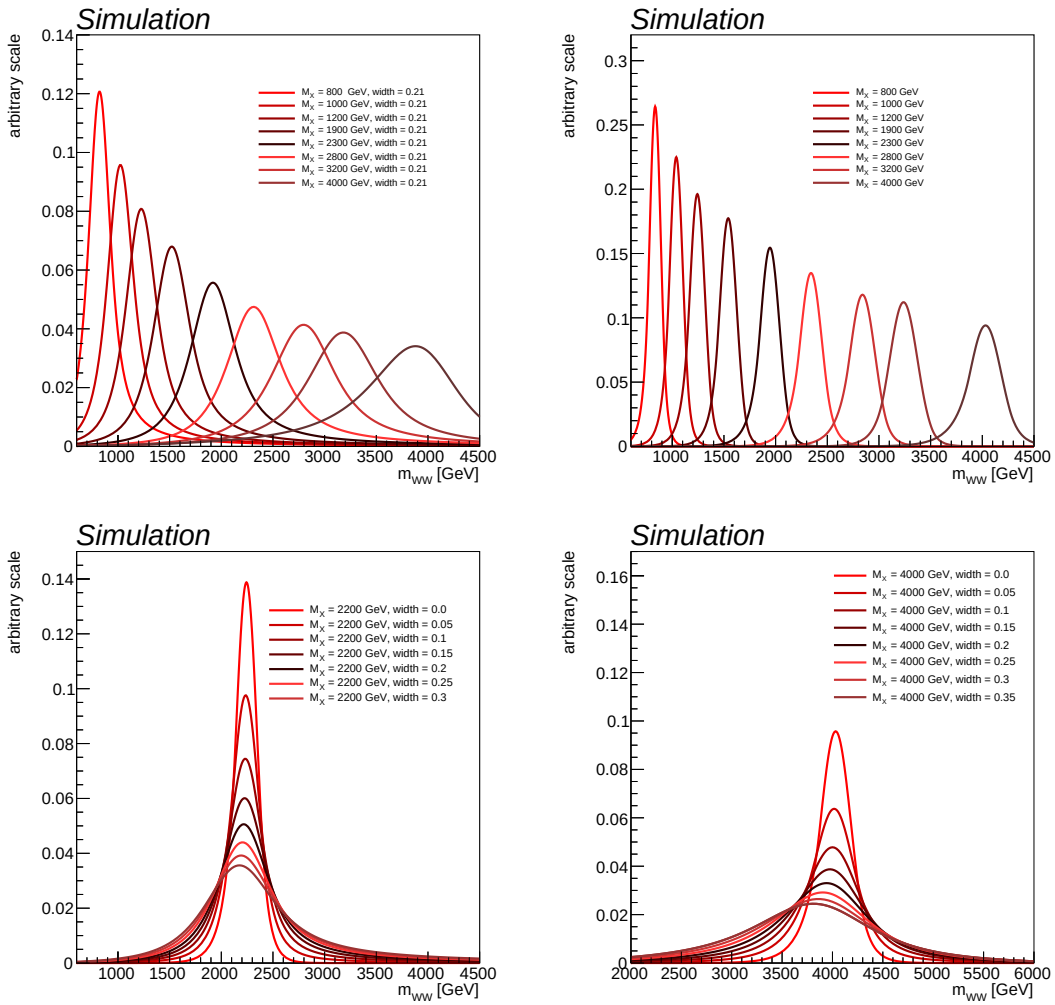

Figure 6.13.: A shape test for the interpolation procedure of the semileptonic analysis. The top left figure shows the signal shapes normalised to unity for different masses and a fixed width of $\Gamma/m_{VV} = 0.21$. The top right plot shows the same for the narrow-width approximation. On the bottom left are the signal shapes for a fixed mass of $m_{VV} = 2200$ GeV and different widths and on the bottom right are the shapes for $m_{VV} = 4000$ GeV and different widths featuring the interpolation of the extra degree of freedom. As an example the figures are given for the muon channel only. The functional forms of the detector resolution were extracted from simulated samples for the mass points of $m_{VV} = 800$, 1200 and 4000 GeV.

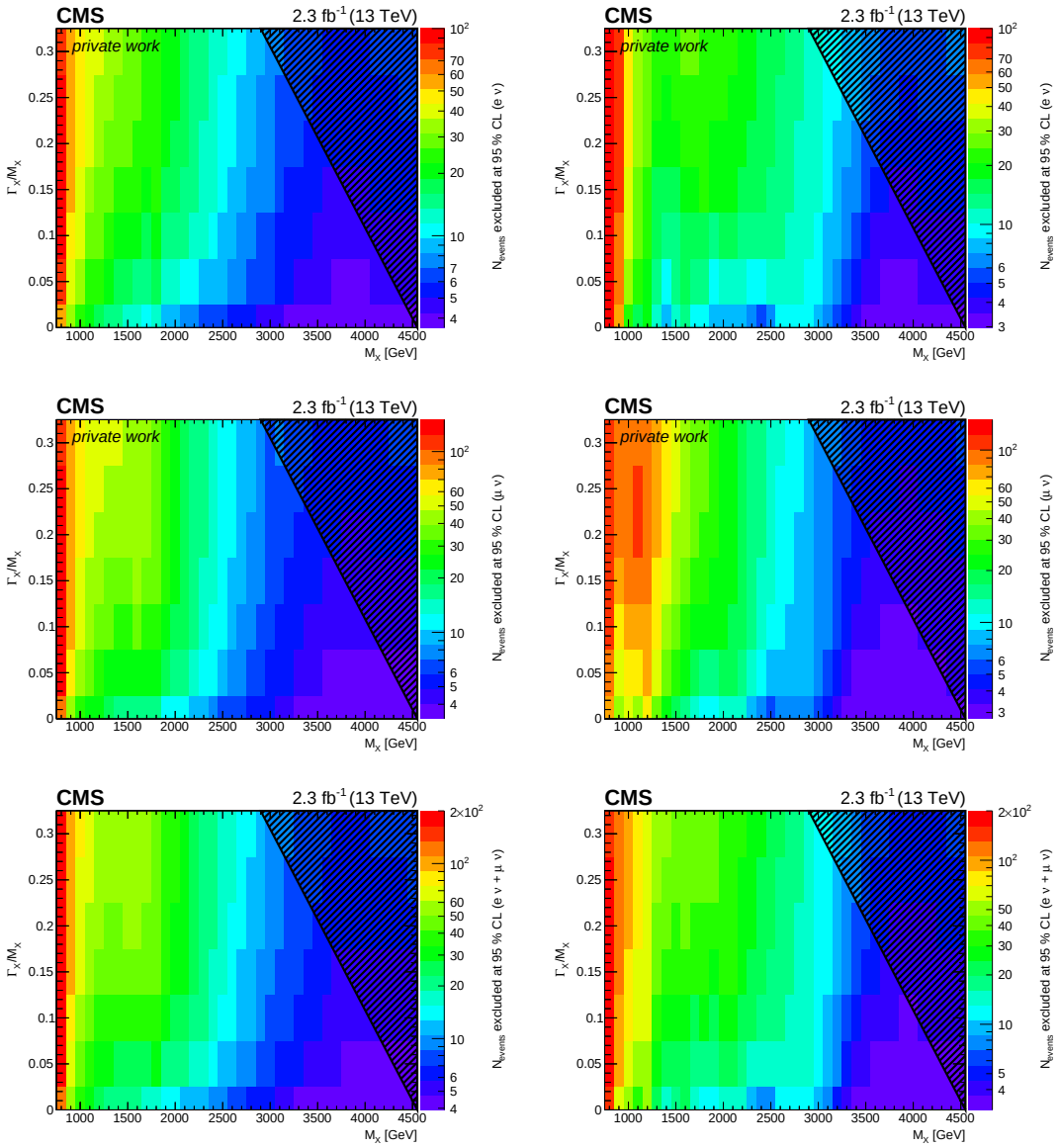

Figure 6.14.: The expected and observed exclusion limits on the number of events for the semileptonic channel, as a function of resonance mass and the relative width of the resonance. On the left hand side are the expected limits, and on the right side are the observed limits. At the top are the limits for the electron channel, in the middle are the limits for the muon channel and on the bottom are the limits for both lepton channels combined. The shaded area indicates the region where the shape hypothesis breaks down for gluon fusion processes.

E. The observed limits are contained within the 1 σ uncertainty band of the expected limits, see figure E.1 in appendix E.

6.5.2. Results for the All-Hadronic Channel

For the shape interpolation in the all-hadronic channel a different method is used. Instead of interpolating the fit values for the narrow-shape function, the analysis uses histograms with 1 GeV bin width of the m_{VV} spectrum derived from the MC samples. Histograms for each mass point are calculated bin per bin using a cubic spline interpolation between the bin contents for each produced mass point. The resulting histograms are used to fit the narrow-signal function directly. The normalisation and signal yield are fixed in the same way as in the semileptonic case. The signal efficiency uncertainties found in table 6.5 are added as uncertainties on the signal yield.

The expected and observed limits for the all-hadronic final states are in figure 6.15. The corresponding values for the number of signal events $N_{expected/observed}$ can be looked up in the tables in appendix E. Since the all-hadronic analysis does not perform the background estimation through a fit in a mass sideband, the background function is fitted simultaneously with the signal function. In the region between 1400 GeV $\leq m_{VV} \leq$ 1800 GeV this leads to a worsening of the exclusion limits for broad resonances due to the possibility that a local decrease in the background function can be compensated by events from a broad signal. The observed limits are contained within the 1 σ uncertainty of the expected limits, with the exception of one point in the mass-width plane, that is, however, well within the 2 σ uncertainty band. This can be seen in figure E.1 in appendix E.

6.6. Instructions for the Usage of the Model-Independent Results

To compare a specific model to the model-independent limits given in section 6.5 the following instructions should be followed step by step. First MC samples of the theory model in question have to be generated. It is important to note that it is not necessary to start a full production, since for this framework only the generator kinematics of the produced particles are used. Thus it suffices to produce MC samples on matrix element level only. In the semileptonic channel the τ decay to leptons has to be included in the production in order to correctly reproduce the analysis acceptance. It is possible to produce events with leptonically decaying tauons only as long as these events are weighted by the τ branching ratio to leptons. Using the following procedure these MC

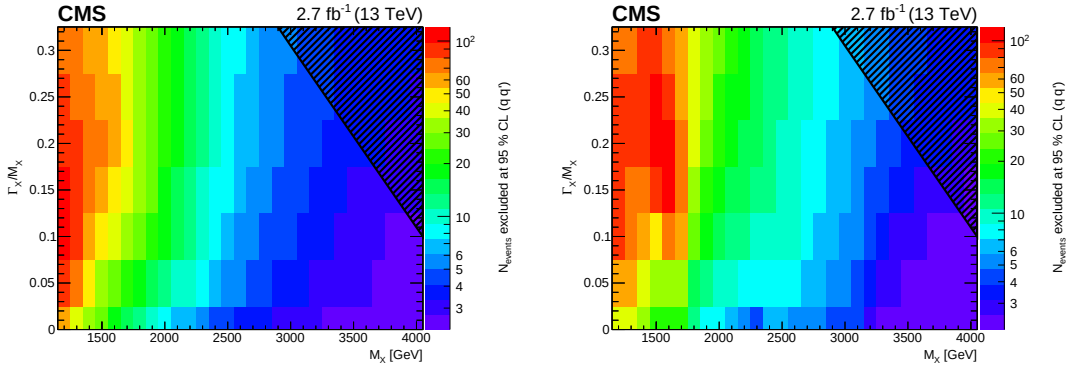

Figure 6.15.: The 95%CL exclusion limits on the number of events for the production of an exotic diboson resonance, in the all-hadronic channel, as a function of the exotic resonance mass. On the left are the expected limits and on the right the observed limits. The shaded area indicates the region where the shape hypothesis breaks down for gluon fusion processes.

samples are used to extract the product of the acceptance and reconstruction efficiency of the analyses for a generic signal model.

1. The signal events need to be preselected using the generator level selections in table 6.1 or 6.2 depending on whether the semileptonic or hadronic final state is considered.

2. The events need to be reweighted with the efficiencies given in table A.1, A.2 and A.3 in the appendix in the case of a semileptonic decay.

   - A reweighting according to the identification and reconstruction efficiency of a leptonic W boson with the given kinematics should be applied, using table A.1 or A.2.

   - A second reweighting of the event according to the identification and reconstruction efficiency of a hadronic W or Z boson using table A.3 or A.4 should be applied. If the hadronic vector boson is transversally polarised the efficiency should be multiplied by a correction factor that is listed in table 6.3.

3. In case of a hadronic decay the events have to be reweighted according to the efficiencies in table A.5.

4. The efficiencies for the second lepton veto and b-tagged jet veto should be applied for the semileptonic final state. The exact values for these vetoes are listed in table 6.3. In case of the all-hadronic channel a factor of 98% should be applied to account

for the selection efficiency on $\Delta\eta_{jj}$.

5. The resulting sum of weights divided by the number of signal events generated provides a reasonable approximation of the product of the total signal efficiency and acceptance for the given model.

The code written for this thesis, which can be found in `https://github.com/daniSchaefer/lheToTree`, can be used to apply the procedure described above to an LHE [120] event file of a generic model. Once ϵ, the acceptance multiplied by the efficiency for the model, is calculated the number of expected signal events N can be compared to the limits given in section 6.5 for a particular resonance mass and width. The number of expected signal events is calculated as

$$N = \sigma_{prod}(\sqrt{s} = 13 \text{ TeV}) BR_{(X \to VV)} BR_{(VV \to \text{final state})} L\epsilon \ , \tag{6.9}$$

where L denotes the integrated luminosity, $\sigma_{prod}(\sqrt{s} = 13 \text{ TeV})$ is the production cross section for the production of a resonance X at a center of mass energy of 13 TeV at the LHC, $BR_{(X \to VV)}$ is the branching ratio of the exotic resonance to two vector bosons, and $BR_{(VV \to \text{final state})}$ is the branching ratio of the produced vector bosons to the final state of the analyses.

6.7. Limits on an RS1-Graviton Model

The exclusion bounds for an RS1-Graviton model are calculated within the framework this thesis provides as a proof of concept. The RS1-Graviton model is chosen because of its large production cross section at the LHC, see section 1.2. This model is usually not used in dedicated analyses in the diboson channel since the diphoton channel has a larger sensitivity for this model, thus the exclusion region provided here is the first for the diboson channel.

For this test a series of Monte Carlo samples are produced with MADGRAPH5 [100]. The τ decay for the semileptonic channel is included using the package TAUDECAY [103]. Only decays of the τ to the semileptonic final states were explicitly modelled. To take the decay modes into account that are not used by the analysis, each event with a W decaying to $\tau\nu$ is weighted according to the branching ratio of τ to an electron and neutrinos or to a muon and neutrinos. Starting from the LHE event format the steps to calculate the analysis efficiency described in section 6.6 are implemented in the code found in `https://github.com/daniSchaefer/lheToTree`. This code has been provided as part of this thesis and can be used to reweight samples with WW and WZ as intermediate states for the semileptonic channel, and WW, WZ and ZZ intermediate states for the all-hadronic channel.

For each sample the acceptance×efficiency (ϵ) is extracted for the usage in the calculation of the expected signal event yield. The number of signal events N within the analyses acceptance and reconstruction efficiencies is then calculated as

$$N = \sigma_{\text{production}} \cdot L \cdot \epsilon \cdot \text{BR}_{\text{G} \rightarrow \text{WW/ZZ}} \cdot \text{BR}_{\text{final state}} \ . \tag{6.10}$$

Here L is the integrated luminosity, $\sigma_{\text{production}}$ is the production cross section at the LHC and a center of mass energy of 13 TeV, $\text{BR}_{\text{G to WW/ZZ}}$ is the branching ratio of the exotic particle to the diboson intermediate state and $\text{BR}_{\text{final state}}$ is the branching ratio of the produced bosons to the final state of the analysis. The theory cross section is adapted to different values of the width and therefore the coupling $\tilde{\text{k}}$ using

$$\sigma(m_G, \tilde{k}) = \left(\frac{\tilde{k}}{0.1}\right)^2 \cdot \sigma(m_G, 0.1) \ . \tag{6.11}$$

The values for $\sigma(m_G, 0.1)$ are found in reference [121], together with the branching ratio of an RS1-Graviton to two vector bosons. The branching ratios of the vector bosons into the final state particles of the analysis are calculated as

$$\text{BR} = \begin{cases} (\text{BR}_{\text{W to e}\nu} + \text{BR}_{\text{W to }\mu\nu} & \\ +\text{BR}_{\text{W to }\tau\nu} \cdot \text{BR}_{\tau \text{ to l}\nu\nu}) \cdot 2 \cdot \text{BR}_{\text{G to WW}} & \text{, for WW to lvqq} \\ \text{BR}_{\text{G to WW}} \cdot (\text{BR}_{\text{W to qq}})^2 & \text{, for WW to qqqq} \\ \text{BR}_{\text{G to ZZ}} \cdot (\text{BR}_{\text{Z to qq}})^2 & \text{, for ZZ to qqqq} \end{cases} , \tag{6.12}$$

using the branching ratios in reference [118]. The analysis acceptance×efficiency ϵ is calculated separately for the all-hadronic decay channel and the semileptonic decay channel, as well as for the intermediate states WW and ZZ for the all-hadronic decay channel.

Figure 6.16 shows the observed 95% CLs limits on the number of observable events overlaid with an exclusion curve (light blue), which marks the crossing point of the observed CLs limit with the theory prediction. The exclusion power of the two considered final states is similar, excluding RS1-Graviton resonances with masses smaller than ≈ 2 TeV for coupling strengths $\tilde{\text{k}}$ between 0.07 and 0.4. A dedicated analysis done specifically for the RS1-Graviton model could reach better exclusion bounds, but this framework is able to produce limits over a wide range of coupling strengths. Dedicated RS1-Graviton analyses are not usually done for this decay channel since the decay to two photons is more sensitive. Since with the framework presented in this thesis it is possible to find exclusion regions for arbitrary theory models, the RS1-Graviton model is suitable for this proof of concept, since the exclusion region calculated in this model-independent way is the first given in the diboson channel for this model, but the success of the exclusion region can still be compared to bounds given by dedicated analysis. Exclusion bounds for an RS1-Graviton model in the diphoton decay channel can be found for example in references [2] and [3]. Compared to these bounds, which were calculated in the diphoton channel and for a center-of-mass energy of 13 TeV and 8 TeV combined, the limits on an

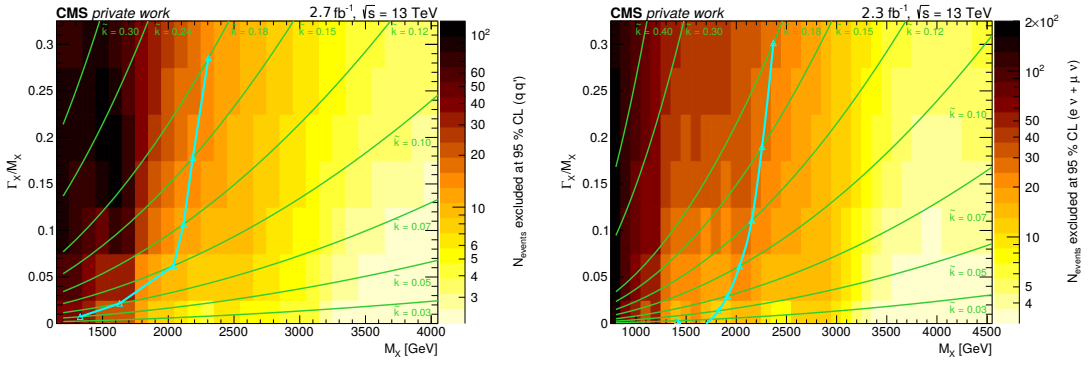

Figure 6.16.: Exclusion bounds for the RS1-Graviton model in both the the all-hadronic channel (left) and semileptonic decay channel (right). The green lines indicate the widths and masses corresponding to a certain coupling $\tilde{k}$. The parameter space to the left of the blue line, which marks the crossing point of the theory prediction with the observed limits, is excluded.

RS1-Graviton model given in this thesis are about a factor of 2 worse. This is a good performance given that the framework used for the calculation of these exclusion bounds is especially designed to be model-independent and the diboson channel is less sensitive to this particular theory model.

7. Conclusion

There are a multitude of theory models predicting diboson resonances. Since the predictions for kinematic distributions of final state particles, cross sections and branching ratios vary wildly between different models, it is impossible for experimentalists to give conclusive bounds for all of them. In practice a few selected theory models are used for most BSM analysis, which are not chosen by their physical merit alone, but also considering reasons like availability of MC generators. Thus more sophisticated or less known models are often disregarded by dedicated analyses of experimental data searching for BSM physics.

The goal of this thesis is to bridge the gap between theorists and experimentalists by providing a framework and model-independent limits for diboson resonances, that can be used to set limits on arbitrary theory models. This thesis is an expansion of two existing CMS diboson searches, which utilise jet substructure techniques to search for heavy diboson resonances in the mass range from 800 to 4000 TeV, with data taken with the CMS detector at $\sqrt{s} = 13$ TeV. The considered analyses are optimised for the search of resonances arising in the Bulk-Graviton or HVT models. Two different final states are considered, the semileptonic channel, where the resonance decays to one W boson, which in turn decays leptonically and one vector boson that decays hadronically. The second channel considered is the all hadronic channel, where both vector bosons decay hadronically.

Based on references [113] and [114] the model-independent limits were calculated for a 2D grid of different values for the mass m_X and relative decay width Γ/m_X of the exotic resonance. In order to achieve model-independence the limits are given on the number of signal events, the low purity category of the analyses was dropped, and the W and Z mass windows combined into one category. The limit calculation also takes an additional set of systematic uncertainties on the signal yields into account, which are based on differences in the reconstruction and identification efficiencies of the two vector bosons between different theory models.

In figure 7 the results for the two-dimensional model-independent limits are given. Together with the upper limits on the number of signal events, tables containing the reconstruction and identification efficiencies for vector bosons in the kinematic acceptance of the analysis are provided. Following the instructions detailed in 6.1 or using the code and instructions under the address `https://github.com/daniSchaefer/lheToTree` it

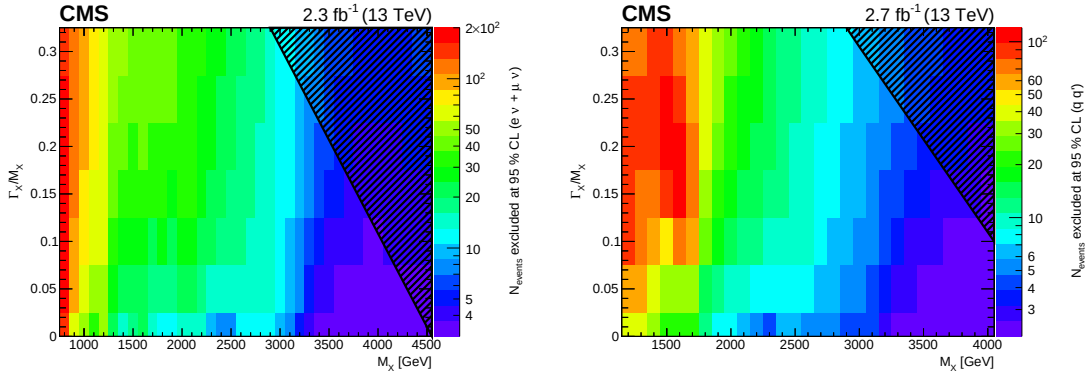

Figure 7.1.: Model-independent 95% CL limits on the number of observed signal events. The limits are given as a function of the resonance mass m_X and the relative width of the resonance Γ/m_X. On the left are the limits for the semileptonic final state and on the right are the limits for the all hadronic final state. The shaded area denotes the kinematic regime where the limit is valid only for quark-anti-quark annihilation processes.

is possible to estimate the number of events for a generic signal model, that would be expected to be detected in CMS with the collected integrated luminosity and to compare it with the upper limit on the number of signal events.

As a proof of concept, limits on an RS1-Graviton model are calculated using the provided framework. The limits can be found in 6.16 and provide an exclusion region for resonance masses smaller than 2 TeV and couplings $\tilde{k}$ larger than 0.07 and 0.3 in both channels. The exclusion bounds provided by this model-independent framework are worse than those from a dedicated analysis such as [3], however, the limits provided with this framework are provided over a larger parameter space in coupling strengths.

To summarise: Model-independent limits on diboson resonances with a semileptonic or hadronic final state were calculated and used to develop an ready-to-use framework for the calculation of signal yields from arbitrary theoretical models. This enables model-builders to directly obtain the phenomenological implications of their theories and can therefore help to stimulate and improve scientific exchange between the theoretical and experimental communities.

List of Figures

List of Tables

Appendices

A. Parametrised ID and Reconstruction Efficiencies

The efficiencies contained in this section are calculated as described in section 6.3. For the calculation of the efficiencies of the leptonically decaying W boson and of the hadronically decaying W boson in the semileptonic channel a set of Bulk-Graviton samples is used. The efficiency for a hadronically decaying Z boson in the semileptonic channel is calculated using a set of W′ MC samples. For the all-hadronic channel MC samples of a Radion decaying into two Z bosons are used for the calculation of the efficiencies for a hadronically decaying Z boson. For the calculation of reconstruction efficiencies of a hadronically decaying W boson a set of Bulk-Graviton MC samples is used. All MC samples used in this calculation were generated in the narrow-width approximation.

Table A.1.: Reconstruction and identification efficiencies for $W \to \mu\nu$ and $W \to \tau\nu \to \mu\nu\nu\nu$ as a function of the generated transverse momentum and pseudorapidity.

p_T [GeV]	$\lvert\eta\rvert$ range								
	0-0.2	0.2-0.4	0.4-0.6	0.6-0.8	0.8-1.0	1-1.25	1.25-1.5	1.5-2.0	2-2.5
200-250	0.82	0.79	0.79	0.80	0.85	0.82	0.81	0.82	0.78
250-300	0.89	0.90	0.88	0.86	0.90	0.86	0.91	0.86	0.91
300-400	0.90	0.89	0.90	0.90	0.89	0.90	0.89	0.90	0.87
400-500	0.88	0.89	0.91	0.90	0.88	0.89	0.90	0.89	0.89
500-600	0.90	0.90	0.92	0.90	0.88	0.89	0.91	0.87	0.88
600-700	0.91	0.90	0.92	0.91	0.88	0.90	0.92	0.88	0.87
700-800	0.91	0.89	0.92	0.91	0.89	0.89	0.91	0.90	0.82
800-1000	0.92	0.89	0.92	0.91	0.88	0.88	0.90	0.88	0.94
1000-1200	0.91	0.89	0.92	0.91	0.89	0.88	0.89	0.85	0.75
1200-1500	0.91	0.88	0.92	0.91	0.87	0.87	0.89	0.87	-
1500-2000	0.90	0.87	0.92	0.91	0.86	0.88	0.87	-	-
2000-2500	0.91	0.86	0.91	0.90	0.83	0.82	-	-	-
2500-3000	0.88	0.79	0.90	0.82	-	-	-	-	-
3000-4000	0.78	0.88	0.80	1.00	-	-	-	-	-

Table A.2.: Reconstruction and identification efficiencies for W $\rightarrow e\nu$ and W $\rightarrow \tau\nu \rightarrow e\nu\nu\nu$ as a function of the generated transverse momentum and pseudorapidity.

p_T [GeV]	$\lvert\eta\rvert$ range								
	0-0.2	0.2-0.4	0.4-0.6	0.6-0.8	0.8-1.0	1-1.25	1.25-1.5	1.5-2.0	2-2.5
200-250	0.78	0.75	0.82	0.81	0.79	0.80	0.71	0.79	0.68
250-300	0.79	0.79	0.77	0.80	0.78	0.82	0.79	0.73	0.78
300-400	0.82	0.82	0.82	0.83	0.82	0.82	0.80	0.81	0.80
400-500	0.82	0.82	0.81	0.84	0.81	0.81	0.82	0.82	0.80
500-600	0.83	0.83	0.84	0.84	0.83	0.81	0.82	0.84	0.85
600-700	0.83	0.84	0.84	0.83	0.85	0.84	0.82	0.84	0.88
700-800	0.84	0.83	0.84	0.85	0.84	0.84	0.82	0.82	0.94
800-1000	0.83	0.84	0.84	0.84	0.85	0.86	0.82	0.85	0.78
1000-1200	0.83	0.84	0.84	0.83	0.84	0.85	0.84	0.86	0.33
1200-1500	0.84	0.84	0.84	0.84	0.85	0.84	0.85	0.81	-
1500-2000	0.83	0.85	0.84	0.84	0.86	0.84	0.86	0.95	-
2000-2500	0.83	0.85	0.84	0.85	0.84	0.79	-	-	-
2500-3000	0.78	0.82	0.78	0.69	-	-	-	-	-
3000-4000	0.80	0.81	0.67	1.00	-	-	-	-	-

Table A.3.: Reconstruction and identification efficiency of W $\rightarrow q\bar{q}'$ using the selections of the semileptonic analysis.

p_T [GeV]	$\lvert\eta\rvert$ range								
	0-0.2	0.2-0.4	0.4-0.6	0.6-0.8	0.8-1.0	1.0-1.25	1.25-1.5	1.5-2.0	2.0-2.5
200-250	0.27	0.34	0.23	0.25	0.35	0.32	0.31	0.30	0.32
250-300	0.55	0.50	0.55	0.51	0.54	0.58	0.52	0.56	0.54
300-400	0.74	0.74	0.75	0.73	0.73	0.69	0.69	0.67	0.63
400-500	0.69	0.68	0.70	0.69	0.68	0.69	0.65	0.65	0.71
500-600	0.72	0.72	0.74	0.73	0.74	0.70	0.66	0.70	0.75
600-700	0.74	0.75	0.75	0.74	0.73	0.72	0.71	0.73	0.78
700-800	0.74	0.75	0.74	0.75	0.73	0.72	0.68	0.69	0.66
800-1000	0.74	0.75	0.75	0.75	0.73	0.71	0.66	0.66	0.58
1000-1200	0.70	0.71	0.72	0.72	0.69	0.67	0.59	0.63	0.40
1200-1500	0.69	0.70	0.70	0.70	0.68	0.65	0.54	0.59	-
1500-2000	0.68	0.69	0.68	0.68	0.67	0.65	0.47	-	-
2000-2500	0.69	0.69	0.69	0.69	0.67	0.69	-	-	-
2500-3000	0.74	0.66	0.73	0.60	-	-	-	-	-
3000-4000	0.74	0.74	-	-	-	-	-	-	-

Table A.4.: Reconstruction and identification efficiency of $Z \to q\bar{q}$ using the selections of the semileptonic analysis.

p_T [GeV]	$\|\eta\|$ range								
	0-0.2	0.2-0.4	0.4-0.6	0.6-0.8	0.8-1	1.0-1.25	1.25-1.5	1.5-2	2.0-2.5
200-250	0.26	0.48	0.27	0.37	0.33	0.41	0.37	0.36	0.28
250-300	0.64	0.56	0.62	0.58	0.60	0.57	0.56	0.61	0.53
300-400	0.76	0.75	0.77	0.75	0.74	0.72	0.71	0.73	0.67
400-500	0.75	0.75	0.76	0.74	0.76	0.77	0.73	0.74	0.71
500-600	0.80	0.81	0.82	0.80	0.78	0.79	0.76	0.78	0.73
600-700	0.81	0.83	0.80	0.81	0.82	0.80	0.76	0.77	0.72
700-800	0.81	0.80	0.79	0.79	0.80	0.78	0.74	0.75	0.77
800-1000	0.81	0.81	0.81	0.81	0.79	0.77	0.72	0.74	0.72
1000-1200	0.78	0.78	0.79	0.78	0.77	0.75	0.66	0.71	0.77
1200-1500	0.77	0.77	0.76	0.77	0.75	0.73	0.60	0.65	0.66
1500-2000	0.74	0.74	0.73	0.74	0.72	0.67	0.52	0.57	-
2000-2500	0.72	0.73	0.73	0.73	0.69	0.66	0.53	-	-
2500-3000	0.80	0.85	0.69	0.76	-	-	-	-	-
3000-4000	1.0	0.50	1.0	-	-	-	-	-	-

Table A.5.: Reconstruction and identification efficiency of $W \to q\bar{q}$ using the selections of the all-hadronic analysis.

p_T [GeV]	$\|\eta\|$ range									
	0-0.2	0.2-0.3	0.3-0.4	0.4-0.6	0.6-0.8	0.8-1	1-1.25	1.2-1.5	1.5-2	2-2.4
200-250	-	-	0.48	-	0.32	0.48	0.32	0.16	0.48	-
250-300	0.24	0.32	0.19	0.24	0.27	0.48	0.32	0.24	0.63	-
300-350	0.23	0.25	0.32	0.42	0.34	0.31	0.39	0.26	0.38	0.95
350-400	0.28	0.34	0.39	0.33	0.36	0.38	0.37	0.39	0.29	0.32
400-500	0.41	0.41	0.46	0.45	0.43	0.45	0.38	0.38	0.38	0.40
500-600	0.56	0.54	0.54	0.54	0.53	0.50	0.46	0.39	0.43	0.46
600-700	0.56	0.56	0.55	0.54	0.54	0.50	0.46	0.37	0.44	0.34
700-800	0.54	0.53	0.55	0.53	0.52	0.50	0.45	0.35	0.35	0.48
800-1000	0.53	0.54	0.52	0.53	0.50	0.48	0.41	0.30	0.31	0.95
1000-1200	0.48	0.49	0.47	0.47	0.45	0.43	0.37	0.19	0.35	-
1200-1500	0.46	0.45	0.45	0.45	0.43	0.39	0.31	0.17	0.29	-
1500-2000	0.44	0.45	0.42	0.43	0.39	0.35	0.31	0.14	0.19	-
2000-2500	0.44	0.43	0.45	0.41	0.39	0.32	0.27	-	-	-
2500-3000	0.41	0.41	0.43	0.30	0.27	0.17	-	-	-	-
3000-4000	0.39	0.29	0.48	0.17	-	-	-	-	-	-

Table A.6.: Reconstruction and identification efficiency of $Z \to q\bar{q}$ using the selections of the all-hadronic analysis.

p_T [GeV]	$\|\eta\|$ range									
	0-0.2	0.2-0.3	0.3-0.4	0.4-0.6	0.6-0.8	0.8-1	1-1.25	1.2-1.5	1.5-2	2-2.4
200-250	-	-	0.24	-	-	0.48	-	0.48	-	-
250-300	0.29	-	0.32	0.24	0.17	-	0.32	0.63	-	-
300-350	0.44	0.15	0.32	0.42	0.43	0.20	0.39	0.12	0.42	-
350-400	0.36	0.38	0.45	0.45	0.40	0.39	0.24	0.33	0.35	0.48
400-500	0.48	0.44	0.48	0.45	0.43	0.49	0.39	0.36	0.43	0.56
500-600	0.56	0.57	0.58	0.57	0.56	0.52	0.50	0.42	0.48	0.63
600-700	0.60	0.58	0.59	0.57	0.56	0.53	0.47	0.43	0.46	0.51
700-800	0.57	0.59	0.58	0.57	0.57	0.55	0.48	0.39	0.39	0.71
800-1000	0.57	0.58	0.56	0.57	0.54	0.50	0.46	0.36	0.44	0.95
1000-1200	0.53	0.50	0.54	0.50	0.50	0.46	0.41	0.23	0.38	0.95
1200-1500	0.50	0.49	0.50	0.49	0.48	0.42	0.37	0.24	0.15	-
1500-2000	0.47	0.46	0.46	0.45	0.44	0.40	0.32	0.23	-	-
2000-2500	0.45	0.46	0.46	0.42	0.41	0.40	0.39	0.32	-	-
2500-3000	0.41	0.34	0.45	0.44	0.36	0.16	-	-	-	-
3000-4000	0.42	0.48	-	-	-	-	-	-	-	-

B. Efficiency Tests

In order to test the method of efficiency parametrisation that is used for the main limit setting procedure, the excact efficiency and the one using the parametrisation method are calculated for different theory models and resonance masses and widths. "Efficiency" in this section always means the product of the reconstruction and ID efficiency and the acceptance. The relative difference between the two methods is calculated as

$$\Delta\epsilon = \frac{\epsilon_{exact} - \epsilon_{param}}{\epsilon_{param}} \ . \tag{B.1}$$

The uncertainties on the signal yield are derived from these tests by calculating

$$\max \left(\frac{\epsilon_{exact} - \epsilon_{param}}{\epsilon_{param}} \right) \Bigg|_{\text{theory models}} \tag{B.2}$$

and rounding up towards the nearest multiple of 5.

Table B.1.: Comparison between the exact efficiency×acceptance obtained using the full analysis selection on reconstructed events and the efficiency×acceptance obtained using the reweighting procedure. In this self-consistency test the procedure is used on the same narrow width Bulk-Graviton MC-samples used to calculate the efficiency tables.

	X→WW→ $e\nu q\bar{q}'$			X→ WW→ $\mu\nu q\bar{q}'$		
M_x	ϵ_{exact}	ϵ_{param}	$\Delta\epsilon$ (in %)	ϵ_{exact}	ϵ_{param}	$\Delta\epsilon$ (in %)
800	0.129	0.110	17.2	0.2212	0.1997	10.8
1200	0.1895	0.1792	5.8	0.2663	0.2572	3.5
1400	0.2035	0.1959	3.9	0.2685	0.2667	0.7
1800	0.2212	0.2176	1.6	0.2723	0.2764	-1.5
2000	0.2257	0.2218	1.8	0.2750	0.2784	-1.2
2500	0.2317	0.2281	1.6	0.2715	0.2722	-0.3
3000	0.2300	0.2294	0.3	0.2631	0.2666	-1.3
3500	0.2381	0.2335	1.9	0.2573	0.2637	-2.4
4500	0.2311	0.2339	-1.2	0.2557	0.2684	-4.7

Table B.2.: Comparison between the exact efficiency×acceptance obtained using the full analysis selection on reconstructed events and the efficiency×acceptance obtained using the reweighting procedure. The procedure is used on a set of narrow width W′ samples.

	W′ →WZ→ $e\nu q\bar{q}'$			W′ → WZ→ $\mu\nu q\bar{q}'$		
M_x	ϵ_{exact}	ϵ_{param}	$\Delta\epsilon$ (in %)	ϵ_{exact}	ϵ_{param}	$\Delta\epsilon$ (in %)
800	0.129	0.117	10.7	0.2216	0.2159	2.6
1200	0.2204	0.2010	9.7	0.3000	0.2872	4.5
1400	0.2441	0.2235	9.2	0.3193	0.3101	3.0
1800	0.2705	0.2521	7.3	0.3298	0.3218	2.5
2000	0.2778	0.2613	6.3	0.3284	0.3244	1.2
2500	0.2837	0.2663	6.5	0.3337	0.3274	1.9
3000	0.2860	0.2705	5.7	0.3212	0.3168	1.4
3500	0.2865	0.2689	6.6	0.3209	0.3138	2.3
4500	0.2765	0.2631	5.1	0.3026	0.3051	-0.8

Table B.3.: Comparison between the exact efficiency×acceptance obtained using the full analysis selection on reconstructed events and the efficiency×acceptance obtained using the reweighting procedure. The procedure is used on narrow width Z′ samples.

	Z′ →WW→ $e\nu q\bar{q}'$			Z′ → WW→ $\mu\nu q\bar{q}'$		
M_x	ϵ_{exact}	ϵ_{param}	$\Delta\epsilon$ (in %)	ϵ_{exact}	ϵ_{param}	$\Delta\epsilon$ (in %)
800	0.130	0.100	29.3	0.2211	0.1877	17.8
1200	0.1945	0.1671	16.4	0.2737	0.2450	11.7
1400	0.2145	0.1876	14.3	0.2798	0.2542	10.1
1800	0.2351	0.2103	11.8	0.2853	0.2694	5.9
2000	0.2378	0.2145	10.9	0.2882	0.2720	6.0
2500	0.2424	0.2182	11.1	0.2836	0.2664	6.5
3000	0.2423	0.2235	8.4	0.2784	0.2650	5.0
3500	0.2437	0.2229	9.3	0.2742	0.2644	3.7
4500	0.2431	0.2304	5.5	0.2660	0.2617	1.6

Table B.4.: Consistency test using the tables in appendix A on W′ MC samples of different masses and widths.

$\Gamma/m_X = 0.1$

	W′ →WZ→ $e\nu q\bar{q}'$			W′ → WZ→ $\mu\nu q\bar{q}'$		
M_x	ϵ_{exact}	ϵ_{param}	$\Delta\epsilon$ (in %)	ϵ_{exact}	ϵ_{param}	$\Delta\epsilon$ (in %)
800	0.139	0.124	12.2	0.2134	0.2091	2.1
1200	0.2195	0.2016	8.9	0.2957	0.2834	4.4
2000	0.2723	0.2572	5.9	0.3308	0.3258	1.5
3000	0.2911	0.2712	7.3	0.3247	0.3172	2.4
4000	0.2769	0.2613	5.9	0.3107	0.3082	0.8

$\Gamma/m_X = 0.2$

	W′ →WZ→ $e\nu q\bar{q}'$			W′ → WZ→ $\mu\nu q\bar{q}'$		
M_x	ϵ_{exact}	ϵ_{param}	$\Delta\epsilon$ (in %)	ϵ_{exact}	ϵ_{param}	$\Delta\epsilon$ (in %)
800	0.148	0.132	11.5	0.2279	0.2186	4.3
1200	0.2233	0.2072	7.8	0.3013	0.2903	3.8
2000	0.2752	0.2570	7.1	0.3275	0.3205	2.2
3000	0.2814	0.2655	6.0	0.3192	0.3143	1.6
4000	0.2778	0.2592	7.2	0.3027	0.3024	0.1

$\Gamma/m_X = 0.3$

	W′ →WZ→ $e\nu q\bar{q}'$			W′ → WZ→ $\mu\nu q\bar{q}'$		
M_x	ϵ_{exact}	ϵ_{param}	$\Delta\epsilon$ (in %)	ϵ_{exact}	ϵ_{param}	$\Delta\epsilon$ (in %)
800	0.158	0.142	10.7	0.2379	0.2279	4.4
1200	0.2231	0.2085	7.0	0.3030	0.2907	4.3
2000	0.2728	0.2566	6.3	0.3264	0.3185	2.5
3000	0.2843	0.2641	7.6	0.3193	0.3122	2.3
4000	0.2720	0.2549	6.7	0.3047	0.2985	2.1

Table B.5.: Consistency test using the tables in appendix A on RS1-Graviton MC samples. The reconstruction efficiency for the hadronically decaying W boson is corrected by a constant factor of 1.305 to take effects of W boson polarisation into account.

$\Gamma/m_X = 0.1$

	X→WW→ $e\nu q\bar{q}'$			X→ WW→ $\mu\nu q\bar{q}'$		
M_x	ϵ_{exact}	ϵ_{param}	$\Delta\epsilon$ (in %)	ϵ_{exact}	ϵ_{param}	$\Delta\epsilon$ (in %)
800	0.046	0.033	38.2	0.0908	0.0730	24.3
1200	0.0838	0.0695	20.5	0.1389	0.1200	15.7
2000	0.1200	0.1089	10.2	0.1673	0.1610	3.9
3000	0.1405	0.1303	7.8	0.1783	0.1748	2.0
4000	0.1467	0.1384	6.0	0.1740	0.1758	-1.0

$\Gamma/m_X = 0.2$

	X→WW→ $e\nu q\bar{q}'$			X→ WW→ $\mu\nu q\bar{q}'$		
M_x	ϵ_{exact}	ϵ_{param}	$\Delta\epsilon$ (in %)	ϵ_{exact}	ϵ_{param}	$\Delta\epsilon$ (in %)
800	0.052	0.037	37.9	0.0931	0.0752	23.8
1200	0.0863	0.0716	20.5	0.1408	0.1225	14.9
2000	0.1210	0.1088	11.2	0.1642	0.1592	3.1
3000	0.1326	0.1272	4.2	0.1724	0.1680	2.6
4000	0.1394	0.1318	5.8	0.1676	0.1709	-1.9

$\Gamma/m_X = 0.3$

	X→WW→ $e\nu q\bar{q}'$			X→ WW→ $\mu\nu q\bar{q}'$		
M_x	ϵ_{exact}	ϵ_{param}	$\Delta\epsilon$ (in %)	ϵ_{exact}	ϵ_{param}	$\Delta\epsilon$ (in %)
800	0.054	0.041	32.9	0.0984	0.0790	24.6
1200	0.0855	0.0719	19.0	0.1376	0.1221	12.7
2000	0.1219	0.1084	12.5	0.1649	0.1553	6.2
3000	0.1349	0.1253	7.7	0.1737	0.1701	2.1
4000	0.1385	0.1299	6.6	0.1727	0.1700	1.6

Table B.6.: Comparison between the exact efficiency×acceptance obtained using the full analysis selection on reconstructed events and the efficiency×acceptance obtained using the reweighting procedure. The procedure is used on broad Z′ samples.

$\Gamma/m_X = 0.1$

	Z′ →WW→ $e\nu q\bar{q}'$			Z′ → WW→ $\mu\nu q\bar{q}'$		
M_x	ϵ_{exact}	ϵ_{param}	$\Delta\epsilon$ (in %)	ϵ_{exact}	ϵ_{param}	$\Delta\epsilon$ (in %)
800	0.135	0.108	25.7	0.2181	0.1860	17.2
1200	0.2011	0.1724	16.7	0.2727	0.2419	12.7
2000	0.2361	0.2139	10.4	0.2840	0.2676	6.1
3000	0.2436	0.2212	10.1	0.2779	0.2648	4.9
4000	0.2412	0.2221	8.6	0.2606	0.2558	1.8

$\Gamma/m_X = 0.2$

	Z′ →WW→ $e\nu q\bar{q}'$			Z′ → WW→ $\mu\nu q\bar{q}'$		
M_x	ϵ_{exact}	ϵ_{param}	$\Delta\epsilon$ (in %)	ϵ_{exact}	ϵ_{param}	$\Delta\epsilon$ (in %)
800	0.143	0.116	23.8	0.2149	0.1865	15.2
1200	0.2029	0.1749	16.0	0.2685	0.2445	9.8
2000	0.2391	0.2133	12.1	0.2869	0.2664	7.7
3000	0.2414	0.2194	10.0	0.2751	0.2614	5.2
4000	0.2389	0.2184	9.4	0.2578	0.2525	2.1

$\Gamma/m_X = 0.3$

	Z′ →WW→ $e\nu q\bar{q}'$			Z′ → WW→ $\mu\nu q\bar{q}'$		
M_x	ϵ_{exact}	ϵ_{param}	$\Delta\epsilon$ (in %)	ϵ_{exact}	ϵ_{param}	$\Delta\epsilon$ (in %)
800	0.149	0.123	21.0	0.2229	0.1939	14.9
1200	0.2034	0.1757	15.8	0.2714	0.2483	9.3
2000	0.2372	0.2128	11.4	0.2770	0.2634	5.1
3000	0.2388	0.2163	10.4	0.2739	0.2625	4.3
4000	0.2359	0.2138	10.3	0.2535	0.2495	1.6

Table B.7.: Comparison between the exact efficiency×acceptance obtained using the full analysis selection on reconstructed events and the efficiency×acceptance obtained using the reweighting procedure. The procedure is used on broad Radion samples.

$\Gamma/m_X = 0.1$

	$G_{Radion} \rightarrow$WW$\rightarrow e\nu q\bar{q}'$			$G_{Radion} \rightarrow$ WW$\rightarrow \mu\nu q\bar{q}'$		
M_x	ϵ_{exact}	ϵ_{param}	$\Delta\epsilon$ (in %)	ϵ_{exact}	ϵ_{param}	$\Delta\epsilon$ (in %)
800	0.101	0.083	22.6	0.1713	0.1509	13.5
1200	0.1580	0.1441	9.6	0.2298	0.2151	6.8
2000	0.1990	0.1941	2.5	0.2470	0.2476	-0.2
3000	0.2058	0.2036	1.1	0.2481	0.2514	-1.3
4000	0.2109	0.2083	1.3	0.2391	0.2447	-2.3

$\Gamma/m_X = 0.2$

	$G_{Radion} \rightarrow$WW$\rightarrow e\nu q\bar{q}'$			$G_{Radion} \rightarrow$ WW$\rightarrow \mu\nu q\bar{q}'$		
M_x	ϵ_{exact}	ϵ_{param}	$\Delta\epsilon$ (in %)	ϵ_{exact}	ϵ_{param}	$\Delta\epsilon$ (in %)
800	0.102	0.084	20.5	0.1672	0.1459	14.6
1200	0.1586	0.1445	9.7	0.2255	0.2159	4.4
2000	0.1916	0.1882	1.8	0.2468	0.2449	0.8
3000	0.2062	0.2013	2.5	0.2454	0.2468	-0.6
4000	0.2033	0.2016	0.8	0.2375	0.2457	-3.4

$\Gamma/m_X = 0.3$

	$G_{Radion} \rightarrow$WW$\rightarrow e\nu q\bar{q}'$			$G_{Radion} \rightarrow$ WW$\rightarrow \mu\nu q\bar{q}'$		
M_x	ϵ_{exact}	ϵ_{param}	$\Delta\epsilon$ (in %)	ϵ_{exact}	ϵ_{param}	$\Delta\epsilon$ (in %)
800	0.106	0.087	21.2	0.1679	0.1473	14.0
1200	0.1572	0.1450	8.4	0.2250	0.2123	5.9
2000	0.1920	0.1857	3.4	0.2437	0.2446	-0.4
3000	0.2010	0.1991	0.9	0.2446	0.2467	-0.8
4000	0.2018	0.1972	2.4	0.2383	0.2424	-1.7

Table B.8.: Comparison between the exact efficiencies using the full analysis selection and the efficiencies obtained using the reweighting procedure. The test was performed on the narrow-width Bulk-Graviton sample for the all-hadronic analysis.

	X→WW→ $q\bar{q}'q\bar{q}'$		
M_x	ϵ_{exact}	ϵ_{param}	$\Delta\epsilon$ (in %)
1200	0.271	0.235	15.3
1400	0.2597	0.2454	5.9
1800	0.2293	0.2329	-1.5
2000	0.2255	0.2254	0.1
2500	0.1965	0.1893	3.8
3000	0.1768	0.1781	-0.7
3500	0.1702	0.1699	0.2
4000	0.1672	0.1688	-0.9
4500	0.1603	0.1668	-3.9

Table B.9.: Comparison between the exact efficiencies using the full analysis selection and the efficiencies obtained using the reweighting procedure on a set of broad Radion samples with two W bosons as intermediate state.

$\Gamma/m_X = 0.1$

	$G_{Radion} \rightarrow$WW$\rightarrow q\bar{q}'q\bar{q}'$		
M_x	ϵ_{exact}	ϵ_{param}	$\Delta\epsilon$ (in %)
1200	0.1711	0.1465	16.8
2000	0.1507	0.1482	1.6
3000	0.1214	0.1212	0.2
4000	0.1178	0.1160	1.6

$\Gamma/m_X = 0.2$

	$G_{Radion} \rightarrow$WW$\rightarrow q\bar{q}'q\bar{q}'$		
M_x	ϵ_{exact}	ϵ_{param}	$\Delta\epsilon$ (in %)
1200	0.1647	0.1370	20.2
2000	0.1418	0.1429	-0.7
3000	0.1261	0.1240	1.7
4000	0.1201	0.1171	2.6

$\Gamma/m_X = 0.3$

	$G_{Radion} \rightarrow$WW$\rightarrow q\bar{q}'q\bar{q}'$		
M_x	ϵ_{exact}	ϵ_{param}	$\Delta\epsilon$ (in %)
1200	0.1587	0.1310	21.1
2000	0.1479	0.1427	3.7
3000	0.1271	0.1253	1.5
4000	0.1205	0.1205	0.0

Table B.10.: Comparison between the exact efficiencies using the full analysis selection and the efficiencies obtained using the reweighting procedure on a set of narrow-width Radion samples with two Z bosons as intermediate state.

	$G_{Radion} \rightarrow$ZZ$\rightarrow q\bar{q}'q\bar{q}'$		
M_x	ϵ_{exact}	ϵ_{param}	$\Delta\epsilon$ (in %)
1200	0.199	0.176	13.4
1400	0.1974	0.1896	4.1
1800	0.1876	0.1845	1.7
2000	0.1810	0.1778	1.8
2500	0.1534	0.1511	1.6
3000	0.1459	0.1406	3.8
3500	0.1237	0.1278	-3.2
4500	0.1166	0.1220	-4.4

Table B.11.: Comparison between the exact efficiencies using the full analysis selection and the efficiencies obtained using the reweighting procedure on a set of broad Z′ samples for the all-hadronic analysis.

$\Gamma/m_X = 0.1$

	Z′ →WW→ $q\bar{q}'q\bar{q}'$		
M_x	ϵ_{exact}	ϵ_{param}	$\Delta\epsilon$ (in %)
1200	0.2333	0.1776	31.3
2000	0.2067	0.1753	18.0
3000	0.1784	0.1498	19.1
4000	0.1645	0.1427	15.3

$\Gamma/m_X = 0.2$

	Z′ →WW→ $q\bar{q}'q\bar{q}'$		
M_x	ϵ_{exact}	ϵ_{param}	$\Delta\epsilon$ (in %)
1200	0.2376	0.1816	30.9
2000	0.2017	0.1786	13.0
3000	0.1786	0.1492	19.7
4000	0.1637	0.1427	14.8

$\Gamma/m_X = 0.3$

	Z′ →WW→ $q\bar{q}'q\bar{q}'$		
M_x	ϵ_{exact}	ϵ_{param}	$\Delta\epsilon$ (in %)
1200	0.2479	0.1895	30.8
2000	0.2103	0.1837	14.5
3000	0.1805	0.1492	20.9
4000	0.1637	0.1418	15.4

Table B.12.: Comparison between the exact efficiencies using the full analysis selection and the efficiencies obtained using the reweighting procedure. The test was performed on the narrow-width Radion sample for the all-hadronic analysis.

	G_{Radion} →WW→ $q\bar{q}'q\bar{q}'$		
M_x	ϵ_{exact}	ϵ_{param}	$\Delta\epsilon$ (in %)
1400	0.1725	0.1670	3.3
1800	0.1604	0.1584	1.3
2000	0.1518	0.1508	0.7
3000	0.1166	0.1186	-1.6
3500	0.1120	0.1104	1.5
4000	0.1080	0.1126	-4.1
4500	0.1059	0.1105	-4.2

Table B.13.: Comparison between the exact efficiencies using the full analysis selection and the efficiencies obtained using the reweighting procedure on a set of broad-width RS1-Graviton samples. The reconstruction efficiency of the hadronically decaying W boson has been corrected by a constant factor of 1.305 to take effects of W boson polarisation into account.

$\Gamma/m_X = 0.1$

	X→WW→ $q\bar{q}'q\bar{q}'$		
M_x	ϵ_{exact}	ϵ_{param}	$\Delta\epsilon$ (in %)
1200	0.0773	0.0636	21.4
2000	0.0686	0.0712	-3.7
3000	0.0661	0.0643	2.7

$\Gamma/m_X = 0.2$

	X→WW→ $q\bar{q}'q\bar{q}'$		
M_x	ϵ_{exact}	ϵ_{param}	$\Delta\epsilon$ (in %)
1200	0.0733	0.0606	20.9
2000	0.0706	0.0704	0.3
3000	0.0648	0.0642	0.9
4000	0.0660	0.0603	9.4

$\Gamma/m_X = 0.3$

	X→WW→ $q\bar{q}'q\bar{q}'$		
M_x	ϵ_{exact}	ϵ_{param}	$\Delta\epsilon$ (in %)
1200	0.0725	0.0600	20.9
2000	0.0717	0.0682	5.1
3000	0.0660	0.0644	2.5
4000	0.0656	0.0602	8.9

Table B.14.: Comparison between the exact efficiencies using the full analysis selection and the efficiencies obtained using the reweighting procedure. The test was performed on the narrow-width Z′ sample for the all-hadronic analysis.

	Z′ →WW→ $q\bar{q}'q\bar{q}'$		
M_x	ϵ_{exact}	ϵ_{param}	$\Delta\epsilon$ (in %)
1200	0.255	0.198	28.9
1400	0.2376	0.2069	14.8
1800	0.2199	0.1948	12.8
2000	0.2112	0.1886	12.0
2500	0.1922	0.1550	24.0
3000	0.1761	0.1482	18.8
3500	0.1734	0.1402	23.7
4000	0.1594	0.1407	13.3
4500	0.1555	0.1406	10.6

Table B.15.: Comparison between the exact efficiencies using the full analysis selection and the efficiencies obtained using the reweighting procedure on a set of broad-width W′ samples for the all-hadronic analysis.

$\Gamma/m_X = 0.1$

	W′ →WZ→ $q\bar{q}'q\bar{q}'$		
M_x	ϵ_{exact}	ϵ_{param}	$\Delta\epsilon$ (in %)
1200	0.250	0.199	25.3
2000	0.2278	0.1982	14.9
3000	0.1894	0.1597	18.6
4000	0.1726	0.1486	16.1

$\Gamma/m_X = 0.2$

	W′ →WZ→ $q\bar{q}'q\bar{q}'$		
M_x	ϵ_{exact}	ϵ_{param}	$\Delta\epsilon$ (in %)
1200	0.245	0.194	26.6
2000	0.2197	0.1934	13.6
3000	0.1929	0.1614	19.5
4000	0.1661	0.1497	11.0

$\Gamma/m_X = 0.3$

	W′ →WZ→ $q\bar{q}'q\bar{q}'$		
M_x	ϵ_{exact}	ϵ_{param}	$\Delta\epsilon$ (in %)
2000	0.2214	0.1909	16.0
3000	0.1899	0.1621	17.2

C. Shape Hypothesis Tests

To demonstrate the validity of the signal shape parametrisation the histograms derived from MC simulations for different theory models are depicted together with the shape hypothesis (blue curve), which corresponds to a Breit-Wigner distribution convoluted with the narrow resolution function of the theory. The resolution function is fitted to a narrow Bulk-Graviton MC beforehand and then set to its best fit values. The histograms are chosen to contain 90 % of signal events after the full analysis selection with the exception of the m_{VV} cuts, which are omitted on generator level for shape testing in order to avoid a distortion of shapes due to migration.

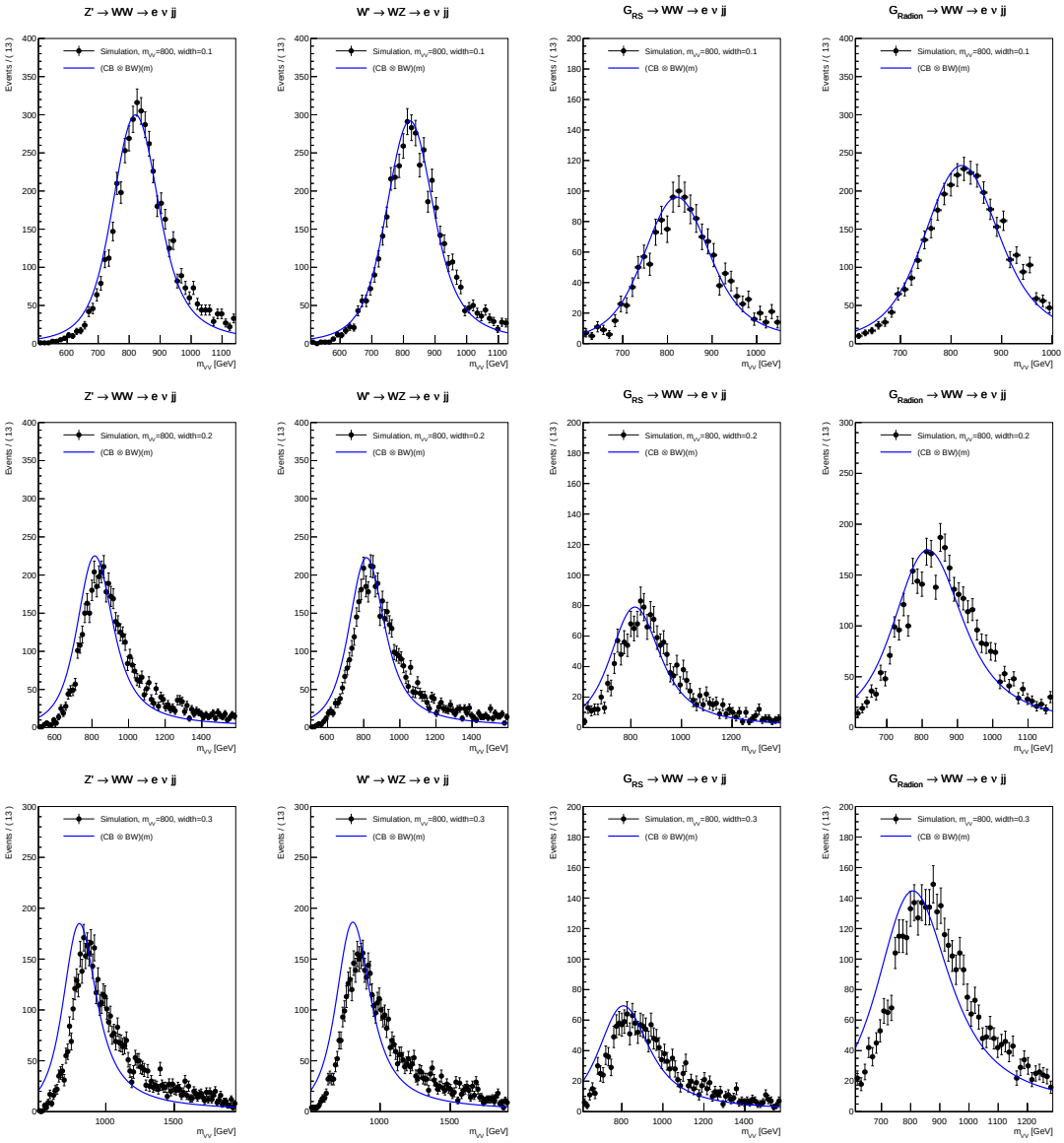

Figure C.1.: The signal shape modelling for different theory models and decay widths of $\Gamma/m_{VV} = 0.1$, 0.2 and 0.3 and a resonance mass $m_X = 800$ GeV. The figure contains the shape modelling for the electron channel of the semileptonic analysis.

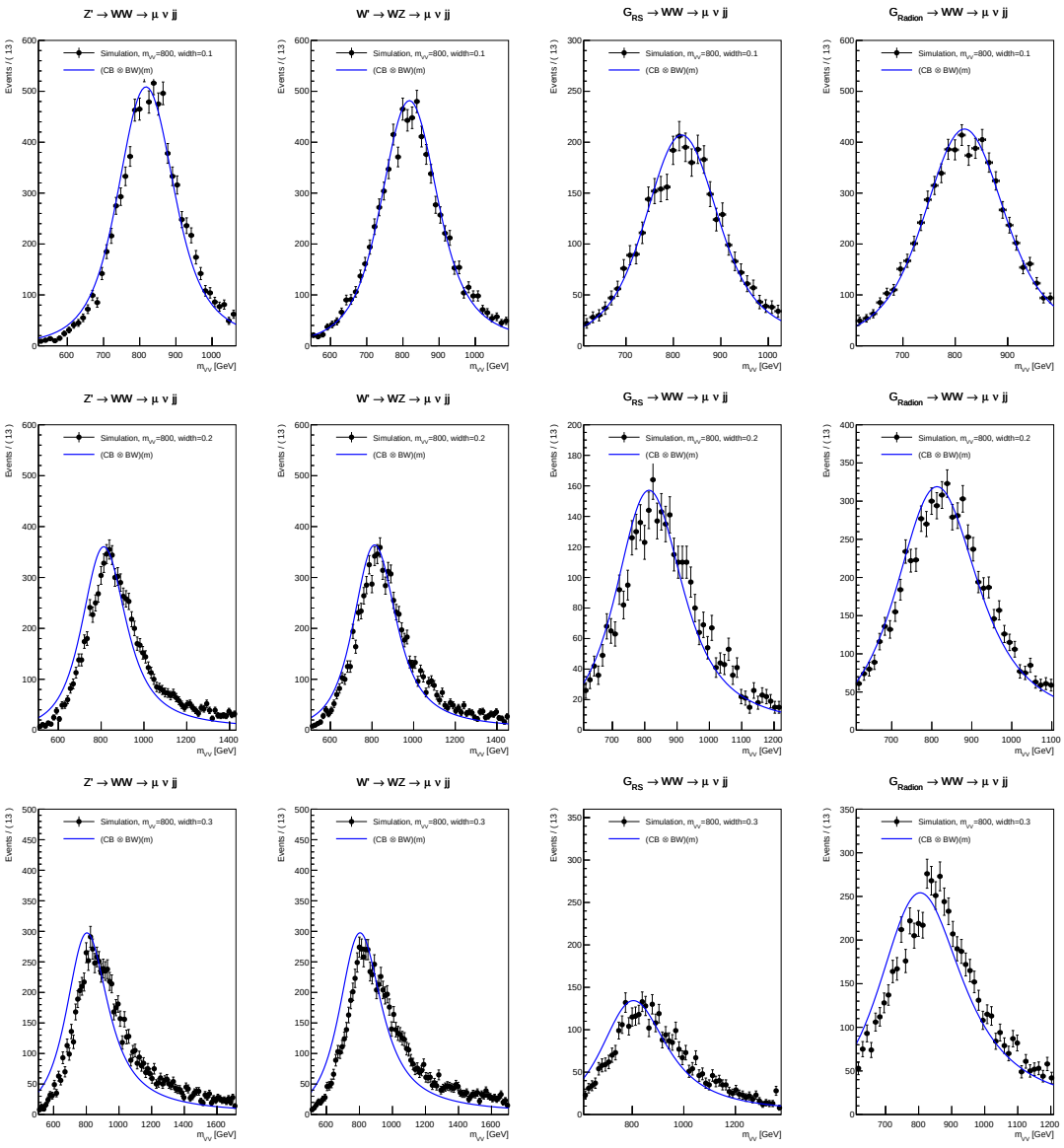

Figure C.2.: The signal shape modelling for different theory models and decay widths of $\Gamma/m_{VV} = 0.1$, 0.2 and 0.3 and a resonance mass $m_X = 800$ GeV. The figure contains the shape modelling for the muon channel of the semileptonic analysis. The mean shift observed here is small enough to be contained within the fit-uncertainties of the mean value of the narrow-width function.

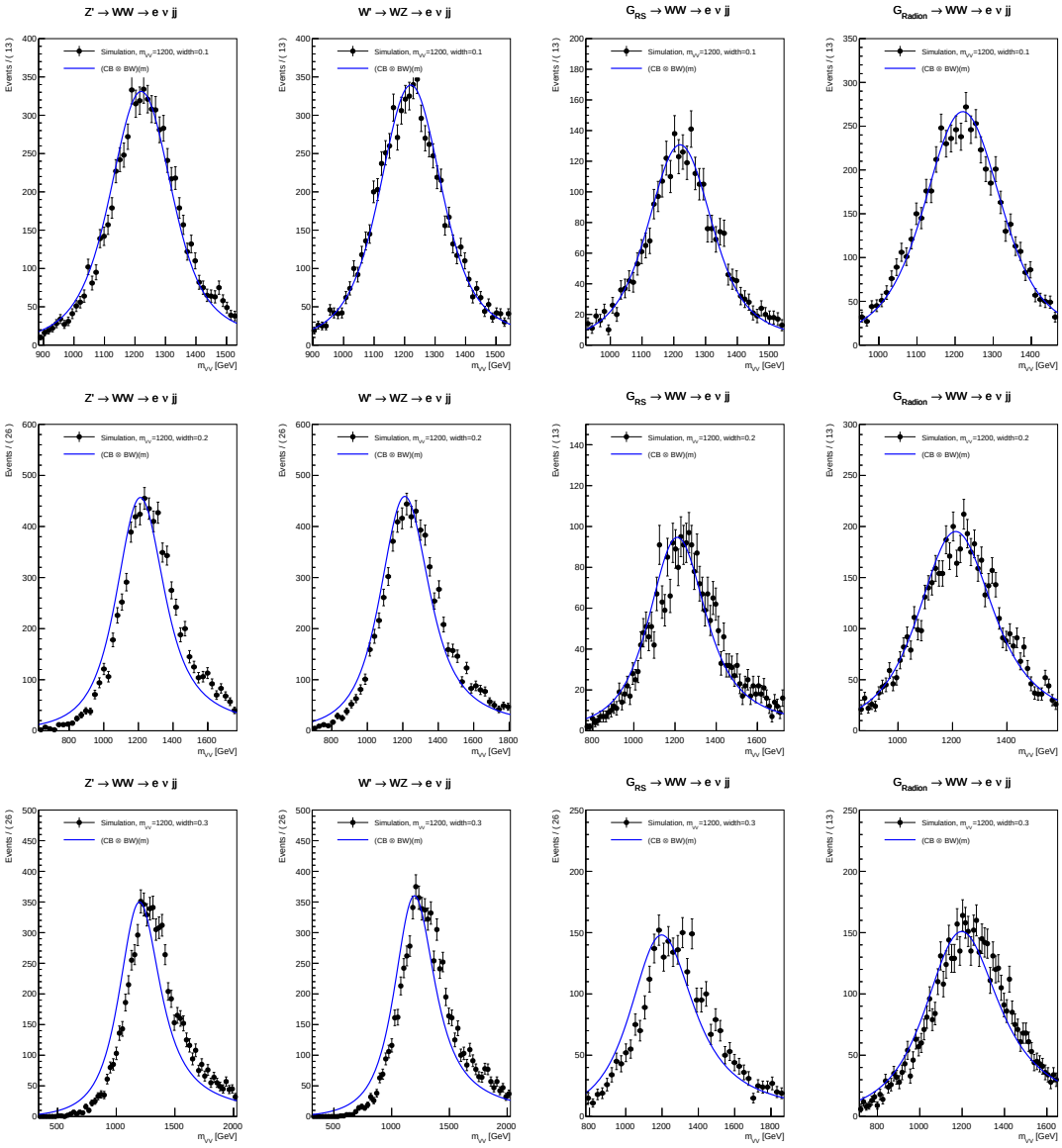

Figure C.3.: The signal shape modelling for different theory models and decay widths of $\Gamma/m_{VV} = 0.1$, 0.2 and 0.3 and a resonance mass $m_X = 1200$ GeV. The figure contains the shape modelling for the electron channel of the semileptonic analysis.

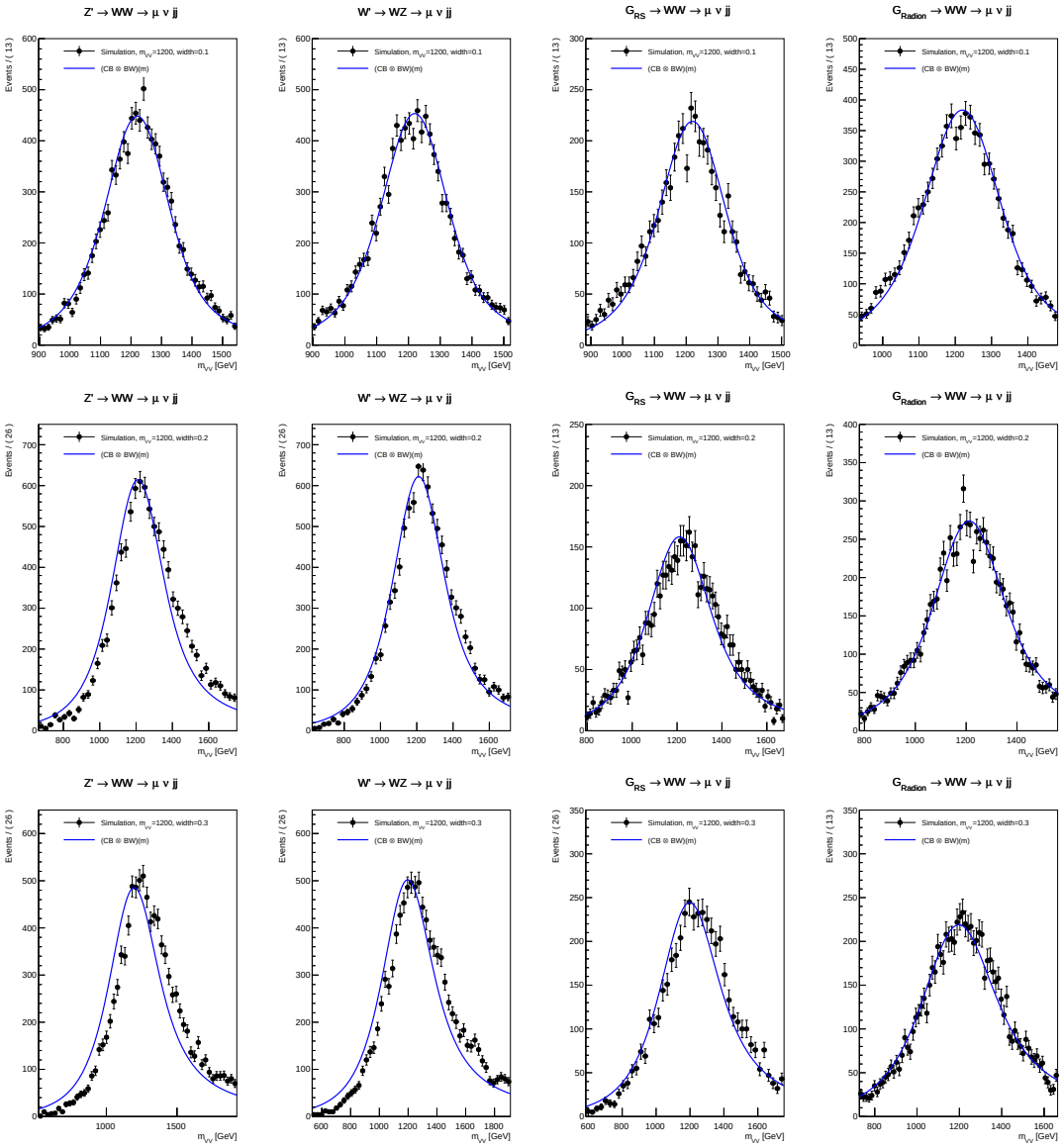

Figure C.4.: The signal shape modelling for different theory models and decay widths of $\Gamma/m_{VV} = 0.1$, 0.2 and 0.3 and a resonance mass $m_X = 1200$ GeV. The figure contains the shape modelling for the muon channel of the semileptonic analysis.

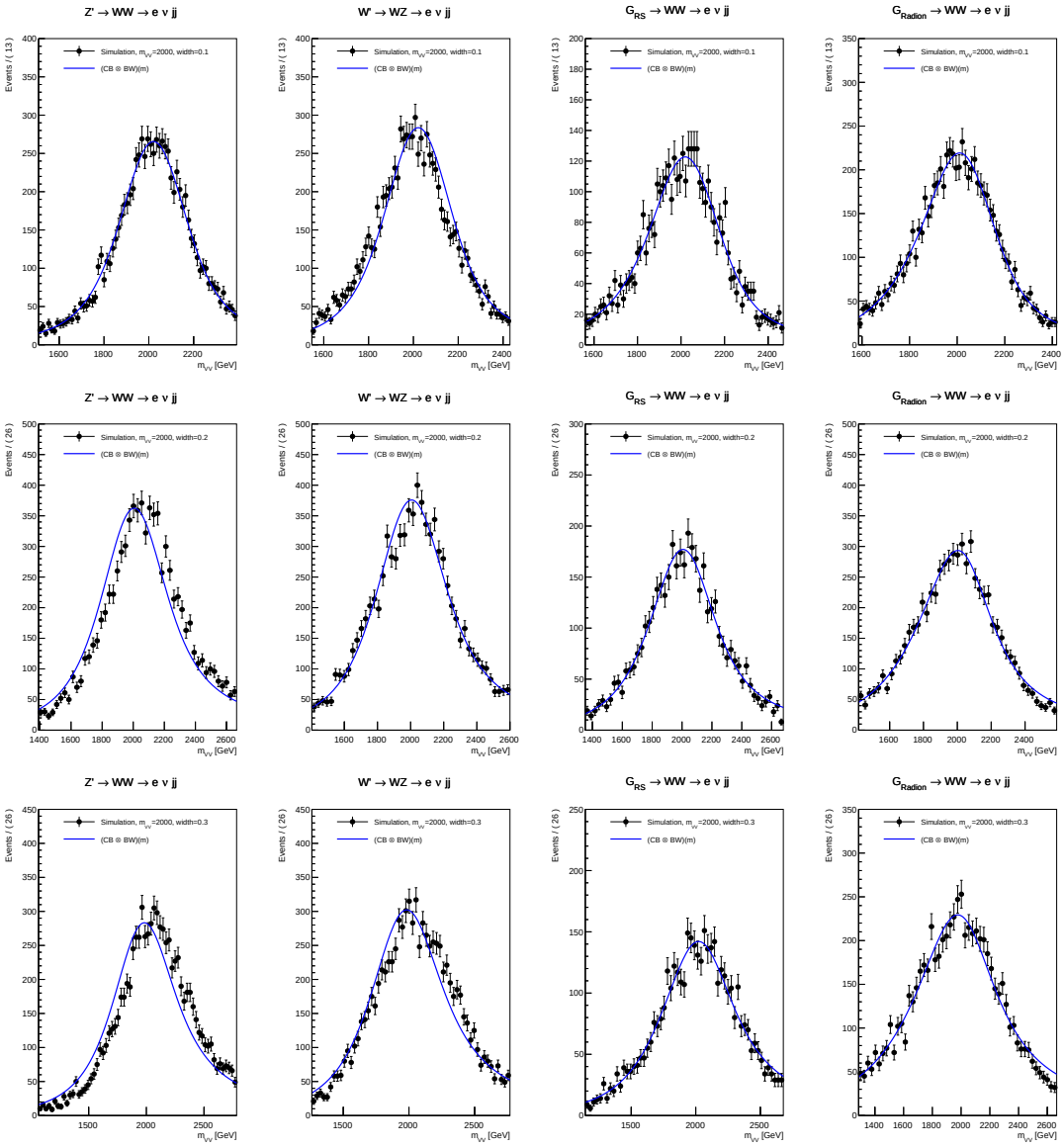

Figure C.5.: The signal shape modelling for different theory models and decay widths of $\Gamma/m_{VV} = 0.1$, 0.2 and 0.3 and a resonance mass $m_X = 2000$ GeV. The figure contains the shape modelling for the electron channel of the semileptonic analysis.

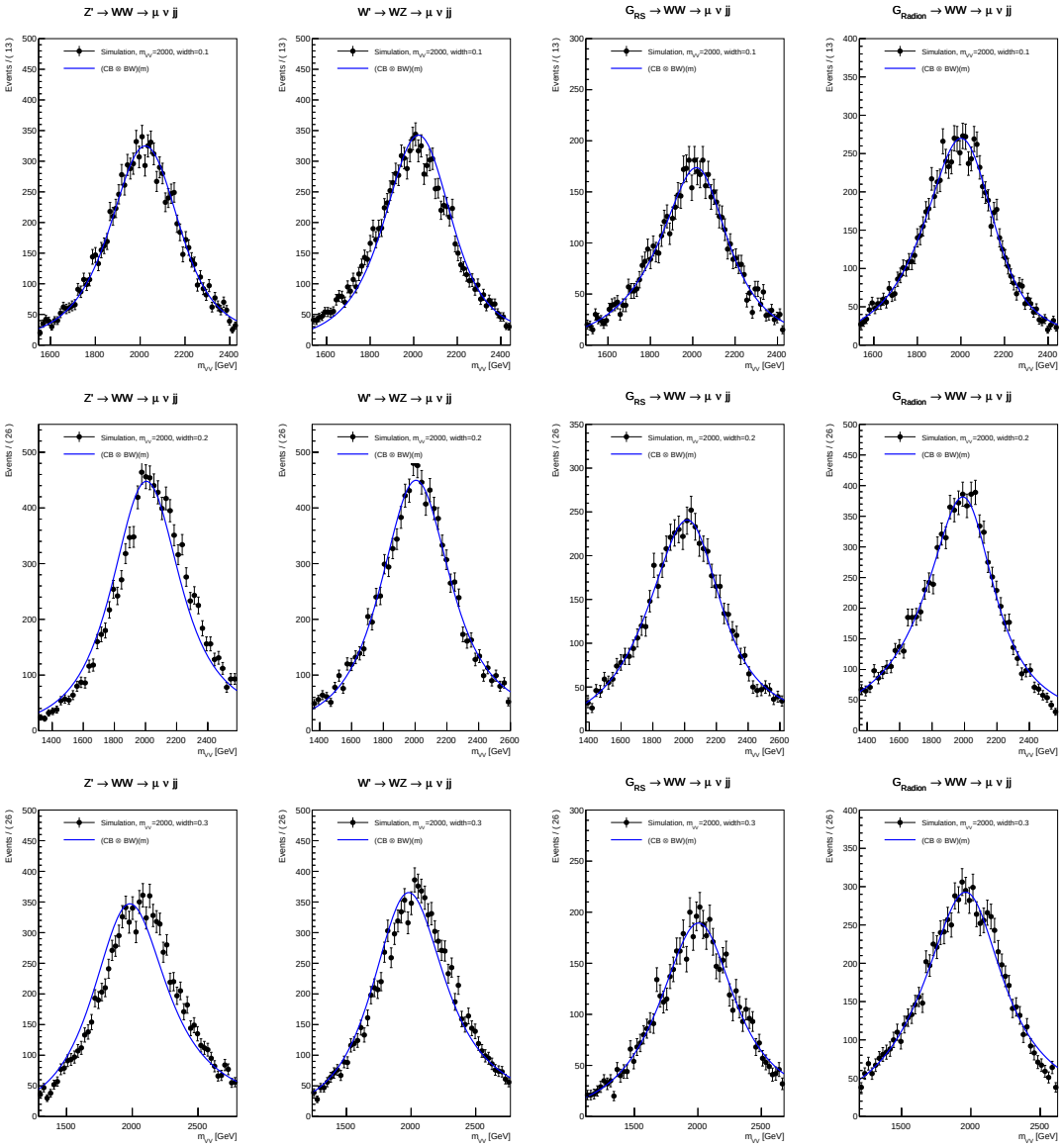

Figure C.6.: The signal shape modelling for different theory models and decay widths of $\Gamma/m_{VV} = 0.1$, 0.2 and 0.3 and a resonance mass $m_X = 2000$ GeV. The figure contains the shape modelling for the muon channel of the semileptonic analysis.

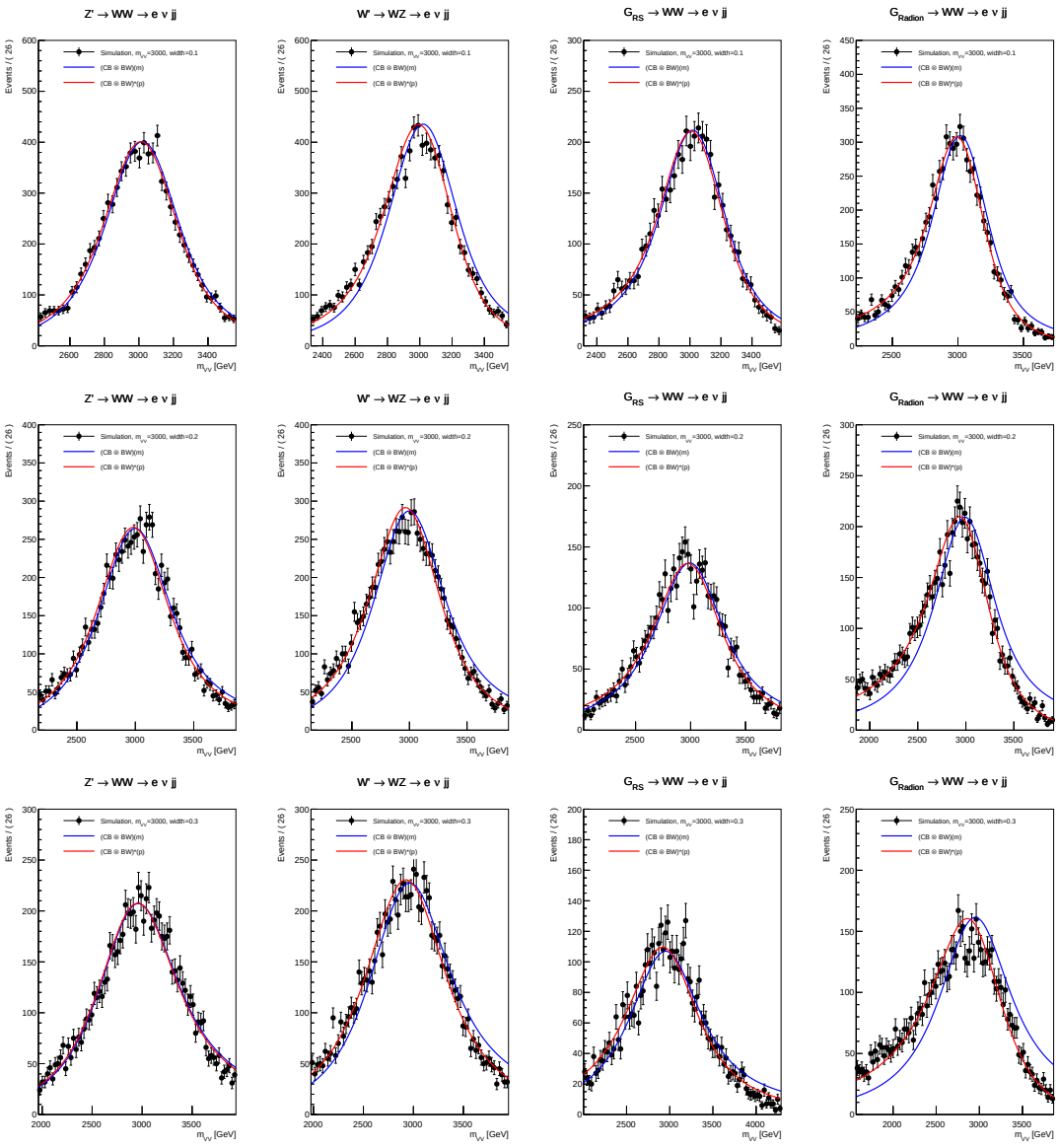

Figure C.7.: The signal shape modelling for different theory models and decay widths of $\Gamma/m_{VV} = 0.1$, 0.2 and 0.3 and a resonance mass $m_X = 3000$ GeV. The figure contains the shape modelling for the electron channel of the semileptonic analysis. The red curve is the signal hypothesis times a Chebichev polynomial of degree one, which is fitted to the MC histograms.

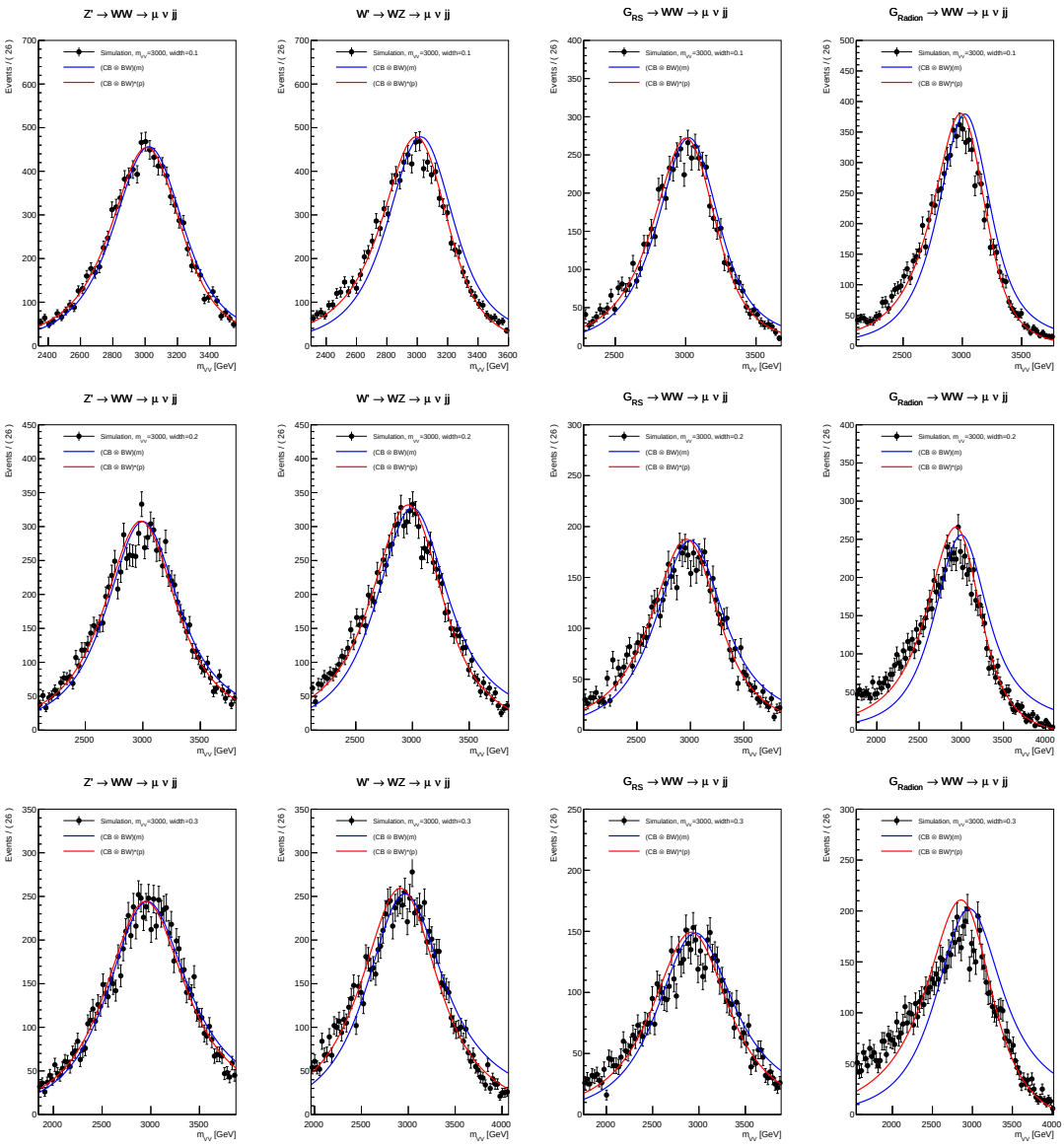

Figure C.8.: The signal shape modelling for different theory models and decay widths of $\Gamma/m_{VV} = 0.1, 0.2$ and 0.3 and a resonance mass $m_X = 3000$ GeV. The figure contains the shape modelling for the muon channel of the semileptonic analysis. The red curve is the signal hypothesis times a Chebichev polynomial of degree one, which is fitted to the MC histograms.

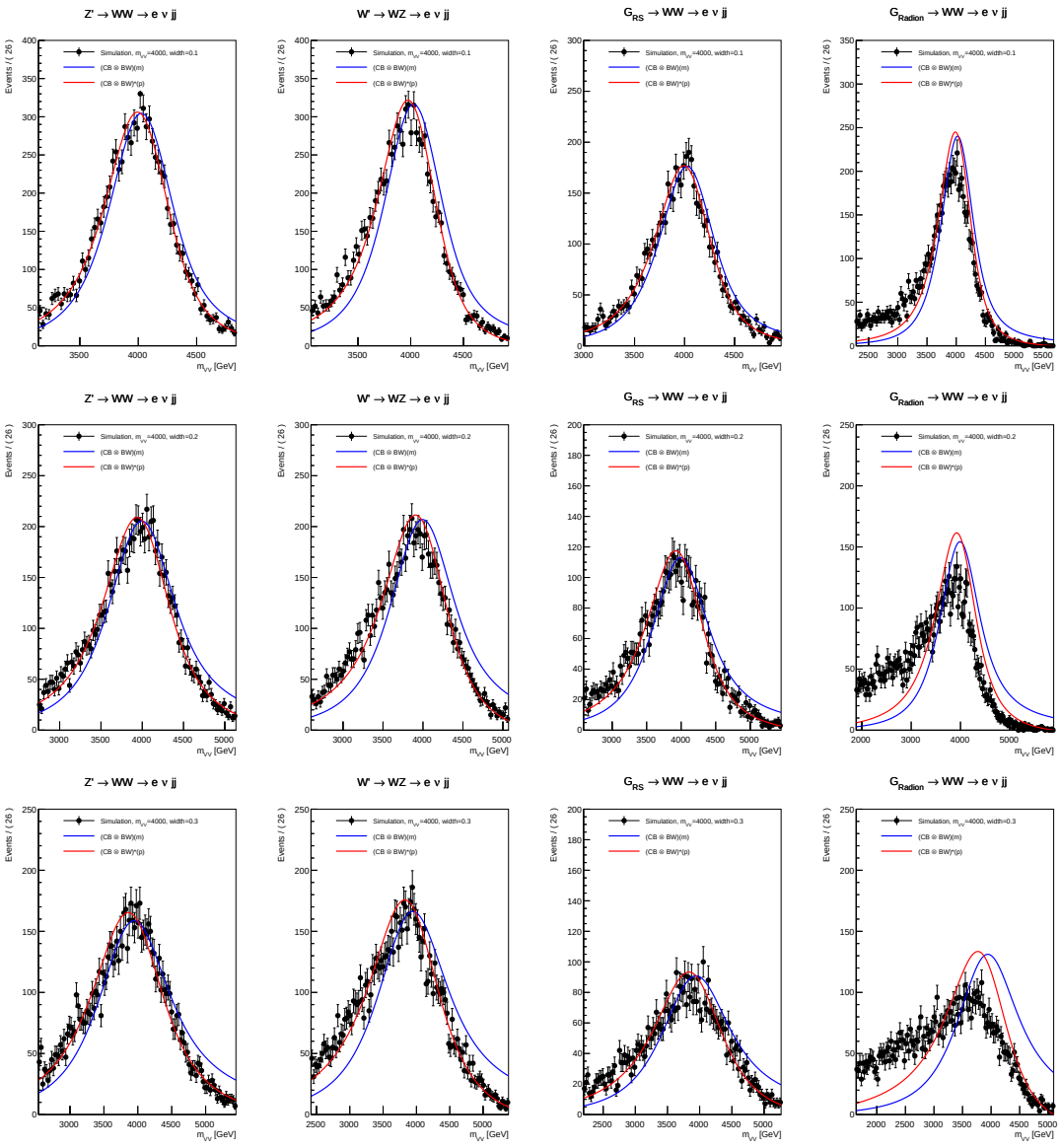

Figure C.9.: The signal shape modelling for different theory models and decay widths of $\Gamma/m_{VV} = 0.1$, 0.2 and 0.3 and a resonance mass $m_X = 4000$ GeV. The figure contains the shape modelling for the electron channel of the semileptonic analysis. The red curve is the signal hypothesis times a Chebichev polynomial of degree one, which is fitted to the MC histograms.

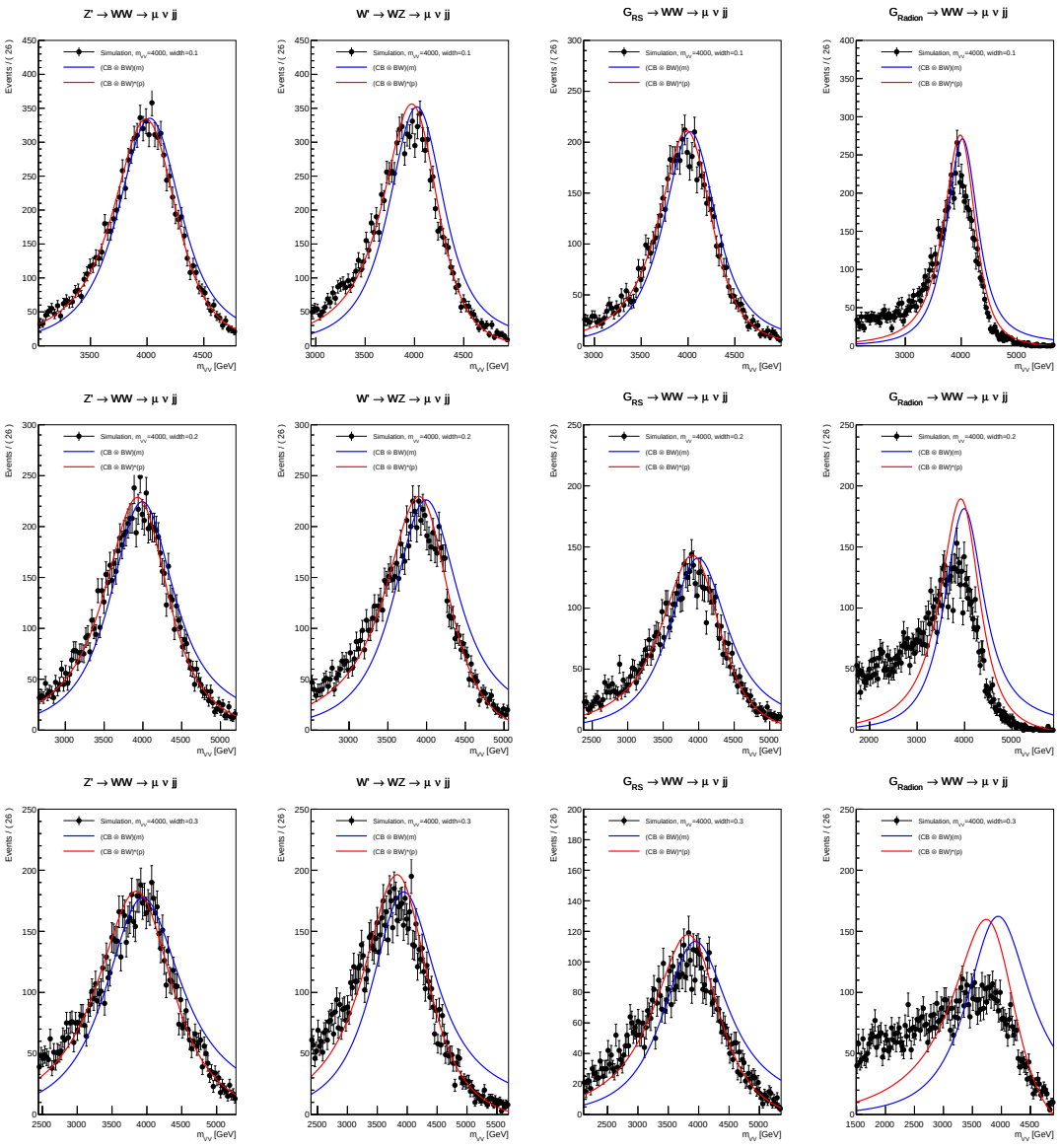

Figure C.10.: The signal shape modelling for different theory models and decay widths of $\Gamma/m_{VV} = 0.1$, 0.2 and 0.3 and a resonance mass $m_X = 4000$ GeV. The figure contains the shape modelling for the muon channel of the semileptonic analysis. The red curve is the signal hypothesis times a Chebichev polynomial of degree one, which is fitted to the MC histograms.

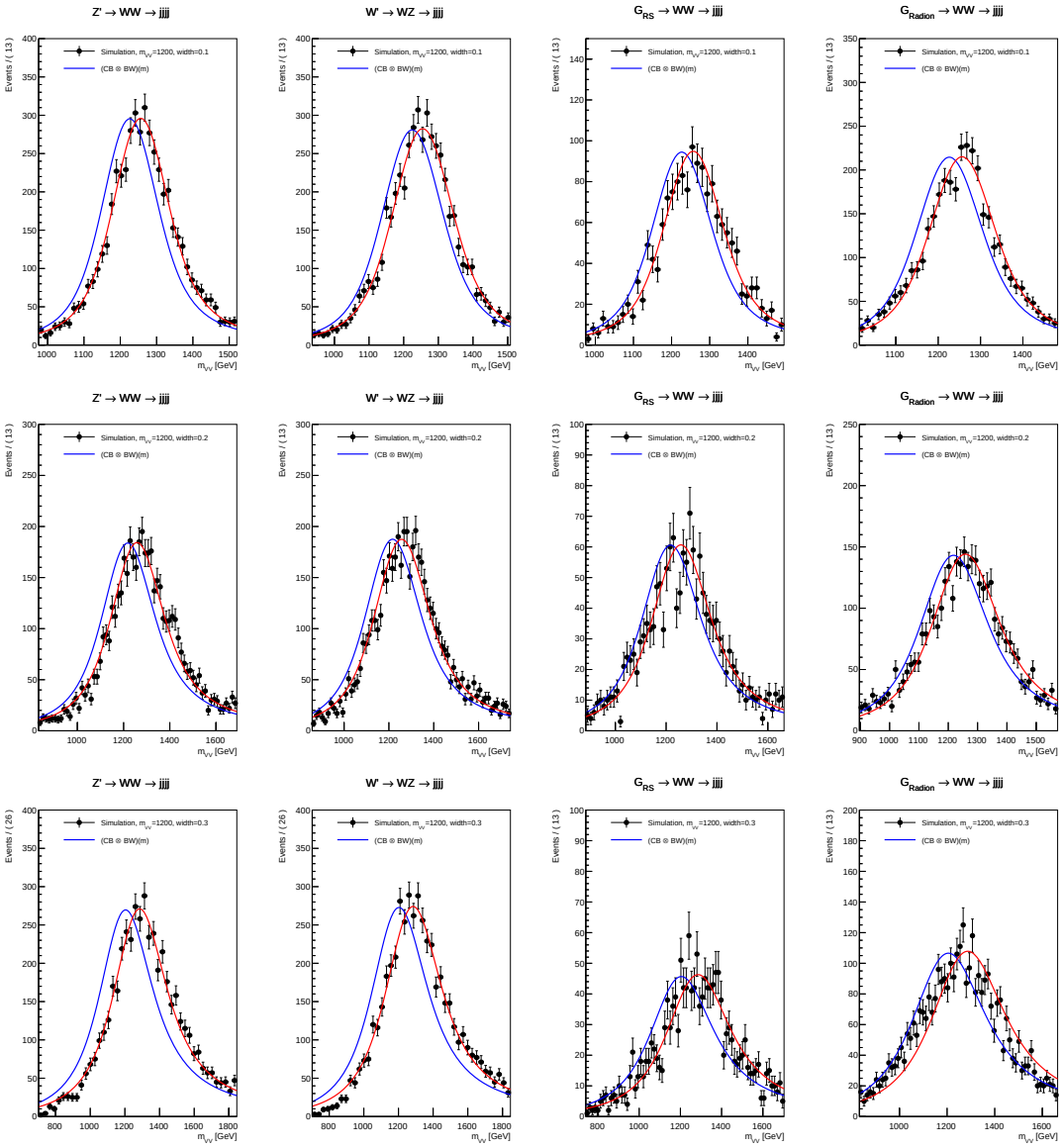

Figure C.11.: The signal shape modelling for different theory models and decay widths of $\Gamma/m_{VV} = 0.1$, 0.2 and 0.3 and a resonance mass $m_X = 1200$ GeV. The figure contains the shape modelling for the all-hadronic analysis. The red curve is the normal signal shape modelling with its peak mass value shifted.

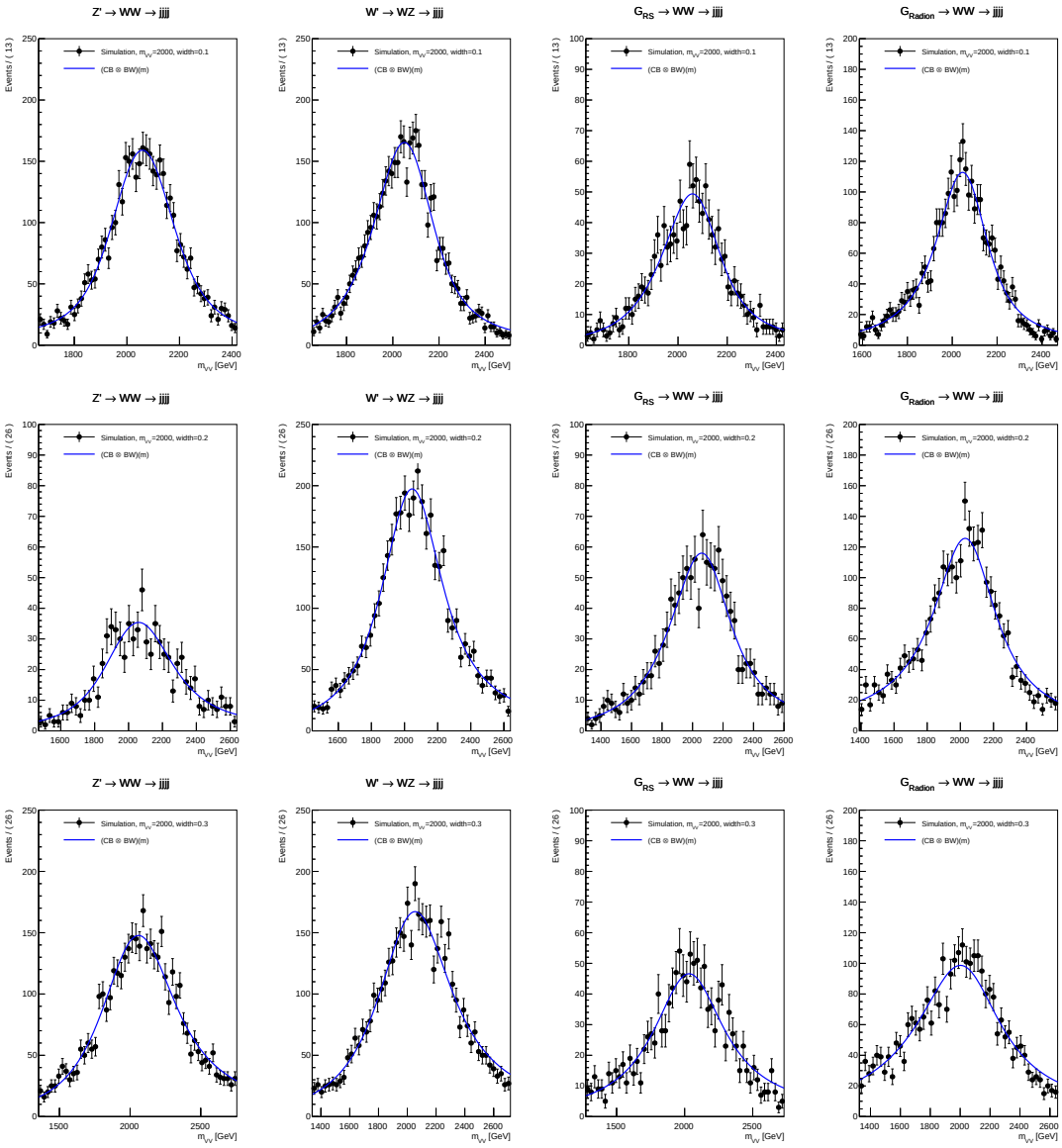

Figure C.12.: The signal shape modelling for different theory models and decay widths of $\Gamma/m_{VV} = 0.1$, 0.2 and 0.3 and a resonance mass $m_X = 2000$ GeV. The figure contains the shape modelling for the all-hadronic analysis.

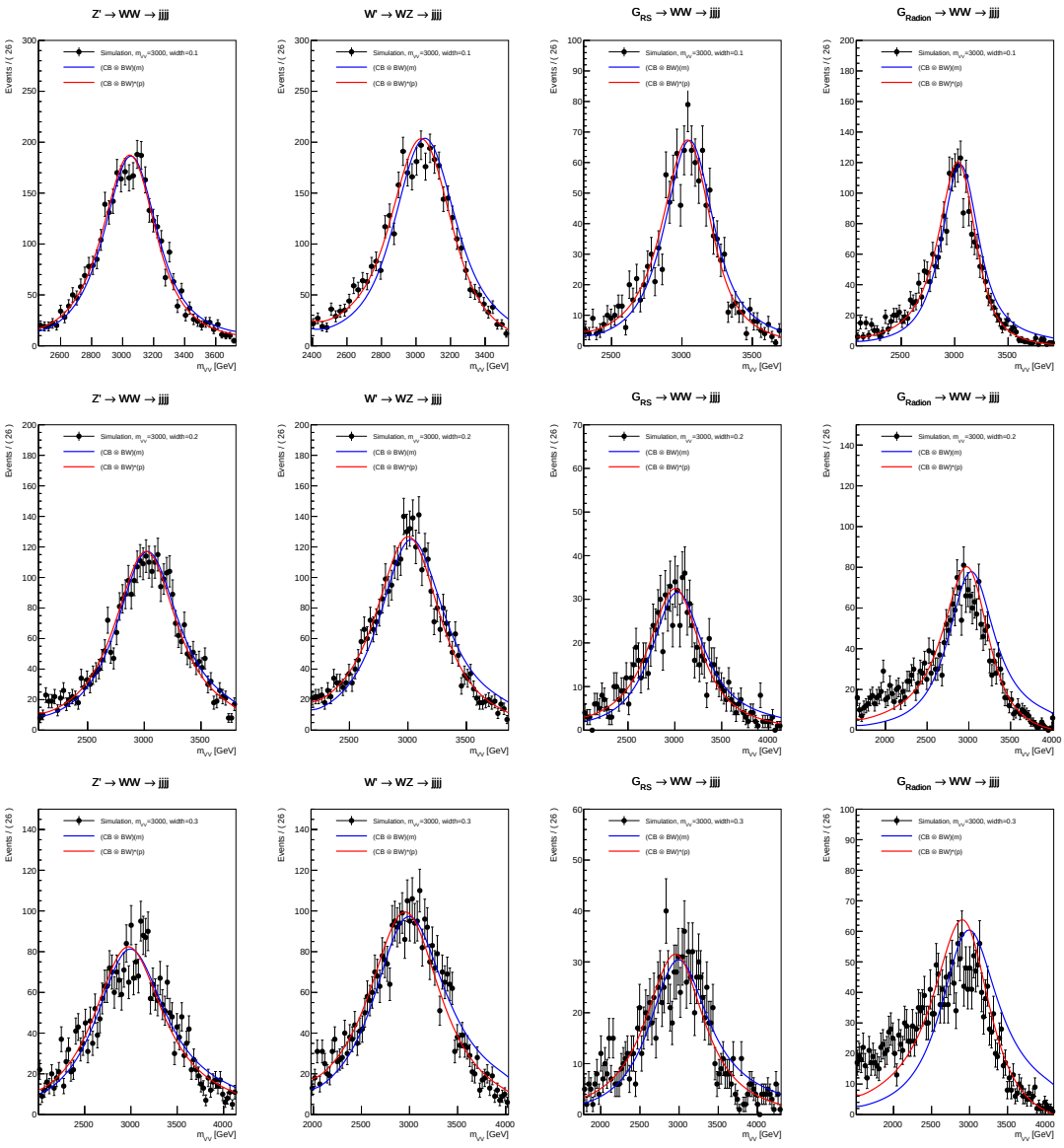

Figure C.13.: The signal shape modelling for different theory models and decay widths of $\Gamma/m_{VV} = 0.1$, 0.2 and 0.3 and a resonance mass $m_X = 3000$ GeV. The figure contains the shape modelling for the all-hadronic analysis. The red curve is the signal hypothesis times a Chebichev polynomial of degree one, which is fitted to the MC histograms.

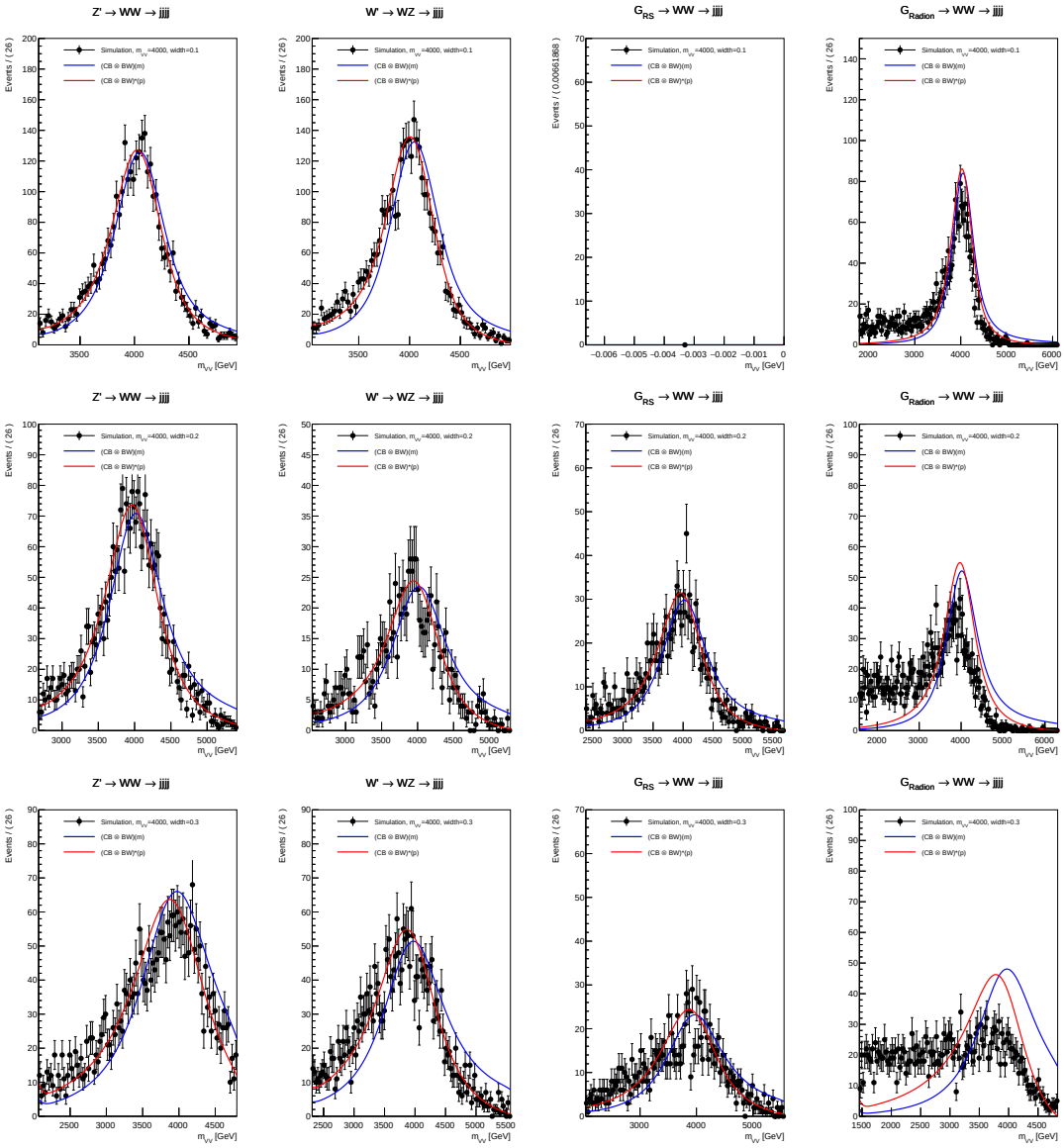

Figure C.14.: The signal shape modelling for different theory models and decay widths of $\Gamma/m_{VV} = 0.1$, 0.2 and 0.3 and a resonance mass $m_X = 4000$ GeV. The figure contains the shape modelling for the all-hadronic analysis. The red curve is the signal hypothesis times a Chebichev polynomial of degree one, which is fitted to the MC histograms. The histogram for an RS1-Graviton model and a mass of 4 TeV with a relative width of 0.1 is empty, because there is no simulation for this point.

D. χ^2 Tests for Broad Signal Shapes

This section contains the reduced χ^2 values for a comparison between the histograms filled with the reconstructed m_{VV} spectrum and the complete signal shape hypothesis. The complete signal shape is the narrow-width resolution function convoluted with a Breit-Wigner function. For small masses it includes the mean shift discussed in section 6.4.2 for the all-hadronic channel. For large resonance masses an extra degree of freedom is included as discussed in section 6.4.3. For the calculation of the χ^2 tests the uncertainties on the narrow resolution function are approximated. This is done by calculating for each bin the difference of the function value with all parameters set to best-fit values and the function value with one parameter set to its maximum/minimum value. The maximum difference derived this way is added to the uncertainty of the corresponding MC histogram bin. For small-mass samples a shift of the peak value of the narrow fit function with respect to the MC histograms can be seen. This shift is, however, within the fitted error of the mean value for the resolution function in the semileptonic case. For the calculation of the χ^2 test this parameter is therefore left floating within its uncertainty-bounds and fitted to the broad MC shape. Since the semileptonic analysis uses a mass cut for values of m_{VV} greater than 500 GeV, the calculation of χ^2 values only uses masses larger than 500 GeV. Analogously only masses larger than 1000 GeV are used for the calculations in the all-hadronic channel.

Table D.1.: The reduced χ^2 values for a Radion theory model decaying semileptonically. An accepted test value means the shape hypothesis used in the analysis passed a χ^2 test with a confidence level of 0.05.

CHANNEL	χ^2	MASS [GeV]	WIDTH	ACCEPTED/FAILED
ele/mu	0.58/0.41	800	0.1	a/a
ele/mu	1.07/0.50	800	0.2	a/a
ele/mu	0.57/0.79	800	0.3	a/a
ele/mu	0.49/0.41	1200	0.1	a/a
ele/mu	0.68/0.71	1200	0.2	a/a
ele/mu	0.39/0.53	1200	0.3	a/a
ele/mu	0.56/0.58	2000	0.1	a/a
ele/mu	0.63/1.16	2000	0.2	a/a
ele/mu	0.89/0.81	2000	0.3	a/a
ele/mu	0.67/1.24	3000	0.1	a/a
ele/mu	0.80/1.29	3000	0.2	a/a
ele/mu	1.15/1.56	3000	0.3	a/f
ele/mu	3.17/4.69	4000	0.1	f/f
ele/mu	5.13/9.39	4000	0.2	f/f
ele/mu	4.48/7.01	4000	0.3	f/f

Table D.2.: The reduced χ^2 values for a RS1-Graviton theory model decaying semileptonically. An accepted test value means the shape hypothesis used in the analysis passed a χ^2 test with a confidence level of 0.05.

CHANNEL	χ^2	MASS [GeV]	WIDTH	ACCEPTED/FAILED
ele/mu	0.60/0.39	800	0.1	a/a
ele/mu	0.60/0.63	800	0.2	a/a
ele/mu	0.78/0.69	800	0.3	a/a
ele/mu	0.51/0.66	1200	0.1	a/a
ele/mu	0.60/0.81	1200	0.2	a/a
ele/mu	0.54/0.44	1200	0.3	a/a
ele/mu	0.89/0.66	2000	0.1	a/a
ele/mu	1.02/0.31	2000	0.2	a/a
ele/mu	0.47/0.50	2000	0.3	a/a
ele/mu	0.76/0.93	3000	0.1	a/a
ele/mu	0.62/0.84	3000	0.2	a/a
ele/mu	0.68/0.87	3000	0.3	a/a
ele/mu	0.56/0.63	4000	0.1	a/a
ele/mu	0.68/0.89	4000	0.2	a/a
ele/mu	0.66/1.06	4000	0.3	a/a

Table D.3.: The reduced χ^2 values for a Z′ theory model decaying semileptonically. An accepted test value means the shape hypothesis used in the analysis passed a χ^2 test with a confidence level of 0.05.

CHANNEL	χ^2	MASS [GeV]	WIDTH	ACCEPTED/FAILED
ele/mu	0.89/0.90	800	0.1	a/a
ele/mu	1.04/0.76	800	0.2	a/a
ele/mu	1.34/1.21	800	0.3	a/a
ele/mu	0.43/0.63	1200	0.1	a/a
ele/mu	0.69/0.67	1200	0.2	a/a
ele/mu	0.40/1.10	1200	0.3	a/a
ele/mu	0.49/0.84	2000	0.1	a/a
ele/mu	0.53/0.42	2000	0.2	a/a
ele/mu	0.41/0.51	2000	0.3	a/a
ele/mu	0.45/0.56	3000	0.1	a/a
ele/mu	0.68/0.87	3000	0.2	a/a
ele/mu	0.53/0.59	3000	0.3	a/a
ele/mu	0.55/0.48	4000	0.1	a/a
ele/mu	0.61/0.54	4000	0.2	a/a
ele/mu	0.62/0.68	4000	0.3	a/a

Table D.4.: The reduced χ^2 values for a W′ theory model decaying semileptonically. An accepted test value means the shape hypothesis used in the analysis passed a χ^2 test with a confidence level of 0.05.

CHANNEL	χ^2	MASS [GeV]	WIDTH	ACCEPTED/FAILED
ele/mu	0.78/0.60	800	0.1	a/a
ele/mu	1.04/0.89	800	0.2	a/a
ele/mu	1.30/1.14	800	0.3	f/a
ele/mu	0.57/0.75	1200	0.1	a/a
ele/mu	0.42/0.523	1200	0.2	a/a
ele/mu	0.57/0.72	1200	0.3	a/a
ele/mu	0.67/0.53	2000	0.1	a/a
ele/mu	0.71/0.56	2000	0.2	a/a
ele/mu	0.58/0.43	2000	0.3	a/a
ele/mu	0.86/1.04	3000	0.1	a/a
ele/mu	0.47/0.60	3000	0.2	a/a
ele/mu	0.45/0.83	3000	0.3	a/a
ele/mu	0.94/1.32	4000	0.1	a/a
ele/mu	0.69/0.94	4000	0.2	a/a
ele/mu	0.66/1.23	4000	0.3	a/a

Table D.5.: The reduced χ^2 values for a Radion theory model decaying hadronically. An accepted test value means the shape hypothesis used in the analysis passed a χ^2 test with a confidence level of 0.05.

CHANNEL	χ^2	MASS [GeV]	WIDTH	ACCEPTED/FAILED
had	0.55	1200	0.1	a
had	0.34	1200	0.2	a
had	0.62	1200	0.3	a
had	0.53	2000	0.1	a
had	0.34	2000	0.2	a
had	0.43	2000	0.3	a
had	0.40	3000	0.1	a
had	0.59	3000	0.2	a
had	1.62	3000	0.3	f
had	3.12	4000	0.1	f
had	6.76	4000	0.2	f
had	10.11	4000	0.3	f

Table D.6.: The reduced χ^2 values for a RS1-Graviton theory model decaying hadronically. An accepted test value means the shape hypothesis used in the analysis passed a χ^2 test with a confidence level of 0.05.

CHANNEL	χ^2	MASS [GeV]	WIDTH	ACCEPTED/FAILED
had	0.81	1200	0.1	a
had	0.56	1200	0.2	a
had	0.43	1200	0.3	a
had	0.38	2000	0.1	a
had	0.29	2000	0.2	a
had	0.61	2000	0.3	a
had	0.69	3000	0.1	a
had	0.33	3000	0.2	a
had	0.84	3000	0.3	a
had	-	4000	0.1	-
had	1.12	4000	0.2	a
had	1.11	4000	0.3	a

Table D.7.: The reduced χ^2 values for a Z′ theory model decaying hadronically. An accepted test value means the shape hypothesis used in the analysis passed a χ^2 test with a confidence level of 0.05.

CHANNEL	χ^2	MASS [GeV]	WIDTH	ACCEPTED/FAILED
had	0.53	1200	0.1	a
had	0.37	1200	0.2	a
had	0.21	1200	0.3	a
had	0.41	2000	0.1	a
had	0.49	2000	0.2	a
had	0.19	2000	0.3	a
had	0.48	3000	0.1	a
had	0.52	3000	0.2	a
had	0.58	3000	0.3	a
had	0.36	4000	0.1	a
had	0.39	4000	0.2	a
had	0.34	4000	0.3	a

Table D.8.: The reduced χ^2 values for a W′ theory model decaying hadronically. An accepted test value means the shape hypothesis used in the analysis passed a χ^2 test with a confidence level of 0.05. For the χ^2 test no mass cut is used on the reconstructed events.

CHANNEL	χ^2	MASS [GeV]	WIDTH	ACCEPTED/FAILED
had	0.46	1200	0.1	a
had	0.35	1200	0.2	a
had	0.22	1200	0.3	a
had	0.49	2000	0.1	a
had	0.35	2000	0.2	a
had	0.39	2000	0.3	a
had	1.31	3000	0.1	a
had	0.76	3000	0.2	a
had	0.84	3000	0.3	a
had	1.29	4000	0.1	a
had	0.76	4000	0.2	a
had	1.31	4000	0.3	a

E. Model-Independent Limits

In figure E.1 the difference between the observed and expected limits is illustrated. The observed values of all bins lie well between the 1 σ and 2 σ uncertainty bands.

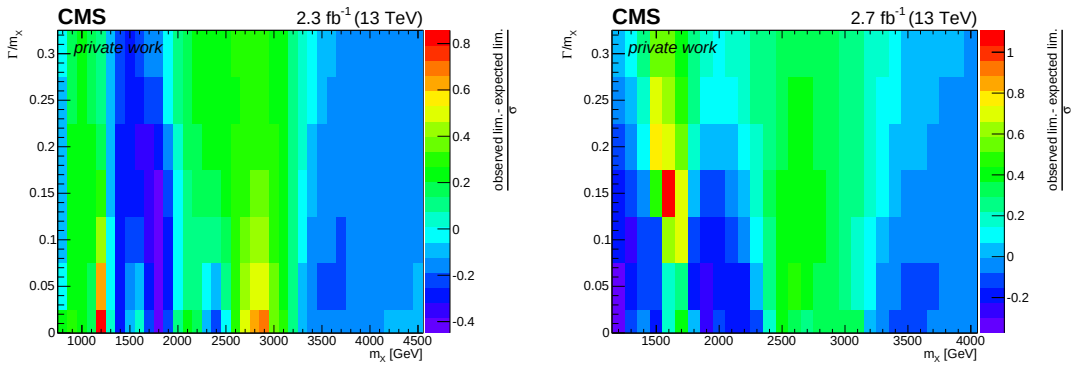

Figure E.1.: On the left is the difference between the observed and expected exclusion limits divided by the variance σ for the semileptonic channel and on the right for the all-hadronic channel.

Table E.1.: Observed 95%CLs limits on the number of signal events for a heavy diboson resonance decaying hadronically. The limits are given as a function of the resonance mass M_X and the relative decay width Γ/M_X.

M_X [GeV]	Γ/M_X						
	0.0	0.05	0.1	0.15	0.2	0.25	0.3
1200	38.1	61.5	88.6	84.6	84.1	82.6	77.9
1300	39.4	54.6	68.8	77.6	82.0	82.7	78.8
1400	29.7	41.7	57.1	66.5	82.6	71.4	85.3
1500	19.5	30.9	44.3	84.2	126.9	115.4	52.2
1600	22.3	33.3	65.5	114.2	100.8	89.9	43.9
1700	22.1	29.1	57.4	70.5	70.5	64.3	56.8
1800	13.0	15.3	24.2	34.5	40.2	40.9	39.6
1900	7.6	11.8	17.2	23.6	27.6	29.1	29.3
2000	7.7	10.5	14.4	18.6	21.4	23.0	23.8
2100	6.2	9.0	12.5	15.5	17.5	18.8	19.5
2200	5.1	7.8	10.9	13.3	15.0	15.9	16.4
2300	4.6	7.8	10.5	12.2	13.2	13.8	14.2
2400	5.8	8.4	10.1	11.1	11.7	12.2	12.5
2500	6.4	8.4	9.4	10.1	10.5	10.9	11.2
2600	5.5	7.8	8.7	9.2	9.6	9.9	10.1
2700	4.8	7.0	7.8	8.3	8.6	8.9	9.2
2800	4.8	6.2	6.8	7.3	7.7	8.0	8.3
2900	4.6	5.5	6.1	6.5	6.8	7.1	7.4
3000	4.5	5.1	5.6	5.9	6.2	6.6	6.9
3100	4.1	4.5	4.9	5.3	5.6	5.9	6.2
3200	2.9	3.7	4.2	4.6	5.0	5.3	5.6
3300	2.4	3.1	3.6	4.0	4.4	4.8	5.1
3400	2.3	2.7	3.1	3.5	4.0	4.3	4.6
3500	2.2	2.5	2.8	3.2	3.6	3.9	4.2
3600	2.2	2.5	2.7	3.0	3.5	3.7	4.0
3700	2.2	2.4	2.6	2.9	3.3	3.5	3.8
4000	2.1	2.2	2.3	2.6	3.0	3.2	3.4

Table E.2.: Expected 95%CLs limits on the number of signal events for a heavy diboson resonance decaying hadronically. The limits are given as a function of the resonance mass M_X and the relative decay width Γ/M_X.

M_X [GeV]	Γ/M_X						
	0.0	0.05	0.1	0.15	0.2	0.25	0.3
1200	59.9	89.8	111.7	108.1	97.7	86.1	74.8
1300	43.9	67.8	89.1	90.4	85.5	78.7	69.8
1400	32.0	48.2	65.3	71.2	73.7	71.2	64.0
1500	24.4	36.1	48.8	59.3	66.2	64.4	45.2
1600	19.3	28.1	40.4	51.8	57.6	54.9	37.0
1700	15.6	22.8	33.2	42.3	45.8	43.9	40.2
1800	12.5	18.3	26.3	32.7	34.9	34.3	32.2
1900	10.6	15.6	21.7	25.9	27.3	26.8	25.9
2000	8.4	12.8	17.1	20.0	21.2	21.6	21.4
2100	7.3	10.8	13.9	15.7	16.7	17.2	17.2
2200	6.2	9.1	11.3	12.7	13.5	13.8	14.1
2300	5.5	7.8	9.4	10.4	11.1	11.5	11.7
2400	4.8	6.7	8.0	8.7	9.3	9.7	9.9
2500	4.3	5.9	6.9	7.5	8.0	8.3	8.6
2600	4.0	5.3	6.1	6.6	7.0	7.3	7.6
2700	3.7	4.8	5.5	5.9	6.2	6.5	6.7
2800	3.5	4.4	4.9	5.3	5.6	5.8	6.1
2900	3.3	4.1	4.5	4.8	5.1	5.3	5.5
3000	3.1	3.9	4.2	4.5	4.8	5.0	5.2
3100	3.0	3.6	3.9	4.2	4.4	4.6	4.8
3200	2.8	3.4	3.7	3.9	4.1	4.3	4.5
3300	2.7	3.2	3.4	3.7	3.9	4.1	4.3
3400	2.6	3.0	3.2	3.5	3.7	3.9	4.1
3500	2.5	2.8	3.1	3.3	3.5	3.7	3.9
3600	2.5	2.8	3.0	3.2	3.5	3.6	3.8
3700	2.4	2.7	2.8	3.1	3.4	3.5	3.7
3800	2.4	2.6	2.7	3.0	3.3	3.4	3.6
3900	2.3	2.5	2.7	2.9	3.3	3.4	3.5
4000	2.3	2.4	2.5	2.8	3.2	3.3	3.4

Table E.3.: Observed 95%CLs limits on the number of signal events for a heavy resonance decaying semileptonically, for the electron channel. The limits are given as a function of the resonance mass M_X and the relative decay width Γ/M_X.

M_X [GeV]	Γ/M_X							
	0.0	0.05	0.1	0.15	0.2	0.25	0.3	0.35
800	87.9	102.0	108.9	110.0	106.7	100.7	93.7	86.5
900	50.7	62.7	70.0	73.6	74.3	72.9	70.5	67.5
1000	23.9	30.8	35.6	39.7	42.8	44.8	46.0	46.6
1100	17.2	21.0	24.5	27.5	30.1	32.0	33.7	35.1
1200	17.9	19.9	21.4	23.0	24.6	26.3	27.9	29.3
1300	10.6	12.8	14.7	16.9	19.1	21.2	23.2	25.0
1400	7.2	9.7	12.2	14.9	17.5	20.0	22.2	24.1
1500	10.2	12.1	14.4	16.7	19.1	21.4	23.4	24.9
1600	13.2	15.0	17.0	19.3	21.7	23.9	25.4	26.3
1700	9.9	12.7	15.7	18.9	22.1	24.3	25.7	26.4
1800	9.4	13.1	17.1	20.9	23.3	24.3	24.4	24.0
1900	7.3	10.1	13.6	17.4	20.5	22.6	23.9	24.4
2000	8.2	11.0	14.5	17.8	20.3	21.7	22.5	23.0
2100	8.4	11.1	14.5	17.4	19.3	20.2	20.7	21.4
2200	7.2	10.3	13.9	16.6	18.0	18.8	19.4	20.0
2300	6.2	9.6	13.2	15.7	16.8	17.5	18.1	18.7
2400	5.8	9.6	13.0	14.7	15.6	16.3	16.9	17.5
2500	7.1	10.7	12.8	13.9	14.6	15.2	15.8	16.4
2600	8.6	11.0	12.3	13.1	13.6	14.1	14.7	15.3
2700	8.8	10.9	11.8	12.4	12.8	13.2	13.7	14.2
2800	9.1	10.5	11.2	11.7	12.1	12.4	12.8	13.2
2900	8.9	10.0	10.6	11.0	11.4	11.7	12.0	12.4
3000	7.6	9.1	9.8	10.2	10.6	11.0	11.2	11.6
3100	6.2	7.5	8.3	8.9	9.4	9.8	10.1	10.4
3200	5.5	6.5	7.3	7.9	8.5	8.9	9.3	9.7
3300	4.4	5.6	6.3	7.0	7.5	8.0	8.5	8.9
3400	3.6	4.6	5.3	6.0	6.6	7.2	7.7	8.2
3500	3.2	4.0	4.7	5.3	5.8	6.4	6.9	7.5
3600	3.1	3.7	4.2	4.7	5.3	5.8	6.3	6.8
3700	3.0	3.5	3.9	4.4	4.9	5.4	5.9	6.5
4000	3.1	3.4	3.7	4.1	4.5	4.9	5.4	6.0
4100	3.3	3.6	3.9	4.3	4.7	5.2	5.7	6.4
4500	3.4	3.7	4.1	4.4	4.9	5.5	6.4	7.0

Table E.4.: Expected 95%CLs limits on the number of signal events for a heavy resonance decaying semileptonically, for the electron channel. The limits are given as a function of the resonance mass M_X and the relative decay width Γ/M_X.

M_X [GeV]	Γ/M_X							
	0.0	0.05	0.1	0.15	0.2	0.25	0.3	0.35
800	57.0	73.7	85.1	90.5	90.5	87.8	83.5	78.1
900	32.0	41.5	49.0	54.5	58.2	60.0	60.3	59.4
1000	25.2	31.8	37.3	42.0	45.4	47.7	48.7	49.1
1100	20.9	26.2	31.1	35.1	38.3	40.6	42.1	42.5
1200	17.8	22.5	26.8	30.6	33.9	36.3	37.7	38.5
1300	15.0	19.2	23.0	26.8	30.0	32.3	33.8	34.6
1400	13.9	18.1	22.0	25.7	28.7	31.1	32.3	32.9
1500	12.7	16.6	20.5	24.3	27.2	29.2	30.4	30.8
1600	11.9	15.7	19.5	23.1	26.1	27.7	28.4	28.6
1700	10.4	13.9	17.7	21.4	23.9	25.4	25.9	26.1
1800	12.2	17.5	21.8	24.2	25.2	24.9	24.0	23.1
1900	8.7	12.1	15.7	18.5	20.2	21.0	21.4	21.4
2000	8.3	11.6	14.9	17.2	18.5	19.1	19.3	19.6
2100	7.7	10.8	13.7	15.6	16.6	17.0	17.3	17.8
2200	7.3	10.2	12.6	14.1	14.9	15.3	15.8	16.2
2300	6.8	9.6	11.6	12.8	13.5	13.9	14.4	14.8
2400	6.5	8.9	10.6	11.6	12.2	12.6	13.1	13.6
2500	6.1	8.3	9.7	10.5	11.0	11.5	12.0	12.5
2600	5.8	7.7	8.9	9.5	10.0	10.4	10.9	11.3
2700	5.4	7.1	8.1	8.7	9.1	9.5	9.8	10.3
2800	5.2	6.6	7.5	8.0	8.4	8.7	9.0	9.4
2900	5.0	6.2	7.0	7.4	7.8	8.1	8.3	8.7
3000	5.0	6.0	6.6	7.0	7.3	7.6	7.8	8.1
3100	4.4	5.4	5.9	6.3	6.6	6.9	7.2	7.4
3200	4.2	5.0	5.5	5.9	6.2	6.5	6.8	7.0
3300	4.0	4.8	5.3	5.6	6.0	6.2	6.5	6.8
3400	3.9	4.6	5.1	5.4	5.7	6.0	6.2	6.5
3500	3.8	4.5	4.9	5.2	5.5	5.8	6.0	6.3
3600	3.7	4.3	4.7	5.0	5.3	5.6	5.9	6.1
3700	3.7	4.2	4.6	4.9	5.2	5.5	5.8	6.0
4000	3.7	4.1	4.4	4.8	5.1	5.4	5.8	6.1
4100	3.9	4.3	4.7	5.1	5.4	5.8	6.2	6.7
4500	3.9	4.4	4.8	5.2	5.7	6.3	7.0	7.4

Table E.5.: Observed 95%CLs limits on the number of signal events for a heavy resonance decaying semileptonically, for the muon channel. The limits are given as a function of the resonance mass M_X and the relative decay width Γ/M_X.

M_X [GeV]	Γ/M_X							
	0.0	0.05	0.1	0.15	0.2	0.25	0.3	0.35
800	77.9	100.2	110.1	115.0	115.4	111.9	106.3	100.0
900	39.6	53.8	66.9	77.1	83.7	87.1	87.4	85.5
1000	50.0	63.8	76.4	87.0	93.7	95.8	94.0	89.9
1100	45.0	63.6	80.9	94.0	101.5	103.2	100.1	94.3
1200	57.0	70.3	81.6	90.7	96.1	97.1	94.1	88.7
1300	33.6	46.5	57.3	67.0	73.9	76.9	76.2	73.1
1400	24.3	32.4	40.6	49.1	55.9	59.8	60.6	59.3
1500	19.3	25.3	31.7	38.5	44.2	47.4	48.4	48.0
1600	16.2	21.5	27.4	33.4	37.9	40.3	40.9	40.4
1700	12.6	17.2	22.7	28.3	32.6	34.8	35.6	35.3
1800	10.2	15.4	21.5	26.8	30.2	31.8	32.2	31.8
1900	10.8	15.4	20.5	24.2	26.2	27.0	27.3	27.0
2000	13.0	17.7	21.5	23.6	24.4	24.7	24.5	24.1
2100	12.9	17.1	19.9	21.4	21.8	21.8	21.6	21.3
2200	11.5	15.0	17.4	18.7	19.2	19.0	18.9	18.7
2300	8.8	12.3	14.5	15.8	16.5	16.4	16.4	16.3
2400	6.7	9.8	12.0	13.2	14.0	14.3	14.2	14.3
2500	6.0	8.6	10.4	11.4	12.0	12.4	12.7	12.6
2600	6.4	8.5	9.6	10.3	10.7	11.0	11.3	11.5
2700	7.2	8.4	9.1	9.5	9.8	10.0	10.2	10.4
2800	7.3	8.0	8.5	8.8	9.0	9.2	9.3	9.4
2900	7.0	7.6	7.9	8.1	8.3	8.4	8.6	8.7
3000	6.0	6.5	6.6	6.7	6.8	6.8	6.9	6.9
3100	4.8	5.7	6.1	6.4	6.7	6.9	7.1	7.3
3200	3.5	4.4	5.0	5.4	5.8	6.1	6.3	6.6
3300	3.0	3.7	4.3	4.7	5.1	5.5	5.8	6.1
3400	2.8	3.4	3.8	4.2	4.6	5.0	5.3	5.6
3500	2.8	3.2	3.5	3.9	4.3	4.6	4.9	5.3
3600	2.8	3.1	3.4	3.7	4.0	4.3	4.7	5.0
3700	2.8	3.1	3.3	3.6	3.9	4.2	4.5	4.8
4000	2.9	3.1	3.3	3.5	3.8	4.1	4.4	4.8
4100	3.1	3.3	3.5	3.7	4.0	4.3	4.7	5.0
4500	3.2	3.4	3.7	4.0	4.3	4.7	5.2	5.8

Table E.6.: Expected 95%CLs limits on the number of signal events for a heavy resonance decaying semileptonically, for the muon channel. The limits are given as a function of the resonance mass M_X and the relative decay width Γ/M_X.

M_X [GeV]	Γ/M_X							
	0.0	0.05	0.1	0.15	0.2	0.25	0.3	0.35
800	90.2	140.9	159.6	160.6	151.7	137.4	123.1	109.2
900	42.9	61.2	72.6	79.3	81.9	81.4	79.3	76.7
1000	31.1	42.6	50.3	55.9	59.6	61.2	61.7	61.2
1100	26.2	34.4	40.8	46.2	50.4	52.9	54.0	54.0
1200	23.0	30.2	36.3	41.9	46.5	49.5	50.9	51.1
1300	19.9	26.3	32.7	38.9	43.9	47.4	48.5	48.5
1400	17.9	24.4	31.4	38.5	44.4	47.6	48.5	47.6
1500	16.8	23.2	31.0	39.0	44.4	46.7	47.0	45.5
1600	17.4	24.9	33.6	40.8	44.3	44.9	44.0	42.2
1700	16.1	23.9	32.5	38.5	40.9	41.2	40.0	38.5
1800	15.3	23.2	31.1	35.4	36.9	36.6	35.7	34.5
1900	12.3	18.8	24.6	27.7	28.9	29.1	28.8	28.3
2000	11.6	17.3	21.7	23.8	24.4	24.6	24.4	24.1
2100	10.5	15.5	18.6	20.3	20.7	20.9	20.9	20.7
2200	9.5	13.6	16.2	17.4	18.0	18.0	18.0	18.0
2300	8.7	12.0	14.0	15.1	15.7	15.7	15.7	15.7
2400	7.8	10.6	12.2	13.0	13.5	13.8	13.7	13.8
2500	7.1	9.5	10.7	11.3	11.8	12.2	12.3	12.3
2600	6.5	8.5	9.5	10.0	10.5	10.8	11.0	11.2
2700	5.9	7.6	8.4	9.0	9.4	9.6	9.9	10.1
2800	5.5	6.9	7.7	8.1	8.5	8.8	9.0	9.2
2900	5.1	6.4	7.0	7.4	7.8	8.1	8.3	8.5
3000	5.1	5.7	6.1	6.4	6.6	6.8	7.0	7.2
3100	4.4	5.3	5.8	6.2	6.5	6.8	7.1	7.4
3200	4.1	4.9	5.4	5.7	6.0	6.4	6.6	6.9
3300	3.8	4.6	5.0	5.4	5.7	6.0	6.3	6.6
3400	3.6	4.3	4.7	5.1	5.4	5.7	6.0	6.3
3500	3.5	4.1	4.5	4.9	5.2	5.5	5.8	6.1
3600	3.4	4.0	4.3	4.7	5.0	5.3	5.6	5.9
3700	3.4	3.9	4.2	4.6	4.9	5.2	5.5	5.8
4000	3.4	3.8	4.1	4.4	4.7	5.1	5.5	5.8
4100	3.5	3.9	4.2	4.6	5.0	5.4	5.8	6.2
4500	3.5	3.9	4.3	4.8	5.3	5.9	6.5	7.2

Table E.7.: Observed limits on the number of events for a confidence level 95% for muon and electron channel combined. The limits are given as a function of the resonance mass M_X and the relative decay width Γ/M_X.

M_X [GeV]	Γ/M_X						
	0.0	0.05	0.1	0.15	0.2	0.25	0.3
800	139.9	173.5	189.2	192.7	185.7	173.1	157.8
900	66.9	87.8	104.4	115.5	120.4	120.6	117.1
1000	46.9	61.4	72.4	81.6	87.9	91.0	91.4
1100	35.2	47.1	58.2	66.7	72.2	75.3	76.3
1200	50.7	56.5	59.7	62.0	63.8	65.1	65.9
1300	22.7	29.4	34.9	40.4	45.5	49.9	53.0
1400	15.1	20.5	26.3	32.1	37.9	43.0	46.9
1500	18.2	22.4	27.1	32.1	37.2	41.7	45.1
1600	20.1	24.1	28.4	33.4	38.3	42.3	44.9
1700	14.2	19.0	24.4	30.6	36.7	41.3	44.0
1800	11.8	17.7	24.5	31.6	37.0	40.0	40.6
1900	11.6	16.6	23.1	29.8	35.1	38.4	39.7
2000	14.7	20.4	26.7	32.0	35.2	36.8	37.2
2100	15.4	20.8	26.4	30.6	32.7	33.6	33.9
2200	13.2	18.5	23.9	27.5	29.4	30.2	30.6
2300	9.8	15.4	20.7	24.2	26.1	27.1	27.3
2400	7.9	13.3	18.4	21.4	23.0	24.2	25.1
2500	8.5	13.7	17.4	19.5	20.6	21.6	22.6
2600	11.0	14.6	16.7	18.0	18.8	19.5	20.3
2700	11.9	14.6	16.0	16.8	17.3	17.7	18.4
2800	12.3	14.1	15.0	15.5	16.0	16.2	16.7
2900	11.9	13.1	13.8	14.3	14.6	14.9	15.2
3000	9.5	11.0	11.7	12.0	12.4	12.5	12.6
3100	7.5	9.2	10.1	10.7	11.2	11.6	11.9
3200	5.6	7.1	8.0	8.8	9.4	9.9	10.3
3300	4.0	5.3	6.2	7.0	7.7	8.3	8.8
3400	3.4	4.3	5.1	5.8	6.5	7.1	7.6
3500	3.2	3.9	4.5	5.1	5.6	6.2	6.8
3600	3.0	3.6	4.1	4.6	5.1	5.6	6.1
3700	3.0	3.5	3.9	4.3	4.7	5.2	5.7
4000	3.1	3.4	3.7	4.0	4.4	4.8	5.3
4100	3.3	3.6	3.9	4.2	4.6	5.0	5.5
4500	3.4	3.7	4.0	4.3	4.8	5.3	6.1

Table E.8.: Expected limits on the number of events for a confidence level 95% for the combined electron and moun channels. The limits are given as a function of the resonance mass M_X and the relative decay width Γ/M_X.

M_X [GeV]	Γ/M_X						
	0.0	0.05	0.1	0.15	0.2	0.25	0.3
800	118.1	173.5	202.6	208.7	199.5	182.9	164.3
900	50.5	71.9	86.5	96.4	101.3	102.1	101.3
1000	36.3	48.4	58.1	65.5	71.2	74.5	76.0
1100	29.7	39.0	46.8	53.4	59.0	62.7	65.0
1200	25.8	33.7	40.9	47.6	53.6	57.6	60.5
1300	22.2	29.3	36.4	43.4	49.6	54.1	57.2
1400	20.5	27.8	35.5	43.2	49.9	54.7	57.1
1500	19.3	26.4	34.8	43.4	50.6	54.9	56.8
1600	19.2	26.8	35.8	44.8	51.1	54.2	54.6
1700	17.6	25.2	34.3	43.1	48.5	50.6	50.6
1800	18.7	28.7	39.0	46.0	48.4	47.9	46.0
1900	14.3	21.6	29.7	36.0	38.7	39.8	39.8
2000	13.7	20.7	27.7	32.1	34.0	34.6	34.5
2100	12.6	18.9	24.6	28.0	29.4	29.9	29.9
2200	11.6	17.3	21.8	24.3	25.5	25.9	26.2
2300	10.7	15.7	19.2	21.3	22.4	22.8	22.9
2400	9.8	14.2	17.0	18.5	19.4	20.2	20.9
2500	9.0	12.7	15.0	16.2	17.1	17.7	18.4
2600	8.2	11.4	13.3	14.3	15.0	15.6	16.2
2700	7.6	10.2	11.8	12.7	13.3	13.8	14.4
2800	7.0	9.3	10.6	11.4	12.0	12.3	12.9
2900	6.6	8.6	9.6	10.3	10.9	11.3	11.7
3000	6.5	7.8	8.5	9.0	9.4	9.7	10.0
3100	5.5	7.0	7.8	8.4	8.9	9.3	9.7
3200	5.1	6.4	7.1	7.7	8.2	8.6	8.9
3300	4.7	6.0	6.6	7.1	7.6	8.0	8.4
3400	4.5	5.6	6.2	6.7	7.1	7.5	7.9
3500	4.3	5.3	5.8	6.3	6.8	7.2	7.6
3600	4.1	5.0	5.5	6.0	6.5	6.8	7.2
3700	4.0	4.8	5.3	5.8	6.2	6.6	7.0
4000	3.9	4.6	5.0	5.4	5.9	6.3	6.8
4100	4.1	4.7	5.2	5.7	6.2	6.7	7.3
4500	3.9	4.6	5.1	5.7	6.4	7.1	8.1

Bibliography

[1] L. Randall and R. Sundrum, "Large Mass Hierarchy from a Small Extra Dimension," *Phys. Rev. Lett.* **83** (Oct, 1999) 3370–3373. http://link.aps.org/doi/10.1103/PhysRevLett.83.3370.

[2] ATLAS Collaboration, "Search for resonances in diphoton events at $\sqrt{s}$=13 TeV with the ATLAS detector," *JHEP* **09** (2016) 001, arXiv:1606.03833 [hep-ex].

[3] CMS Collaboration, "Search for high-mass diphoton resonances in proton-proton collisions at 13 TeV and combination with 8 TeV search," arXiv:1609.02507 [hep-ex]. CMS-EXO-16-02, CERN-EP-2016-216.

[4] L. H. Ryder, *Quantum Field Theory*. Cambridge University Press, Trumpington Street, Cambridge, 1996.

[5] M. E. Peskin and D. V. Schroeder, *Quantum Field Theory*. Westview Press, 1995.

[6] J. C. Romao and J. P. Silva, "A resource for signs and Feynman diagrams of the Standard Model," *Int. J. Mod. Phys.* **A27** (2012) 1230025, arXiv:1209.6213 [hep-ph].

[7] B. C. Hall, *Lie Groups, Lie Algebras and Representations: An Elementary Introduction*. Springer, 2003. Graduate Texts in Mathematics.

[8] E. Noether, "Invariante Variationsprobleme," *Nachr. v. d. Ges. d. Wiss. zu Göttingen* (1918) 235–257.

[9] N. Byers, "E. Noether's discovery of the deep connection between symmetries and conservation laws," in *Symposium on the Heritage of Emmy Noether Ramat-Gan, Israel, December 2-4, 1996*. 1998. arXiv:physics/9807044 [physics].

[10] P. W. Higgs, "Broken Symmetries and the Masses of Gauge Bosons," *Phys. Rev. Lett.* **13** (Oct, 1964) 508–509.

[11] J. Goldstone *et al.*, "Broken symmetries," *Phys. Rev.* **127** (Aug, 1962) 965–970. http://link.aps.org/doi/10.1103/PhysRev.127.965.

[12] M. Kobayashi and T. Maskawa, "CP-Violation in the Renormalizable Theory of Weak Interaction," *Prog. of Theor. Phys.* **49** no. 2, (1973) 652–657, http://ptp.oxfordjournals.org/content/49/2/652.full.pdf+html.

[13] "Standard Model of Elementary Particles." https://commons.wikimedia.org/wiki/File:Standard_Model_of_Elementary_Particles.svg. licensed under: Creative Commons Attribution 3.0 Unported, Accessed: 2016-08-24.

[14] C. Giunti and M. Laveder, "Neutrino mixing," arXiv:hep-ph/0310238 [hep-ph].

[15] H. Georgi and S. L. Glashow, "Unity of All Elementary-Particle Forces," *Phys. Rev. Lett.* **32** (Feb, 1974) 438–441.

[16] ATLAS and CMS Collaboration, "Combined Measurement of the Higgs Boson Mass in pp Collisions at $\sqrt{s} = 7$ and 8 TeV with the ATLAS and CMS Experiments," *Phys. Rev. Lett.* **114** (2015) 191803, arXiv:1503.07589 [hep-ex].

[17] D. G. Banhatti, "Disk galaxy rotation curves and dark matter distribution," arXiv:astro-ph/0703430 [ASTRO-PH].

[18] K. Agashe *et al.*, "Warped Gravitons at the LHC and Beyond," *Phys. Rev.* **D76** (2007) 036006, arXiv:hep-ph/0701186 [hep-ph].

[19] A. Oliveira, "Gravity particles from Warped Extra Dimensions, a review. Part I - KK Graviton," arXiv:1404.0102 [hep-ph].

[20] C. Bär, *Elementare Differentialgeometrie*. 3. Auflage. Walter de Gruyter, 2010.

[21] O. Klein, "Quantentheorie und fünfdimensionale relativitätstheorie," *Zeitschrift für Physik* **37** no. 12, (1926) 895–906. http://dx.doi.org/10.1007/BF01397481.

[22] T. Kaluza, "Zum Unitätsproblem in der Physik," in *Sitzungsber. Preuss. Akad. Wiss. Berlin. (Math. Phys.)*, pp. 966–972. 1921. https://archive.org/details/sitzungsberichte1921preussi.

[23] H. Davoudiasl *et al.*, "Phenomenology of the Randall-Sundrum Gauge Hierarchy Model," *Phys. Rev. Lett.* **84** (2000) 2080, arXiv:hep-ph/9909255 [hep-ph].

[24] A. V. Kisselev, "Physical models within the framework of the Randall-Sundrum scenario," arXiv:1403.5469 [hep-th].

[25] K. Agashe *et al.*, "RS1, custodial isospin and precision tests," *JHEP* **08** (2003) 050, arXiv:hep-ph/0308036 [hep-ph].

[26] "Bulk-Graviton Model." http://www.physics.uci.edu/~tanedo/docs.html. Accessed: 2016-08-24.

[27] D. Pappadopulo *et al.*, "Heavy Vector Triplets: Bridging Theory and Data," *JHEP* **09** (2014) 060, arXiv:1402.4431 [hep-ph].

[28] R. Contino *et al.*, "Warped/composite phenomenology simplified," *JHEP* **05** (2007) 074, arXiv:hep-ph/0612180 [hep-ph].

[29] K. Agashe *et al.*, "Flavor structure of warped extra dimension models," *Phys. Rev.* **D71** (2005) 016002, arXiv:hep-ph/0408134 [hep-ph].

[30] H. de Sandes and R. Rosenfeld, "Radion-Higgs mixing effects on bounds from LHC Higgs Searches," *Phys. Rev.* **D85** (2012) 053003, arXiv:1111.2006 [hep-ph].

[31] M. Frank, K. Huitu, U. Maitra, and M. Patra, "Probing Higgs-radion mixing in warped models through complementary searches at the LHC and the ILC," arXiv:1606.07689 [hep-ph].

[32] V. Barger and M. Ishida, "Randall-Sundrum Reality at the LHC," *Phys. Lett.* **B709** (2012) 185–191, arXiv:1110.6452 [hep-ph].

[33] CMS Collaboration, "Common note on searches for new diboson resonances in semileptonic and hadronic final states at $\sqrt{s} = 13$ TeV." AN-15-196, 2015.

[34] C. Lefèvre, "The CERN accelerator complex. Complexe des accélérateurs du CERN," Dec, 2008. https://cds.cern.ch/record/1260465.

[35] L. Evans and P. Bryant, "LHC Machine," *JINST* **3** no. 08, (2008) S08001.

[36] S. Chatrchyan *et al.*, "The CMS experiment at the CERN LHC," *JINST* **3** (2008) S08004.

[37] G. Aad *et al.*, "The ATLAS Experiment at the CERN Large Hadron Collider," *JINST* **3** (2008) S08003.

[38] ALICE Collaboration, "The ALICE experiment at the CERN LHC," *JINST* **3** no. 08, (2008) S08002.

[39] LHCb Collaboration, "The LHCb Detector at the LHC," *JINST* **3** no. 08, (2008) S08005.

[40] CMS Collaboration, "CMS Detector Slice." `https://cms-docdb.cern.ch/cgi-bin/PublicDocDB/ShowDocument?docid=4172`. Accessed: 2016-08-29.

[41] "New CMS results at Moriond (Electroweak) 2013." `http://cms.web.cern.ch/news/new-cms-results-moriond-electroweak-2013`. Accessed: 2016-08-29.

[42] V. Karimäki *et al.*, *The CMS tracker system project: Technical Design Report*. Technical Design Report CMS. CERN, Geneva, 1997. `http://cds.cern.ch/record/368412`. CERN-LHCC-98-006.

[43] CMS Collaboration, "Operation and performance of the CMS tracker," *JINST* **9** (2014) C03005, `arXiv:1402.0675 [physics.ins-det]`.

[44] A. Dominguez *et al.*, "CMS Technical Design Report for the Pixel Detector Upgrade," Tech. Rep. CERN-LHCC-2012-016. CMS-TDR-11, Sep, 2012. `https://cds.cern.ch/record/1481838`.

[45] CMS Collaboration, "Energy calibration and resolution of the CMS electromagnetic calorimeter in pp collisions at $\sqrt{s} = 7$ TeV," *JINST* **8** no. 09, (2013) P09009.

[46] D. Green, *The Physics of Particle Detectors*. Cambridge University Press, Trumpington Street, Cambridge, 2000.

[47] CMS Collaboration, "Performance of the CMS hadron calorimeter with cosmic ray muons and LHC beam data," *JINST* **5** no. 03, (2010) .

[48] HEPHY, "CMS Detector Layout." `http://www.hephy.at/user/friedl/diss/html/node8.html`. Accessed: 2016-09-09.

[49] C. Eck *et al.*, *LHC computing Grid: Technical Design Report. Version 1.06 (20 Jun 2005)*. Technical Design Report LCG. CERN, Geneva, 2005. `https://cds.cern.ch/record/840543`.

[50] CERN, "The Grid: A system of tiers." `https://home.cern/about/computing/grid-system-tiers`. Accessed: 2016-09-09.

[51] J. M. Butterworth *et al.*, "Hard Processes in Proton-Proton Collisions at the Large Hadron Collider," *Ann. Rev. Nucl. Part. Sci.* **62** (2012) 387–405, arXiv:1202.0583 [hep-ex].

[52] J. M. Campbell *et al.*, "Hard Interactions of Quarks and Gluons: A Primer for LHC Physics," *Rept. Prog. Phys.* **70** (2007) 89, arXiv:hep-ph/0611148 [hep-ph].

[53] V. N. Gribov and L. N. Lipatov, "Deep inelastic e p scattering in perturbation theory," *Sov. J. Nucl. Phys.* **15** (1972) 438–450. [Yad. Fiz.15,781(1972)].

[54] G. Altarelli and G. Parisi, "Asymptotic Freedom in Parton Language," *Nucl. Phys.* **B126** (1977) 298–318.

[55] Y. L. Dokshitzer, "Calculation of the Structure Functions for Deep Inelastic Scattering and e+ e- Annihilation by Perturbation Theory in Quantum Chromodynamics.," *Sov. Phys. JETP* **46** (1977) 641–653. [Zh. Eksp. Teor. Fiz.73,1216(1977)].

[56] R. D. Ball *et al.*, "Unbiased global determination of parton distributions and their uncertainties at NNLO and at LO," *Nucl. Phys.* **B855** (2012) 153–221, arXiv:1107.2652 [hep-ph].

[57] J. Butterworth *et al.*, "PDF4LHC recommendations for LHC Run II," *J. Phys.* **G43** (2016) 023001, arXiv:1510.03865 [hep-ph].

[58] A. D. Martin *et al.*, "Parton distributions for the LHC," *Eur. Phys. J.* **C63** (2009) 189–285, arXiv:0901.0002 [hep-ph].

[59] CMS Collaboration, "Particle-Flow Event Reconstruction in CMS and Performance for Jets, Taus, and MET,". CMS-PAS-PFT-09-001.

[60] CMS Collaboration, "Commissioning of the Particle-Flow reconstruction in Minimum-Bias and Jet Events from pp Collisions at 7 TeV,". CMS-PAS-PFT-10-002.

[61] F. Beaudette, "The CMS Particle Flow Algorithm," in *Proceedings, International Conference on Calorimetry for the High Energy Frontier (CHEF 2013)*, pp. 295–304. 2013. arXiv:1401.8155 [hep-ex].

[62] S. Chatrchyan *et al.*, "Description and performance of track and primary-vertex reconstruction with the CMS tracker," *JINST* **9** no. 10, (2014) P10009, arXiv:1405.6569 [physics.ins-det].

[63] P. Billoir and S. Qian, "Simultaneous pattern recognition and track fitting by the Kalman filtering method," *Nucl. Instrum. Methods Phys. Res. A.* **294** no. 1, (1990) 219 – 228. http://www.sciencedirect.com/science/article/pii/016890029091835Y.

[64] P. Billoir, "Progressive track recognition with a Kalman like fitting procedure," *Comput. Phys. Commun.* **57** (1989) 390–394.

[65] R. Frühwirth, "Application of Kalman filtering to track and vertex fitting," *Nucl. Instrum. Methods Phys. Res., A* **262** no. HEPHY-PUB-503, (Jun, 1987) 444. 19 p. https://cds.cern.ch/record/178627.

[66] W. Waltenberger, "Adaptive Vertex Reconstruction," Tech. Rep. CMS-NOTE-2008-033, CERN, Geneva, Jul, 2008. http://cds.cern.ch/record/1166320.

[67] CMS Collaboration, "Particle-Flow Event Reconstruction in CMS and Performance for Jets, Taus, and MET," Tech. Rep. CMS-PAS-PFT-09-001, CERN, Apr, 2009. https://cds.cern.ch/record/1194487.

[68] W. Adam *et al.*, "Reconstruction of electrons with the Gaussian-sum filter in the CMS tracker at LHC," arXiv:0306087 [hep-ph].

[69] V. Khachatryan *et al.*, "Performance of Electron Reconstruction and Selection with the CMS Detector in Proton-Proton Collisions at $\sqrt{s} = 8$ TeV," *JINST* **10** no. 06, (2015) P06005, arXiv:1502.02701 [physics.ins-det].

[70] CMS Collaboration, "Reconstruction of electrons with the Gaussian-sum filter in the CMS tracker at the LHC," *Journal of Physics G Nuclear Physics* **31** (Sep, 2005) N9–N20, physics/0306087.

[71] G. F. Sterman, "QCD and Jets," in *Physics in D >= 4. Proceedings, Theoretical Advanced Study Institute in elementary particle physics, TASI 2004, Boulder, USA, June 6-July 2, 2004*, pp. 67–145. 2004. arXiv:hep-ph/0412013 [hep-ph].

[72] S. D. Ellis *et al.*, "Jets in Hadron-Hadron Collisions," *Prog. Part. Nucl. Phys.* **60** (2008) 484–551, arXiv:0712.2447 [hep-ph].

[73] G. P. Salam and G. Soyez, "A Practical Seedless Infrared-Safe Cone jet algorithm," *JHEP* **05** (2007) 086, arXiv:0704.0292 [hep-ph].

[74] Y. L. Dokshitzer *et al.*, "Better jet clustering algorithms," *JHEP* **08** (1997) 001, arXiv:hep-ph/9707323 [hep-ph].

[75] M. Wobisch and T. Wengler, "Hadronization corrections to jet cross-sections in deep inelastic scattering," in *Monte Carlo generators for HERA physics. Proceedings, Workshop, Hamburg, Germany, 1998-1999*, pp. 270–279. 1998. arXiv:hep-ph/9907280 [hep-ph].

[76] CMS Collaboration, "Performance of Jet Algorithms in CMS,". http://cds.cern.ch/record/1198227. CMS-PAS-JME-07-003.

[77] M. Cacciari *et al.*, "The Anti-k(t) jet clustering algorithm," *JHEP* **04** (2008) 063, arXiv:0802.1189 [hep-ph].

[78] **CMS** Collaboration, V. Khachatryan *et al.*, "Jet energy scale and resolution in the CMS experiment in pp collisions at 8 TeV," *Submitted to: JINST* (2016) , arXiv:1607.03663 [hep-ex]. CMS-JME-13-004, CERN-PH-EP-2015-305.

[79] M. Cacciari *et al.*, "Pileup subtraction using jet areas," *Phys. Lett.* **B659** (2008) 119–126, arXiv:0707.1378 [hep-ph].

[80] S. D. Ellis *et al.*, "Recombination Algorithms and Jet Substructure: Pruning as a Tool for Heavy Particle Searches," *Phys. Rev.* **D81** (2010) 094023, arXiv:0912.0033 [hep-ph].

[81] S. Chatrchyan *et al.*, "Identification of b-quark jets with the CMS experiment," *JINST* **8** (2013) P04013, arXiv:1211.4462 [hep-ex].

[82] N. Bartosik, "b-jet tagging." http://bartosik.pp.ua/hep_sketches/btagging. Accessed: 2016-09-13.

[83] J. Thaler *et al.*, "Identifying Boosted Objects with N-subjettiness," *JHEP* **03** (2011) 015, arXiv:1011.2268 [hep-ph].

[84] V. Khachatryan *et al.*, "Search for massive resonances decaying into pairs of boosted bosons in semi-leptonic final states at $\sqrt{s} = 8$ TeV," *JHEP* **08** (2014) 174, arXiv:1405.3447 [hep-ex].

[85] V. Khachatryan *et al.*, "Identification techniques for highly boosted W bosons that decay into hadrons," *JHEP* **12** (2014) 017, arXiv:1410.4227 [hep-ex].

[86] V. Khachatryan *et al.*, "Performance of the CMS missing transverse momentum reconstruction in pp data at $\sqrt{s} = 8$ TeV," *JINST* **10** no. 02, (2015) P02006, arXiv:1411.0511 [physics.ins-det].

[87] A. Buckley *et al.*, "General-purpose event generators for LHC physics," *Phys. Rept.* **504** (2011) 145–233, arXiv:1101.2599 [hep-ph].

[88] M. H. Seymour and M. Marx, "Monte Carlo Event Generators," in *Proceedings, 69th Scottish Universities Summer School in Physics : LHC Phenomenology (SUSSP69): St.Andrews, Scotland, August 19-September 1, 2012*, pp. 287–319. 2013. arXiv:1304.6677 [hep-ph].

[89] M. A. Dobbs *et al.*, "Les Houches guidebook to Monte Carlo generators for hadron collider physics," in *Physics at TeV colliders. Proceedings, Workshop, Les Houches, France, May 26-June 3, 2003*, pp. 411–459. 2004. arXiv:hep-ph/0403045 [hep-ph].

[90] N. Bartosik, "Event simulation in HEP experiments." http://bartosik.pp.ua/hep_sketches/event_simulation. Accessed: 2016-09-13.

[91] S. Hoeche *et al.*, "Matching parton showers and matrix elements," in *HERA and the LHC: A Workshop on the implications of HERA for LHC physics: Proceedings Part A*. 2006. arXiv:hep-ph/0602031 [hep-ph]. https://inspirehep.net/record/709818/files/arXiv:hep-ph_0602031.pdf.

[92] T. Sjöstrand, "The lund monte carlo for jet fragmentation and e+e- physics - jetset version 6.2," *Comput. Phys. Commun.* **39** no. 3, (1986) 347 – 407. http://www.sciencedirect.com/science/article/pii/0010465586900962.

[93] T. Sjöstrand and M. Bengtsson, "The lund monte carlo for jet fragmentation and e+ e- physics - jetset version 6.3 - an update," *Comput. Phys. Commun.* **43** no. 3, (1987) 367 – 379. http://www.sciencedirect.com/science/article/pii/0010465587900543.

[94] H.-U. Bengtsson, "The lund monte carlo for high-pt physics," *Comput. Phys. Commun.* **31** no. 4, (1984) 323 – 355. http://www.sciencedirect.com/science/article/pii/0010465584900183.

[95] A. Kupco, "Cluster hadronization in HERWIG 5.9," in *Monte Carlo generators for HERA physics. Proceedings, Workshop, Hamburg, Germany, 1998-1999*, pp. 292–300. 1998. arXiv:hep-ph/9906412 [hep-ph].

[96] D. Amati and G. Veneziano, "Preconfinement as a property of perturbative qcd," *Phys. Lett. B* **83** no. 1, (1979) 87 – 92. http://www.sciencedirect.com/science/article/pii/0370269379908967.

[97] G. Gustafson *et al.*, "Jet final states in ww pair production and colour screening in the qcd vacuum," *Phys. Lett. B* **209** no. 1, (1988) 90 – 94.

[98] S. Agostinelli *et al.*, "Geant4—a simulation toolkit," *Nuclear Instruments and Methods in Physics Research Section A: Accelerators, Spectrometers, Detectors and Associated Equipment* **506** no. 3, (2003) 250 – 303.

[99] V. Lefébure *et al.*, "CMS Simulation Software Using Geant4,". CMS-NOTE-1999-072.

[100] J. Alwall *et al.*, "MadGraph 5 : Going Beyond," *JHEP* **06** (2011) 128, arXiv:1106.0522 [hep-ph].

[101] K. Hagiwara *et al.*, "HELAS and MadGraph/MadEvent with spin-2 particles," *Eur. Phys. J.* **C56** (2008) 435–447, arXiv:0805.2554 [hep-ph].

[102] P. de Aquino *et al.*, "Simulating graviton production at hadron colliders," *JHEP* **06** (2011) 132, arXiv:1101.5499 [hep-ph].

[103] K. Hagiwara *et al.*, "TauDecay: a library to simulate polarized tau decays via FeynRules and MadGraph5," *Eur. Phys. J.* **C73** (2013) 2489, arXiv:1212.6247 [hep-ph].

[104] C. Oleari, "The POWHEG-BOX," *Nucl. Phys. Proc. Suppl.* **205-206** (2010) 36–41, arXiv:1007.3893 [hep-ph].

[105] T. Sjöstrand *et al.*, "High-energy physics event generation with PYTHIA 6.1," *Comput. Phys. Commun.* **135** (2001) 238–259, arXiv:hep-ph/0010017 [hep-ph].

[106] S. Jadach *et al.*, "TAUOLA: A Library of Monte Carlo programs to simulate decays of polarized tau leptons," *Comput. Phys. Commun.* **64** (1990) 275–299. CERN-TH-5856-90.

[107] A. L. Read, "Presentation of search results: the CLs technique," *Journal of Physics G: Nuclear and Particle Physics* **28** no. 10, (2002) 2693.

[108] G. Bohm and G. Zech, *Einfürung in Statistik und Messwertanalyse für Physiker.* Verlag Deutsches Elektronen-Synchotron in der Helmholzgemeinschaft, D-22603 Hamburg, 2006.

[109] G. Cowan, "Statistics for Searches at the LHC," in *Proceedings, 69th Scottish Universities Summer School in Physics : LHC Phenomenology (SUSSP69):*

St.Andrews, Scotland, August 19-September 1, 2012, pp. 321–355. 2013. arXiv:1307.2487 [hep-ex].

[110] G. Cowan *et al.*, "Asymptotic formulae for likelihood-based tests of new physics," *Eur. Phys. J.* **C71** (2011) 1554, arXiv:1007.1727 [physics.data-an]. [Erratum: Eur. Phys. J.C73,2501(2013)].

[111] A. Wald, "Tests of Statistical Hypotheses Concerning Several Parameters When the Number of Observations is Large," *AMS* **54** (1943) 426–482.

[112] T. Junk, "Confidence level computation for combining searches with small statistics," *Nucl. Instrum. Methods. Section A: Accelerators, Spectrometers, Detectors and Associated Equipment* **434** no. 2, (1999) 435 – 443.

[113] CMS Collaboration, "Search for new WV diboson resonances in the semileptonic final state." AN-15-197, 2015.

[114] CMS Collaboration, "Search for heavy resonances in the W/Z dijet mass spectrum at CMS." AN-15-211, 2015.

[115] P. Skands *et al.*, "Tuning PYTHIA 8.1: the Monash 2013 Tune," *Eur. Phys. J.* **C74** no. 8, (2014) 3024, arXiv:1404.5630 [hep-ph].

[116] CMS Collaboration, "Performance of CMS muon reconstruction in *pp* collision events at $\sqrt{s} = 7$ TeV," *JINST* **7** (2012) P10002, arXiv:1206.4071 [physics.ins-det]. CMS-MUO-10-004, CERN-PH-EP-2012-173.

[117] CMS Collaboration, "Pileup Jet Identification," Tech. Rep. CMS-PAS-JME-13-005, CERN, Geneva, 2013. https://cds.cern.ch/record/1581583.

[118] K. A. Olive *et al.*, "Review of Particle Physics," *Chin. Phys.* **C38** (2014) 090001.

[119] CMS Collaboration, "Identifying Hadronically Decaying Vector Bosons Merged into a Single Jet," Tech. Rep., CERN, Geneva, 2013. https://cds.cern.ch/record/1577417. CMS-PAS-JME-13-006.

[120] J. Alwall *et al.*, "A Standard format for Les Houches event files," *Comput. Phys. Commun.* **176** (2007) 300–304, arXiv:hep-ph/0609017 [hep-ph].

[121] A. Oliveira, "Gravity particles from Warped Extra Dimensions, predictions for LHC," arXiv:1404.0102v2 [hep-ph]. Revised in Sep. 2016.

Danksagung

Zunächst möchte ich mich bei Herrn Prof. Dr. Th. Müller für die Möglichkeit bedanken meine Masterarbeit in seiner Arbeitsgruppe anzufertigen und für die vielen und spannenden Konferenzen, die ich im laufe meiner Zeit am Institut besuchen durfte.

Als zweites möchte ich Herrn Prof. Dr. Husemann für die Übernahme des Korreferats danken.

Besonderen Dank verdient mein Betreuer Matthias Mozer für die unermüdliche Betreuung, und seine wissenschaftliche, moralische und organisatorische Unterstützung.

Für das Korrekturlesen meiner Arbeit möchte ich Frank Roscher und Matthias Mozer besonders danken.

Ich möchte mich außerdem bei allen Mitgliedern des EKP bedanken, für die stets angenehme Arbeitsatmosphäre und insbesondere bei Frau Bräunling und dem Admin-Team, die für einen stets reibungslosen Ablauf im organisatorischen und technischen Bereich sorgten. Hier möchte ich mich besonders bei Matthias Schnepf bedanken, der für Probleme mit der Desktop-Cloud, mit der große Teile dieser Arbeit berechnet wurden, immer mit einer schnellen und zuverlässigen Lösung aufwarten konnte.

Mein größter Dank gilt meiner Familie, ohne deren stete Untersützung mein Studium nicht möglich gewesen wäre.